

The Production Cross Sections of the Weak  
Vector Bosons in  $p\bar{p}$  Collisions at  $\sqrt{s}=1.96$  TeV and  
a Measurement of the  $W$  Boson Decay Width

by

Alexei Valerievich Varganov

A dissertation submitted in partial fulfilment  
of the requirements for the degree of  
Doctor of Philosophy  
(Physics)  
in the University of Michigan  
2004

Doctoral Committee:

Professor Dante E. Amidei, Chair  
Professor Philip H. Bucksbaum  
Professor Sherril A. Smith  
Associate Professor Jianming Qian  
Assistant Professor James D. Wells

Copyright © Alexei Varganov 2004  
All Rights Reserved

## ACKNOWLEDGMENTS

The work presented in this thesis would not have been possible without the valuable guidance and support from my adviser *Dan Amidei* and help from other members of the Michigan CDF group: *Stephen Miller, Ken Bloom, Monica Tecchio, Myron Campbell, Dave Gerdes, Nate Goldschmidt, Tom Schwarzt, Kathy Copic, Jian Kang*. They are also the people who contributed greatly to the CDF upgrade and made Run II data taking happen.

A special thank you is due to the committee members *Prof. James, Prof. Qian, Prof. Bucksbaum, and Prof. Smith* for their useful comments and fruitful discussions.

I also would like to acknowledge as well the constant support from my wife *Olga* and my parents *Lubov* and *Valerij Varganov*. I also appreciated very much the motivation from my brother *Georgij* and daughter *Nina*.

# CONTENTS

ACKNOWLEDGMENTS . . . . .	ii
LIST OF FIGURES . . . . .	v
LIST OF TABLES . . . . .	viii
LIST OF APPENDICES . . . . .	ix
CHAPTER 1 <b>Introduction</b> . . . . .	1
1.1 The Standard Model . . . . .	1
1.2 Cross Sections in Colliding Beam Experiments . . . . .	5
1.3 $W$ and $Z$ Processes in Hadron Collisions . . . . .	6
1.4 Measurement of $W$ Width from the Cross Section Ratio . . . . .	15
1.5 Strategy of This Measurement . . . . .	15
CHAPTER 2 <b>The Tevatron and The Collider Detector</b> . . . . .	17
2.1 Tevatron at Fermilab . . . . .	17
2.2 Overview of CDF . . . . .	19
2.3 Tracking System . . . . .	21
2.4 Calorimeter . . . . .	26
2.5 Muon Chambers . . . . .	29
2.6 Data Acquisition System . . . . .	32
CHAPTER 3 <b>Data Sets</b> . . . . .	36
3.1 Inclusive Muon Samples . . . . .	36
3.2 High- $P_T$ Muon Trigger Paths . . . . .	37
3.3 Simulation Samples . . . . .	38

CHAPTER 4	<b>Muon Identification</b>	39
4.1	Inclusive Muon Selections	41
4.2	Cosmic Ray Contamination	43
CHAPTER 5	<b>W Selection Criteria</b>	45
CHAPTER 6	<b>W Backgrounds</b>	52
6.1	Electroweak Processes	52
6.2	QCD Backgrounds	53
6.3	Cosmic Background	59
CHAPTER 7	<b>Z Selection Criteria</b>	62
CHAPTER 8	<b>Z Backgrounds</b>	66
8.1	Cosmic Background	66
8.2	Electroweak Processes	67
8.3	QCD Backgrounds	68
CHAPTER 9	<b>Acceptances</b>	69
CHAPTER 10	<b>Efficiencies</b>	72
10.1	Efficiency for Selecting $W$	74
10.2	Efficiency for Selecting $Z$	75
10.3	Ratio of Efficiencies	78
CHAPTER 11	<b>Result</b>	79
11.1	$W$ Cross Section	80
11.2	$Z$ Cross Section	80
11.3	$W/Z$ Cross Section Ratio	82
11.4	Extracting Physics Quantities	84
11.5	Limit on Unknown Modes of $W$ Decay	87
APPENDICES		89
BIBLIOGRAPHY		96

# LIST OF FIGURES

## Figure

1.1	Feynman diagrams for the dominant $W$ hadronic production processes with muonic decay. . . . .	7
1.2	Feynman diagrams for the dominant $Z$ hadronic production processes with muonic decay. . . . .	7
1.3	Hadron-hadron collision via a hard parton subprocess. . . . .	9
1.4	The CTEQ6M quark and gluon distribution functions for proton at the energy scale of $Q^2 = 2$ GeV. . . . .	11
1.5	The CTEQ6M quark and gluon distribution functions for proton at the energy scale of $Q^2 = 100$ GeV. . . . .	11
2.1	Schematic view of Tevatron . . . . .	18
2.2	Elevation view of one half of the CDF II detector . . . . .	20
2.3	Tracking system of the CDF II detector . . . . .	22
2.4	Transverse view of Layer 00. . . . .	23
2.5	Transverse view of SVX II barrel. . . . .	23
2.6	Cell layout for super-layer 2. . . . .	24
2.7	1/6th view of COT east end-plate. . . . .	24
2.8	1/8th of calorimeter segmentation map. . . . .	26
2.9	Central electromagnetic calorimeter wedge. . . . .	27
2.10	Cross section of upper part of end plug calorimeter. . . . .	28
2.11	$\eta$ and $\phi$ coverage of the CDF II muon system. . . . .	30

2.12	Transverse view of a CMU module. . . . .	31
2.13	Transverse view of a CMP stack. . . . .	31
2.14	Schematic view of DAQ and trigger systems. . . . .	33
4.1	Schematic view of the detector systems involved in muon reconstruction. . . . .	40
4.2	Illustration of muon isolation variable definition. . . . .	40
5.1	Muon transverse momentum spectrum in data and simulation for $W \rightarrow \mu\nu$ candidate events. Only the leading contributing processes are shown. . . . .	46
5.2	A schematic view illustrating the calculation of $\cancel{E}_T$ variable. . . . .	48
5.3	The transverse mass spectrum in data and simulation for $W \rightarrow \mu\nu$ events. . . . .	50
5.4	Number of $W$ candidate events per a run range. . . . .	51
5.5	$W$ candidate yield per inverse picobarn of delivered luminosity. . . . .	51
6.1	Isolation vs. $\cancel{E}_T$ distribution for $W$ candidate events. . . . .	54
6.2	Isolation vs. $\cancel{E}_T$ distribution for $W \rightarrow \mu\nu$ simulation. . . . .	54
6.3	The background dependence on $\cancel{E}_T$ cut for $W$ candidates. . . . .	56
6.4	The background dependence on isolation ratio cut for $W$ candidates. . . . .	56
6.5	$\cancel{E}_T$ in data and Monte Carlo for $W \rightarrow \mu\nu$ candidate events. . . . .	58
6.6	The difference between $\hat{z}$ components of CMU hits and projected cosmic ray hit for cosmics data. . . . .	60
6.7	The difference between $\hat{z}$ components of CMU hits and projected cosmic ray hit for $W$ data. . . . .	60
7.1	Dimuon invariant mass $M_{\mu\mu}$ distribution in data and simulation for $Z \rightarrow \mu^+\mu^-$ candidate events. . . . .	63
7.2	Number of $Z$ candidate events per a run range. . . . .	65

7.3	$Z$ candidate yield per inverse picobarn of delivered luminosity. . . . .	65
8.1	The distribution of 3- $D$ opening angle between muon legs in cosmic ray events. . . . .	67
8.2	The distribution of 3- $D$ opening angle between muon legs in collision data, compared to $Z \rightarrow \mu\mu$ Monte Carlo. . . . .	67
11.1	The measurements of $W$ production cross section in leptonic channel. .	81
11.2	The measurements of $Z$ production cross section in leptonic channel. . .	83
11.3	Comparison of our result for $BR(W \rightarrow \ell\nu)$ with those from the other measurements and the Standard Model expectation. . . . .	86
11.4	Comparison of our result for $\Gamma(W)$ with those from the other measurements and the Standard Model prediction. . . . .	88



# LIST OF TABLES

## Table

1.1	Quarks and Leptons representation in the Standard Model. . . . .	3
4.1	Inclusive high- $P_T$ muon selection cuts. . . . .	43
5.1	$W \rightarrow \mu\nu$ selection cuts. . . . .	49
6.1	Event distribution for regions A, B, C, and D for various processes. . . .	53
6.2	The calculated number of the background events in the signal region D for varying $\cancel{E}_T$ cut. . . . .	56
6.3	The calculated number of the background events in the signal region D for varying isolation ratio cut. . . . .	57
7.1	Loose muon cuts for $Z \rightarrow \mu^+\mu^-$ selection. . . . .	64
9.1	$W$ acceptance calculation. . . . .	69
9.2	$Z$ acceptance calculation. . . . .	69
9.3	Summary of uncertainties for calculating the acceptance ratio . . . . .	70
10.1	Muon identification efficiencies . . . . .	73
11.1	Measured input parameters for the cross section and ratio calculations.	79

# LIST OF APPENDICIES

## Appendix

A Interference Correction in $Z$ Cross Section . . . . .	90
B The CDF Collaboration . . . . .	91

# CHAPTER 1

## Introduction

The theory that describes the fundamental particle interactions is called the Standard Model, which is a gauge field theory that comprises the Glashow-Weinberg-Salam model [1, 2, 3] of the weak and electromagnetic interactions and quantum chromodynamics (QCD) [4, 5, 6], the theory of the strong interactions. The discovery of the  $W$  [7, 8] and  $Z$  [9, 10] bosons in 1983 by the UA1 and UA2 collaborations at the CERN  $p\bar{p}$  collider provided a direct confirmation of the unification of the weak and electromagnetic interactions. Since then, many experiments have refined our understanding of the characteristics of the  $W$  and  $Z$  bosons.

### 1.1 The Standard Model

The Standard Model is a physics theory which describes the *strong*, *weak*, and *electromagnetic* fundamental forces interacting between structureless or *fundamental* particles. It uses the theoretical framework of quantum field theory, and is therefore consistent with both quantum mechanics and special relativity. To date, almost all experimental tests of the three forces described by the Standard Model have agreed with its predictions.

Fundamental particles are divided into *bosons* and *fermions*. The intrinsic angular momentum of a particle is known as its *spin*. Fermions possess half-integer spin and bosons possess integer spin.

The Standard Model combines the theory of *quantum chromodynamics* (which de-

scribes the strong interactions) with the theory of the *electroweak interaction* (which describes the weak and electromagnetic interactions.) Each of these theories are *gauge field theories*, meaning that they describe fermions coupled to bosons, with the bosons mediating the forces between fermions. Quantum field theory formalism uses the *Lagrangian* operator to completely describe the system of particles and their interactions. The Lagrangian of each set of bosons is invariant under a transformation called a *gauge transformation*, and each gauge transformation can be described by a *unitary group* called a “gauge group”. Thus, these mediating bosons are often referred to as “gauge bosons”. The gauge group of the strong interaction is  $SU(3)$ , and the gauge group of the electroweak interaction is  $SU(2) \times U(1)$ . Therefore, the Standard Model is often referred to as  $SU(3) \times SU(2) \times U(1)$ .

The fermions of the Standard Model are divided into two categories: *quarks* and *leptons*. Quarks are fermions that participate in quantum chromodynamics processes, whereas leptons are not affected by the strong interaction. Within the Standard Model the quarks and leptons are arranged in three “generations” in the order of increasing particle masses. Leptons are combined together into pairs of electrically charged and neutral fermions. Three generation of leptons that carry electric charge  $-e$  are: first—*electron*, second—*muon*, and third—*tau*. There is one neutral fermion—*neutrino* associated with ever one of these leptons for each generation. Each generation of quarks consist of a pair of *up*- and *down*-flavored quarks with electric charges  $+\frac{2}{3}e$  and  $-\frac{1}{3}e$  respectively. The three generations of up-flavored quarks are: first—*up*, second—*charm*, and third—*top*. Similarly, the three generations of down-flavored quarks are: first—*down*, second—*strange*, and third—*bottom*.

Since quarks participate in strong interaction they cannot be observed individually. For this reason, quarks are *confined* in groups with other quarks to form *hadrons*—composite particles. Hadrons are divided into *baryons* (three quark objects), and *mesons* (quark-antiquark objects). Ordinary matter is made of baryons

such as protons (each a  $u-u-d$  quark set) and neutrons (each a  $u-d-d$  quark set).

The component of the spin in the direction of motion of a particle is called *helicity*. For massless particles, or particles moving near the speed of light, the helicity is a good approximation of a field quantity called *chirality*. Electroweak interaction affects differently fermions with positive or *right-handed* and negative or *left-handed* chirality. Quarks and leptons in the left-handed state are paired into weak  $SU(2)$  doublets and fermions in the right-handed state are singlets.

Fermion Type	Generation		
	First	Second	Third
Quarks	$\begin{pmatrix} u \\ d \end{pmatrix}_L, u_R, d_R$	$\begin{pmatrix} c \\ s \end{pmatrix}_L, c_R, s_R$	$\begin{pmatrix} t \\ b \end{pmatrix}_L, t_R, b_R$
Leptons	$\begin{pmatrix} \nu_e \\ e \end{pmatrix}_L, e_R, (\nu_e)_R$	$\begin{pmatrix} \nu_\mu \\ \mu \end{pmatrix}_L, \mu_R, (\nu_\mu)_R$	$\begin{pmatrix} \nu_\tau \\ \tau \end{pmatrix}_L, \tau_R, (\nu_\tau)_R$

**Table 1.1.** Quarks and Leptons representation in the Standard Model. The subscripts  $L$  and  $R$  indicate the left- and right-handed helicity state of a given fermion. The left-handed states are weak  $SU(2)$  doublets and the right-handed states are singlets.

The gauge bosons in the Standard Model are:

- photon  $\gamma$ , which mediate the electromagnetic interaction between particles;
- $W^+$ ,  $W^-$ ,  $Z^0$  bosons, which mediate the weak force between fermions;
- eight gluons  $g$ , which mediate the strong force between quarks.

Photon and gluons are massless bosons and they do not carry electric charge. The weak  $W$  and  $Z$  bosons acquire their masses of  $M_W=80.4 \text{ GeV}/c^2$  and  $M_Z=91.2 \text{ GeV}/c^2$  through the mechanism of *spontaneous symmetry breaking* of the gauge groups induced by the *Higgs* field [11].

All the interactions between quarks and leptons are described by the Standard Model Lagrangian terms, in which fermionic fields are coupled with the gauge bosons. Equation 1.1 shows the relevant parts of  $SU(3) \times SU(2) \times U(1)$  Lagrangian for the

first generation of fermions [12]:

$$\begin{aligned}
\mathcal{L} = & e \sum_{f=\nu,e,u,d} Q_f (\bar{f} \gamma^\mu f) A_\mu \\
& + \frac{g_2}{\cos \theta_w} \sum_{f=\nu,e,u,d} \left\{ (\bar{f}_L \gamma^\mu f_L) [T_f^3 - Q_f \sin^2 \theta_w] + (\bar{f}_R \gamma^\mu f_R) [-Q_f \sin^2 \theta_w] \right\} Z_\mu \\
& + \frac{g_2}{\sqrt{2}} \left[ \left\{ (\bar{u}_L \gamma^\mu d'_L) + (\bar{\nu}_L \gamma^\mu e_L) \right\} W_\mu^+ + \left\{ (\bar{d}'_L \gamma^\mu u_L) + (\bar{e}_L \gamma^\mu \nu_L) \right\} W_\mu^- \right] \\
& + \frac{g_3}{2} \sum_{q=u,d} (\bar{q}_\alpha \gamma^\mu \lambda_{\alpha\beta}^a q_\beta) G_\mu^a, \tag{1.1}
\end{aligned}$$

where the first line represents electromagnetic term, second and third lines express the weak interaction due to neutral and charged current respectively, and the last line describes strong interactions. The factors in front of each line are coupling constants, that characterize the strength of each interaction. The relation between  $e$  and  $g_2$  is  $e = g_2 \sin \theta_w$ , where  $\theta_w$  is the *weak angle*—a parameter, which relates the strengths of electromagnetic and weak interactions for both charged and neutral currents. By setting  $\hbar=c=1$  we can express the values of the coupling constants in *natural units*:

$$\alpha = \frac{e^2}{4\pi} \simeq \frac{1}{137}, \quad \alpha_w = \frac{g_2^2}{4\pi} = \frac{\sqrt{2} G_F M_W^2}{\pi} \simeq \frac{1}{30}, \quad \alpha_s = \frac{g_3^2}{4\pi} \simeq (0.3 \rightarrow 0.1), \tag{1.2}$$

where *elementary charge*  $e$ , *Fermi constant*  $G_F$ , and *W boson mass*  $M_W$  are additional parameters of the Standard Model. The strong coupling decreases when interaction energy increases—a perturbative QCD phenomenon known as *asymptotic freedom*.

The observable mass of a quark corresponds to the eigenstate which differs from its weak state, thus down-flavor quark  $d'$  in the term for the charged weak current is a combination of  $d$ ,  $s$ , and  $b$  quarks. This phenomenon is known as *Cabibbo-Kobayashi-Maskawa mixing* (CKM) and can be expressed by applying the mixing matrix on the vector of  $d$ ,  $s$ , and  $b$  mass eigenstates:

$$\begin{pmatrix} d' \\ s' \\ b' \end{pmatrix} = \begin{pmatrix} V_{ud} & V_{us} & V_{ub} \\ V_{cd} & V_{cs} & V_{cb} \\ V_{td} & V_{ts} & V_{tb} \end{pmatrix} \begin{pmatrix} d \\ s \\ b \end{pmatrix}, \tag{1.3}$$

where the matrix elements depend on the four parameters of the Standard Model.

## 1.2 Cross Sections in Colliding Beam Experiments

The beams in colliders travel in bunches of particles. When two bunches collide with each other the expected number of interactions (events) in a small volume  $d^3r$  and a time interval  $dt$  is

$$dN = \rho_1(\vec{r}, t) \rho_2(\vec{r}, t) |\vec{u}| \sigma d^3r dt , \quad (1.4)$$

where  $\rho_1$  and  $\rho_2$  are the particle densities (the number of particles per volume) for each bunch,  $|\vec{u}| = \sqrt{|\dot{\vec{r}}_1 - \dot{\vec{r}}_2|^2 - |\dot{\vec{r}}_1 \times \dot{\vec{r}}_2|^2}$  is the relative speed of bunches with respect to each other,  $\sigma$  is the *cross section* (the invariant measure of the probability) of the interaction. The cross section has dimension of area (unit  $cm^2$  or barn  $1 \text{ b} \equiv 10^{-24} cm^2$ ), and it can be visualized as the area presented by the *target* particle, which must be hit by the point-like *projectile* particle for an interaction to occur.

The collider intensity of the machine is called the *luminosity*, which is defined as the time average of the quantity

$$L = \left\langle \int \rho_1(\vec{r}, t) \rho_2(\vec{r}, t) |\vec{u}| d\vec{r} \right\rangle , \quad (1.5)$$

which has dimension of inverse area per second (unit  $cm^{-2}s^{-1}$ ). Using the definition of luminosity in Equation 1.4 we can express the average event rate (counts per unit of time) for a given process simply as

$$\frac{dN}{dt} = L \sigma . \quad (1.6)$$

For the beams traveling with the speed of light  $c$  inside the collider storage rings the Equation 1.5 can be rewritten as

$$L = 2cf_0B \int \rho_1(x, y, z - ct) \rho_2(x, y, z + ct) d\vec{r} dt , \quad (1.7)$$

where  $f_0$  is the frequency of beam rotation,  $B$  is the number of particle bunches distributed evenly across the storage ring. The  $\hat{z}$  axis of reference frame in this case is chosen such that at any given time it coincides with the direction of motion for the

first beam. Usually the bunch particle densities are assumed Gaussian both in the direction of traveling and transverse plane. In this case we can further parametrize the luminosity in Equation 1.8 as [13]

$$L = \frac{f_0 B N_1 N_2}{4\pi\sqrt{2\pi}} \int \frac{e^{-\frac{1}{2}(\frac{z-z_0}{\sigma_z})^2}}{\sigma_x(z)\sigma_y(z)\sigma_z} dz, \quad (1.8)$$

where  $z_0$  is the position of maximum collision intensity,  $\sigma_z$  is the width of the luminous region along the beam direction,  $\sigma_x(z)$  and  $\sigma_y(z)$  is the transverse widths of the bunches.

To derive a rate from Equation 1.6, we also need the cross section  $\sigma$ . The theoretical values of cross sections for the type of  $a + b \rightarrow n$ -particles processes can be calculated using the following canonical expression [14]:

$$d\sigma = (2\pi)^4 \frac{\langle \sum |M|^2 \rangle \delta^4(P_a + P_b - \sum_{i=1}^n P_i)}{4\sqrt{(P_a \cdot P_b)^2 - m_a^2 m_b^2}} \prod_{i=1}^n \frac{d^3 p_i}{(2\pi)^3 2E_i}, \quad (1.9)$$

where  $\langle \sum |M|^2 \rangle$  is the square of absolute value of *matrix element* summed over the final states and averaged over the states of colliding particles;  $P_a$ ,  $P_b$ ,  $P_i$  are the four-momentum of initial and final particles;  $m_a$ ,  $m_b$  are the masses of colliding particles;  $E_i$ ,  $\vec{p}_i$  are the energy and momentum of final particles. The delta-function in Equation 1.9 enforces conservation of energy-momentum during the collision process. The matrix element is calculated using the Lagrangian 1.1 according to the methods of perturbative quantum field theory.

### 1.3 W and Z Processes in Hadron Collisions

Electroweak interactions at the collider experiments manifest themselves as production of W or Z bosons followed by their subsequent decay into a set of final state particles. For hadron colliders the decay into leptons is currently the only useful channel of weak boson detection, since the abundant presence of QCD processes overwhelms the hadronic channel.



The dominant  $W$  and  $Z$  processes are quark-antiquark vector boson production as shown in Figures 1.1–1.2.

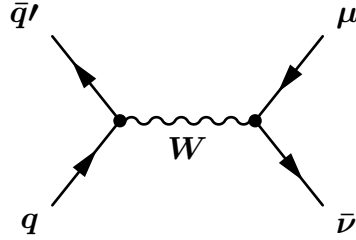


**Figure 1.1.** Feynman diagrams for the dominant  $W$  hadronic production processes with muonic decay.

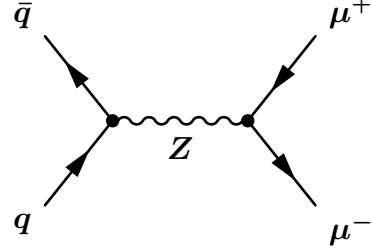


**Figure 1.2.** Feynman diagrams for the dominant  $Z$  hadronic production processes with muonic decay.

The left vertices on these diagrams represent the quark production of  $W$  and  $Z$  bosons, and they can be used for  $\sigma(q\bar{q}' \rightarrow W)$  and  $\sigma(q\bar{q} \rightarrow Z)$  cross section calculations. The distance between left and right vertices characterize the lifetime of the vector bosons before they decay. In our case the right vertices express the decay of  $W$  and  $Z$  bosons in muons.

Once an unstable particle is produced it decays with the rate  $\Gamma$  inversely proportional to its lifetime  $\tau$  in its rest frame, according to the *uncertainty principle*:

$$\tau\Gamma = 1 , \quad (1.10)$$

where  $\tau$  is also known as the *proper lifetime* of the particle and  $\Gamma$  is also known as the *full width* of the particle, which expresses the uncertainty of the particle energy. The decay rate of a particle to one particular final state  $i$  is described by the *partial width*  $\Gamma_i$ . The full width of a particle is the sum of its partial widths over all possible decay channels:

$$\Gamma = \sum_i \Gamma_i . \quad (1.11)$$

The ratio of a particle partial width  $\Gamma_\ell$  to its full width  $\Gamma$  called *branching ratio*:

$$BR(V \rightarrow \ell) = \frac{\Gamma_\ell}{\Gamma} = \frac{\Gamma_\ell}{\sum_i \Gamma_i} . \quad (1.12)$$

The partial width of a particle decay into a final state with  $n$ -particles can be calculated using the following canonical expression [14]:

$$d\Gamma(V \rightarrow a + b + \dots) = (2\pi)^4 \frac{\langle \sum |M|^2 \rangle \delta^4(P_V - \sum_{i=1}^n P_i)}{2m_V} \prod_{i=1}^n \frac{d^3 p_i}{(2\pi)^3 2E_i}, \quad (1.13)$$

where  $\langle \sum |M|^2 \rangle$ —the square of absolute value of *matrix element* summed over the final states and averaged over the states of decaying particle;  $P_V$ ,  $P_i$ —four-momentum of initial and final particles;  $m_V$ —the mass of decaying particles;  $E_i, \vec{p}_i$ —energy and momentum of final particles. The delta-function in Equation 1.13 enforces conservation of energy-momentum during the decay process. Similar to Equation 1.9 the matrix element is calculated using the Lagrangian 1.1 according to the methods of perturbative quantum field theory.

The process of a particle production and decay can be expressed quantitatively as a product of production cross section and decay branching ratio:

$$\sigma(p\bar{p} \rightarrow W \rightarrow X) = \sigma(p\bar{p} \rightarrow W) \cdot BR(W \rightarrow X) \quad (1.14)$$

$$\sigma(p\bar{p} \rightarrow Z \rightarrow Y) = \sigma(p\bar{p} \rightarrow Z) \cdot BR(Z \rightarrow Y), \quad (1.15)$$

where the calculations of production cross sections and the branching ratios are described below in Sections 1.3.3–1.3.2.

### 1.3.1 Particle Production in Hadron Collisions

In the processes where two leptons scatter off each other the inelastic collision outcomes confirm the structureless lepton hypothesis for the entire range of attainable energies. Similar *leptoproduction* processes have been carried out to study the structure of the hadrons, where the structureless lepton used as projectile scatters off a hadronic target. *Deep inelastic scattering* in leptoproduction processes have revealed the composite structure of a hadron, in which *partons* are the building blocks of the particle. Partons were further identified as quarks and gluons through the observation of hadronic jets in the processes  $e^+e^- \rightarrow 2 \text{ jets}, 3 \text{ jets}$  in which 2 and 3 jet channels are

represented by  $e^+e^- \rightarrow q\bar{q}$ ,  $e^+e^- \rightarrow q\bar{q}g$  reactions respectively. The measured rates of these reactions confirmed that quarks and gluons are *color-charged* particles and there are 3 color types for every quark flavor and 8 color types of gluons.

The parton model can be used to describe hadron-hadron collisions. A hadron-hadron scattering with the parton subprocess is illustrated in Figure 1.3. Here  $A$  and  $B$  are the incident hadrons,  $a$  and  $b$  are the partons merging into our final state particle  $V$ . The various scattered and spectator partons will always fragment into final state hadrons  $X$  shown as double lines in the figure.

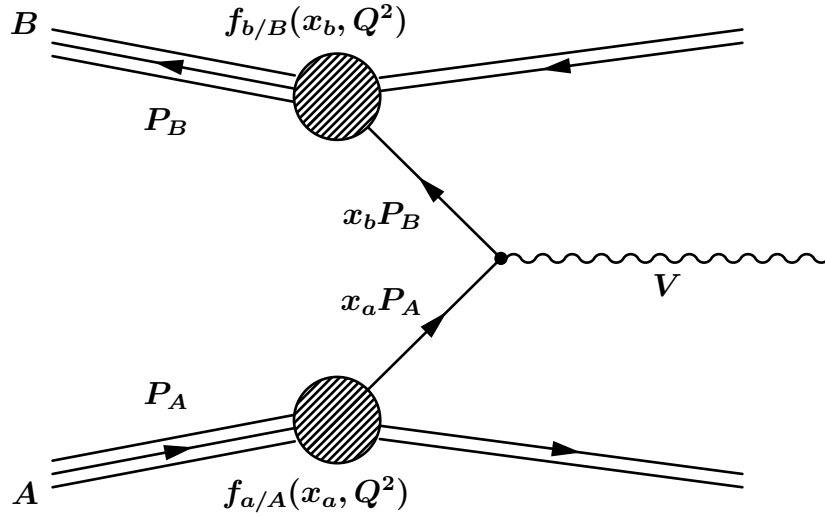


**Figure 1.3.** Hadron-hadron collision via a hard parton subprocess.

When the mass of particle  $V$  is large enough ( $>10 \text{ GeV}/c^2$ ) the cross section  $\sigma$  for inclusive hadronic production  $A + B \rightarrow V + X$  can be obtained by using the subprocess cross section  $\hat{\sigma}$  for partonic production  $a + b \rightarrow V + X$  [15]

$$\sigma = \sum_{a,b=q,\bar{q},g} C_{ab} \int \hat{\sigma} f_{a/A}(x_a, Q^2) f_{b/B}(x_b, Q^2) dx_a dx_b, \quad (1.16)$$

where  $f_{a/A}(x_a, Q^2)$ —the parton density of  $a$  in hadron  $A$ ,  $x_b$ —the longitudinal momentum fraction of parton  $b$  in hadron  $B$ ,  $Q$ —typical momentum transfer in the partonic process,  $C_{ab}$ —the parton color-averaging factor equal to  $\frac{1}{9}$  for quark-quark,  $\frac{1}{24}$  for quark-gluon, and  $\frac{1}{64}$  for gluon-gluon productions.

Typically, the masses of colliding hadrons are negligible comparing to their energies. In this case one can establish the following relation:

$$\hat{s} = (x_a P_a + x_b P_b)^2 = 2x_a x_b P_a P_b = x_a x_b (P_a + P_b)^2 = x_a x_b s = \tau s, \quad (1.17)$$

where  $\hat{s}$ ,  $s$ —the square of invariant mass of  $ab$  and  $AB$  systems respectively,  $\tau$ —a new variable for  $x_a x_b$  substitution.

Another useful variable is the *rapidity* of the  $ab$  system in the  $AB$  center of mass reference frame. Rapidity  $y$  is defined as:

$$y = \frac{1}{2} \ln \left[ \frac{E_V + (\vec{p}_V \cdot \hat{z})}{E_V - (\vec{p}_V \cdot \hat{z})} \right] = \frac{1}{2} \ln \left[ \frac{E_a + (\vec{p}_a \cdot \hat{z}) + E_b + (\vec{p}_b \cdot \hat{z})}{E_a - (\vec{p}_a \cdot \hat{z}) + E_b - (\vec{p}_b \cdot \hat{z})} \right] = \frac{1}{2} \ln \frac{x_a}{x_b}, \quad (1.18)$$

where  $E_a = x_a E_A$ ,  $E_b = x_b E_B$  and in the case of massless hadrons  $(\vec{p}_a \cdot \hat{z}) = x_a E_A$ ,  $(\vec{p}_b \cdot \hat{z}) = -x_b E_B$ . In the  $AB$  center of mass reference frame  $E_A = E_B$ .

Using our variable transformation  $x_a = \sqrt{\tau} e^y$ ,  $x_b = \sqrt{\tau} e^{-y}$  in Equation 1.16 we get:

$$\frac{d\sigma}{d\tau dy} = \sum_{a,b=q,\bar{q},g} C_{ab} \hat{\sigma} f_{a/A}(\sqrt{\tau} e^y, Q^2) f_{b/B}(\sqrt{\tau} e^{-y}, Q^2). \quad (1.19)$$

In case when particle  $V$  is massless, the Equation 1.18 coincides with the definition of *pseudorapidity*  $\eta$ :

$$\eta = \frac{1}{2} \ln \left[ \frac{|\vec{p}_V| + (\vec{p}_V \cdot \hat{z})}{|\vec{p}_V| - (\vec{p}_V \cdot \hat{z})} \right] = -\ln \left[ \tan \left( \frac{\theta}{2} \right) \right], \quad (1.20)$$

where  $\theta$ —center-of-mass scattering angle. For many high energy processes the dependence on the particle masses is negligible and therefore the rapidity and pseudorapidity become equivalent. Experimentally this is very convenient, since one needs to know only the angle  $\theta$ .

If  $V$  is an unstable particle we can use the relativistic Breit-Wigner formula:

$$\hat{\sigma} = 12\pi \frac{\hat{s}}{m_V^2} \frac{\Gamma(V \rightarrow ab) \Gamma(V \rightarrow F)}{(\hat{s} - m_V^2)^2 + m_V^2 \Gamma^2(V)} \approx 12\pi^2 \frac{\Gamma(V \rightarrow ab) \Gamma(V \rightarrow F)}{m_V \Gamma(V)} \delta(\hat{s} - m_V^2), \quad (1.21)$$

where  $\Gamma(V \rightarrow ab)$ ,  $\Gamma(V \rightarrow F)$  are the decay widths of  $V$  into the initial state  $ab$  and the final state  $F$  respectively,  $m_V$  is the mass of  $V$ . The last term has the delta-function

$\delta(\hat{s} - m_V^2)$  as the result of the “narrow width” approximation, when  $\Gamma(V) \ll m_V$ ,  $\sqrt{\hat{s}}$ .

We put this expression for  $\hat{\sigma}$  into our Equation 1.19 for  $\sigma$  and integrate over  $\tau$ :

$$\frac{d\sigma}{dy} = \sum_{a,b=q,\bar{q},g} C_{ab} 12\pi^2 \frac{\Gamma(V \rightarrow ab)\Gamma(V \rightarrow F)}{m_V^3 \Gamma(V)} x_a x_b f_{a/A}(x_a, m_V^2) f_{b/B}(x_b, m_V^2), \quad (1.22)$$

where  $x_a$  is evaluated at  $\frac{m_V}{\sqrt{s}}e^y$  and  $x_b$  is evaluated at  $\frac{m_V}{\sqrt{s}}e^{-y}$ . Here it is assumed that  $Q^2 = m_V^2$  is the appropriate scale for the parton distributions.

Figures 1.4–1.5 show the new  $xf(x)$  parton distributions in proton for two different energy scales [16].

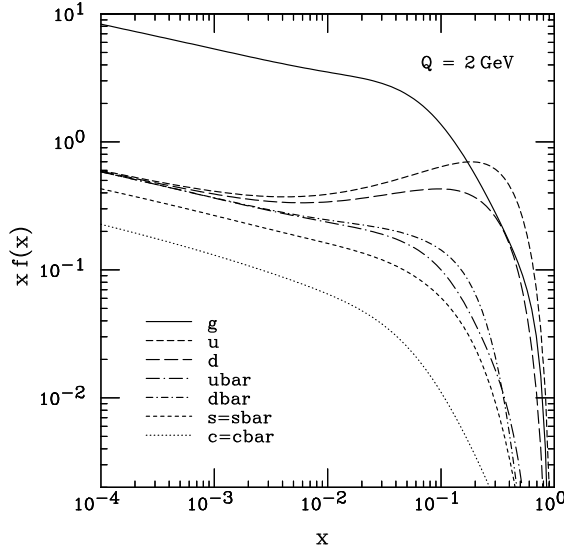


**Figure 1.4.** The CTEQ6M quark and gluon distribution functions for proton at the energy scale of  $Q^2 = 2$  GeV.

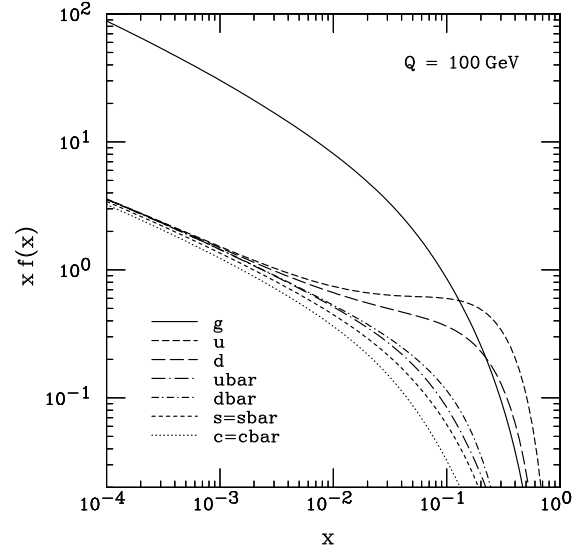


**Figure 1.5.** The CTEQ6M quark and gluon distribution functions for proton at the energy scale of  $Q^2 = 100$  GeV.

According to the parton model, the proton is a combination of  $u$ - $u$ - $d$  “valence” quarks that are accompanied by gluons and quark-antiquark pairs of “sea” quarks. The parton distribution functions of the antiproton are related to those of the proton:

$$\begin{aligned} u_p(x, Q^2) &= \bar{u}_{\bar{p}}(x, Q^2) & \bar{u}_p(x, Q^2) &= u_{\bar{p}}(x, Q^2) \\ d_p(x, Q^2) &= \bar{d}_{\bar{p}}(x, Q^2) & \bar{d}_p(x, Q^2) &= d_{\bar{p}}(x, Q^2) \\ g_p(x, Q^2) &= g_{\bar{p}}(x, Q^2) \\ s_p(x, Q^2) &= s_{\bar{p}}(x, Q^2) = \bar{s}_p(x, Q^2) = \bar{s}_{\bar{p}}(x, Q^2) \\ c_p(x, Q^2) &= c_{\bar{p}}(x, Q^2) = \bar{c}_p(x, Q^2) = \bar{c}_{\bar{p}}(x, Q^2). \end{aligned} \quad (1.23)$$

### 1.3.2 $W$ and $Z$ Decay

The production of  $W$  boson is immediately followed by subsequent leptonic or hadronic decay:  $W \rightarrow \ell\nu$  or  $W \rightarrow q\bar{q}'$ , where  $\ell = e, \mu, \tau$ , and  $q$  or  $q'$  represent one of the quarks  $u, d, c, s$  or  $b$  (but not  $t$  since top quark is heavier than the  $W$  boson).

In the leading order for massless fermions, the partial decay width of  $W \rightarrow \ell\nu$  is [15]

$$\Gamma_W^0 = \frac{G_F M_W^3}{6\sqrt{2}\pi} , \quad (1.24)$$

where the available leptonic channels are  $W \rightarrow e\bar{\nu}, \mu\bar{\nu}, \tau\bar{\nu}$ . Some Standard Model corrections are absorbed in the measured physical values of  $M_W$  and  $G_F$ . Including additional electroweak corrections the Standard Model prediction yields [14]:

$$\Gamma(W \rightarrow \ell\nu) = 226.4 \pm 0.3 \text{ MeV}, \quad (1.25)$$

which is about 0.5 % less than our leading order calculations given by Equation 1.24.

In addition to the three leptonic decays  $W$  has two dominant hadronic decay channels  $W \rightarrow q\bar{q}'$ , where  $q$  is  $u$  or  $c$ , and  $\bar{q}'$  is the appropriate CKM mixture of  $d$  and  $s$ . Other hadronic decay channels are greatly suppressed by CKM off-diagonal matrix elements  $|V_{qq'}|^2$ .

Considering the three color charges for quarks, the partial width of  $W \rightarrow q\bar{q}'$  is:

$$\Gamma(W \rightarrow q\bar{q}') = 3|V_{qq'}|^2 \Gamma_W^0 [1 + \alpha_s(M_W^2)/\pi + \mathcal{O}(\alpha_s^2)] , \quad (1.26)$$

where the first order QCD correction are applied to the final state.

Sum over all nine leptonic and hadronic channels yields a total width of  $W$

$$\Gamma(W) = 3\Gamma_W^0 \left\{ 1 + \left[ 1 + \alpha_s(M_W^2)/\pi + \mathcal{O}(\alpha_s^2) \right] \sum_{\text{no top}} |V_{qq'}|^2 \right\} , \quad (1.27)$$

and the leptonic decay branching ratio

$$BR(W \rightarrow \ell\nu) = \frac{1}{3} \left\{ 1 + \left[ 1 + \alpha_s(M_W^2)/\pi + \mathcal{O}(\alpha_s^2) \right] \sum_{\text{no top}} |V_{qq'}|^2 \right\}^{-1} , \quad (1.28)$$

predicting  $\Gamma(W) = 2.0921 \pm 0.0025 \text{ GeV}$  and  $BR(W \rightarrow \ell\nu) = 0.1082 \pm 0.0002$  [14].

For  $Z$  decay the partial width value depends not only on the leptonic or hadronic decay channel but also on the weak isospin value of the final state fermions. According to the Standard Model, quarks  $u$ ,  $c$ ,  $t$  and neutrinos have positive weak isospin, and quarks  $d$ ,  $s$ ,  $b$  and leptons have negative weak isospin. Since top quark mass is heavier than the mass of  $Z$ , the decay of  $Z$  is limited to 11 channels.

The leading order partial decay widths of  $Z \rightarrow f\bar{f}$  are [15]:

$$\Gamma(Z \rightarrow \nu\bar{\nu}) = \frac{G_F M_Z^3}{12\sqrt{2}\pi} = \Gamma_Z^0 \quad (1.29)$$

$$\Gamma(Z \rightarrow \ell\bar{\ell}) = \Gamma_Z^0(1 - 4\sin^2\theta_W + 8\sin^4\theta_W) \quad (1.30)$$

$$\Gamma(Z \rightarrow u\bar{u}) = 3\Gamma_Z^0(1 - \frac{8}{3}\sin^2\theta_W + \frac{32}{9}\sin^4\theta_W)[1 + \alpha_s(M_Z^2)/\pi + \mathcal{O}(\alpha_s^2)] \quad (1.31)$$

$$\Gamma(Z \rightarrow d\bar{d}) = 3\Gamma_Z^0(1 - \frac{4}{3}\sin^2\theta_W + \frac{8}{9}\sin^4\theta_W)[1 + \alpha_s(M_Z^2)/\pi + \mathcal{O}(\alpha_s^2)] , \quad (1.32)$$

where for hadronic decay modes 3 type of colors and next order QCD effects are taken into account. Equation 1.31 can also be applied to calculate  $Z \rightarrow c\bar{c}$  decay and Equation 1.32 is the same for  $Z \rightarrow s\bar{s}$  and  $Z \rightarrow b\bar{b}$  processes.

A sum over all leptonic and quark flavors yields a total width of  $Z$ :

$$\Gamma(Z) = \Gamma_Z^0 \left\{ 6 - 12\sin^2\theta_W + 24\sin^4\theta_W + [1 + \alpha_s(M_Z^2)/\pi + \mathcal{O}(\alpha_s^2)] \left( 15 - 28\sin^2\theta_W + \frac{88}{3}\sin^4\theta_W \right) \right\} , \quad (1.33)$$

and leptonic decay branching ratio

$$BR(Z \rightarrow \ell\bar{\ell}) = (1 - 4\sin^2\theta_W + 8\sin^4\theta_W) \left\{ 6 - 12\sin^2\theta_W + 24\sin^4\theta_W + [1 + \alpha_s(M_W^2)/\pi] \left( 15 - 28\sin^2\theta_W + \frac{88}{3}\sin^4\theta_W \right) \right\}^{-1} . \quad (1.34)$$

The predicted values [14] for total width  $\Gamma(Z) = 2.4961 \pm 0.0012$  GeV and leptonic branching ratio  $BR(Z \rightarrow \ell\bar{\ell}) = 3.365 \pm 0.002$  % agree very well with the recent measurements from LEP2  $\Gamma(Z) = 2.491 \pm 0.007$  GeV and  $BR(Z \rightarrow \ell\bar{\ell}) = 3.366 \pm 0.002$  %.

### 1.3.3 Hadronic W and Z Production

In  $p\bar{p}$  collisions, W bosons are mostly produced by processes of the type  $u\bar{d} \rightarrow W^+$  or  $\bar{u}d \rightarrow W^-$ . The contributions from  $u\bar{s} \rightarrow W^+$  or  $\bar{u}s \rightarrow W^-$  types are suppressed by the Cabibbo mixing. The distributions of quarks in the proton are described by parton distribution functions through the fraction of longitudinal momentum fraction  $x$ . Using Equation 1.26 for  $\Gamma(W \rightarrow q\bar{q}')$  and Equation 1.23 for parton distributions of the proton and antiproton we can rewrite Equation 1.22 assuming  $\Gamma(W) = \Gamma(W \rightarrow F)$

$$\frac{d\sigma}{dy}(p\bar{p} \rightarrow W^+) = K \frac{4\pi^2 \Gamma_W^0}{M_W^3} x_a x_b \left\{ |V_{ud}|^2 [u(x_a)d(x_b) + \bar{d}(x_a)\bar{u}(x_b)] + |V_{us}|^2 [u(x_a)s(x_b) + \bar{s}(x_a)\bar{u}(x_b)] \right\}, \quad (1.35)$$

where arguments  $x_a, x_b$  in quark and antiquark densities are evaluated through pseudorapidity:  $x_a = M_W/\sqrt{s}e^y$  and  $x_b = M_W/\sqrt{s}e^{-y}$  at the center-of-mass energy  $\sqrt{s}=1.96$  TeV for Tevatron  $p\bar{p}$  collisions.

The corresponding differential cross section for  $W^-$  production can be obtained by interchanging  $x_a$  with  $x_b$  in the arguments of quark and antiquark densities.

To account for the next order QCD effects in quark interactions, an additional  $K$ -factor is introduced in the cross-section expression:

$$K = 1 + \frac{8\pi}{9} \alpha_s(M_W^2) + \mathcal{O}(\alpha_s^2), \quad (1.36)$$

which is evaluated at the  $W$  mass energy scale.

Similarly, the cross section for production of  $Z$  boson is:

$$\frac{d\sigma}{dy} = K \frac{4\pi^2 \Gamma_Z^0}{M_Z^3} x_a x_b \left\{ \left(1 - \frac{8}{3} \sin^2 \theta_W + \frac{32}{9} \sin^4 \theta_W\right) [u(x_a)u(x_b) + \bar{u}(x_a)\bar{u}(x_b)] + \right. \\ \left. \left(1 - \frac{4}{3} \sin^2 \theta_W + \frac{8}{9} \sin^4 \theta_W\right) [d(x_a)d(x_b) + \bar{d}(x_a)\bar{d}(x_b) + s(x_a)s(x_b) + \bar{s}(x_a)\bar{s}(x_b)] \right\}, \quad (1.37)$$

with the Drell-Yan  $K$ -factor:

$$K = 1 + \frac{4\alpha_s(M_Z^2)}{6\pi} \left(1 + \frac{4}{3} \pi^2\right) + \mathcal{O}(\alpha_s^2), \quad (1.38)$$

evaluated at the  $Z$  mass energy scale.



## 1.4 Measurement of $W$ Width from the Cross Section Ratio

The  $p\bar{p}$  production rate of  $W$  and  $Z$  bosons is described through the cross section quantity. The probability for these bosons to decay to a muon in a final state is defined as the branching ratio. We can express the product of the production cross section and the branching ratio for a vector boson decay in the muon channel in terms of the measured variables:

$$\sigma(p\bar{p} \rightarrow V) \cdot BR(V \rightarrow \mu X) = \frac{N - B}{A\epsilon \int L dt}, \quad (1.39)$$

where  $N$  is the number of candidate events passing the selection,  $B$  is the estimated number of background events,  $A$  is the detector acceptance,  $\epsilon$  is the efficiency of the selection cuts,  $\int L dt$  is the luminosity integral which has dimension of inverse area (unit  $cm^{-2}$  or inverse picobarn  $1 \text{ pb}^{-1} \equiv 10^{36} \text{ cm}^{-2}$ ).

When taking the ratio of  $p\bar{p}$  production cross section for  $W$  and  $Z$  in muon channel

$$R = \frac{\sigma(p\bar{p} \rightarrow W) \cdot BR(W \rightarrow \mu\nu)}{\sigma(p\bar{p} \rightarrow Z) \cdot BR(Z \rightarrow \mu\mu)} = \frac{\sigma(p\bar{p} \rightarrow W)}{\sigma(p\bar{p} \rightarrow Z)} \frac{\Gamma(W \rightarrow \mu\nu)}{\Gamma(W)} \frac{\Gamma(Z)}{\Gamma(Z \rightarrow \mu\mu)} \quad (1.40)$$

we can extract the value of the branching ratio  $BR(W \rightarrow \mu\nu) = \Gamma(W \rightarrow \mu\nu)/\Gamma(W)$  using the theoretical calculation of the production cross sections and precise  $Z$  width measurements from LEP experiment [14]. This measurement promises high precision due to the fact that luminosity does not enter the expression. Also we expect complete or partial cancellation of many uncertainties in the ratio when the muon identification is the same both for  $W$  and  $Z$  selection. We can further extract the value  $W$  width parameter  $\Gamma(W)$  using the Standard Model calculation for  $W$  leptonic width  $\Gamma(W \rightarrow \ell\nu)$ .

## 1.5 Strategy of This Measurement

The initial CDF Run II measurements of the  $W \rightarrow \mu\nu$  and  $Z \rightarrow \mu^+\mu^-$  production cross sections were made in summer 2002 using  $16.5 \text{ pb}^{-1}$  of data [17, 18] and in winter

2003 using much larger data sample of  $72 \text{ pb}^{-1}$  and utilizing greater acceptance for  $Z$  selection [19, 20].

Improved measurements of these cross sections can now be made using event samples collected through the beginning of September, 2003 shutdown which are considerably larger than those used for the previous measurements, which allows us to reduce significantly both statistical and systematic uncertainties of our result.

This work describes a new updated measurement of the ratio  $R$  of inclusive  $W$  and  $Z$  boson cross sections in proton-antiproton collisions at 1.96 TeV using about  $194 \text{ pb}^{-1}$  of high- $P_T$  muon data collected by the CDF detector [21]. We describe how different parameters entering Equation 1.39 are measured both for  $W$  and  $Z$  bosons. We also derive the values and uncertainties for acceptance and efficiency ratios that enter the Equation 1.40. At the end of the note we discuss the significance of the ratio measurement in light of existing information on  $W$  and  $Z$  production and decay.

## CHAPTER 2

# The Tevatron and The Collider Detector

The data used in this analysis were collected by the Collider Detector located at the Fermi National Accelerator Laboratory<sup>1</sup> near Batavia, Illinois. CDF<sup>2</sup> utilizes proton-antiproton collisions delivered by the Tevatron accelerator complex. This experiment has been known for the most significant discoveries in High Energy Physics, such as the observation of the Top quark during Run I data taking (1992-1996). Recently, both detector and accelerator have been upgraded for enhanced data taking in Run II. The upgraded Tevatron delivers instantaneous luminosity of up to  $5 \cdot 10^{31} \text{ cm}^{-2} \text{ s}^{-1}$  which is a great improvement compared to Run I peak luminosity of  $2 \cdot 10^{31} \text{ cm}^{-2} \text{ s}^{-1}$ . Also the beam energy has been boosted from 900 to 980 GeV, to intensify the occurrence for many interesting physics processes. To accommodate new accelerator operation, most of the CDF sub-detector systems have been upgraded [23]. The increased rate of beam collisions in Run II requires the new trigger and data acquisition system as well as a redesigned silicon vertex detector and tracking chamber. The detailed overview of Run II upgraded CDF and Tevatron is presented further in this chapter.

### 2.1 Tevatron at Fermilab

The Fermilab Tevatron is a  $p\bar{p}$  superconducting collider, which currently operates with 36 proton on 36 antiproton bunches at a center-of-mass energy of  $\sqrt{s} = 1.96 \text{ TeV}$ .

---

<sup>1</sup>abbreviated as FNAL or Fermilab

<sup>2</sup>abbreviation for Collider Detector at Fermilab

Until the completion of Large Hadron Collider in CERN, Tevatron is the world highest energy  $p\bar{p}$  collider.

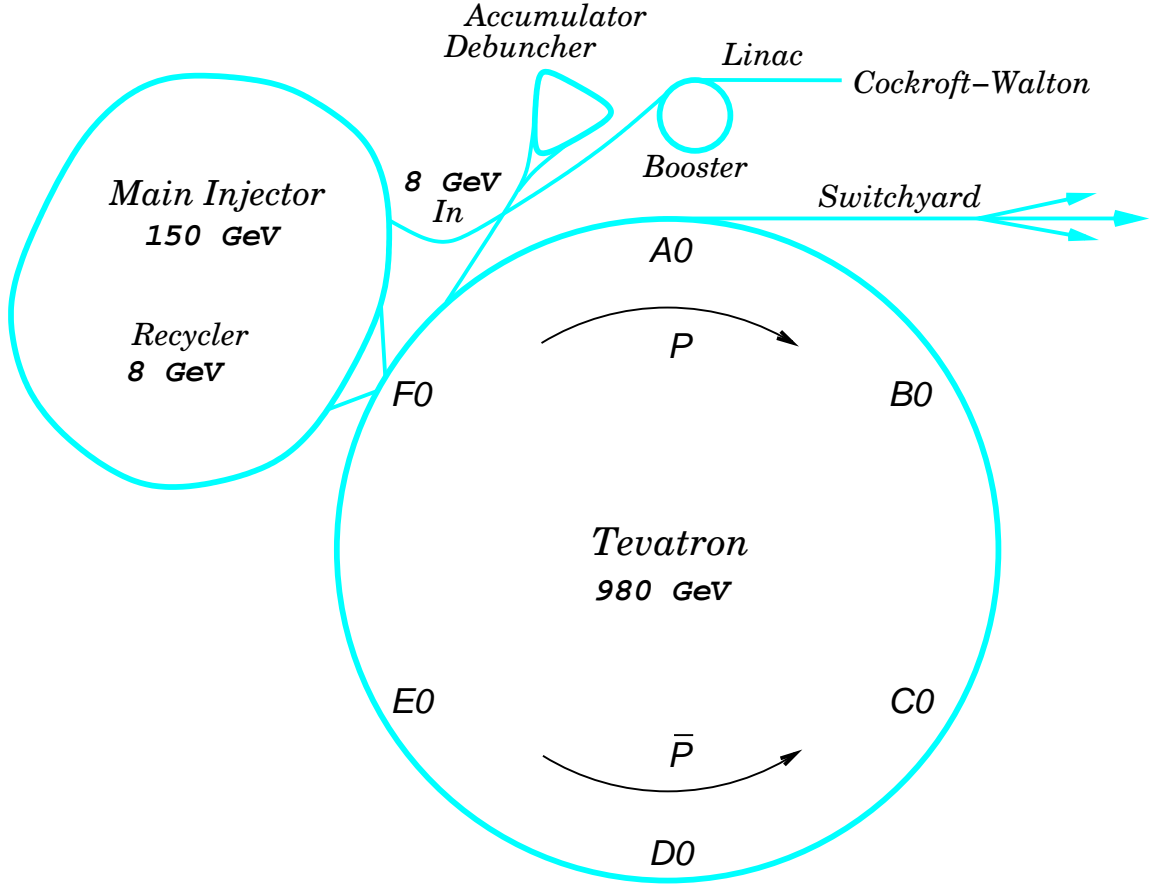


**Figure 2.1.** Schematic view of Tevatron

The collider complex comprises an accelerator chain shown in Figure 2.1. The cycle starts with obtaining protons from the ionized hydrogen atoms  $H^-$ , which are accelerated to 750 KeV by *Cockroft-Walton* electrostatic accelerator. Pre-accelerated  $H^-$  ions are then injected into *Linac* where they gain an energy up to 400 MeV when passing through the 150 m long chain of radio-frequency (RF) accelerator cavities. To form protons, the  $H^-$  ions pass through a carbon foil which strips electrons off the

protons. Inside the *Booster* the protons are merged into the bunches and accelerated to an energy of 8 GeV prior to entering the *Main Injector*, which is a synchrotron 3 km in circumference. In the Main Injector the proton bunches are accelerated further to an energy of 150 GeV and coalesced together to high density prior to injection into the *Tevatron*, a superconducting collider 6 km in circumference. In the Tevatron a total of 36 proton bunches are accelerated to an energy of 980 GeV.

The production of the antiproton beam is significantly more complicated. The cycle starts with projecting 120 GeV proton beam from the Main Injector onto a stainless steel target. Such process produces a variety of different particles, among which are antiprotons. It takes about 100,000 protons to make one or two antiprotons. These antiprotons are separated from other particles by focusing through lithium lenses prior to injecting into the *Debuncher*, which decreases the momentum spread of the particles utilizing the “stochastic cooling” technique [22]. After that, the continuous antiproton beam directed into the *Accumulator* where the antiprotons are stored at an energy of 8 GeV and stacked to the concentration of  $10^{12}$  particles per bunch, which takes up to 12 hours on average. The antiproton bunches are then injected into the Main Injector and accelerated to 150 GeV. Finally, 36 bunches of antiprotons are inserted in the Tevatron where they attain an energy of 980 GeV. The proton and antiproton bunches circulate the Tevatron in the opposite directions. Their orbits cross at the *B0* and *D0* collision points, where interactions are registered by the CDF and D0 detectors respectively.

## 2.2 Overview of CDF

The Collider Detector at Fermilab is designed to register the rich variety of high energy physics processes associated with proton antiproton collisions at Tevatron. The Run II Tevatron upgrade increases the number of bunches in each beam by a factor of six with respect to Run I making the time between two successive interactions

396 ns down from  $2.4 \mu\text{s}$ . As a result, the trigger and other detector subsystem have been rebuild from scratch to accommodate the higher collision rates. During this upgrade [23], efforts were also made to extend its geometrical coverage by adding new detector elements or enlarging the existing ones.

The machine is located at the collision hall, which is denoted as sector  $B0$  in Figure 2.1. The detailed view of CDF is shown in Figure 2.2. Only half of the drawing is shown, since the detector is forward-backward symmetric across the plane through the interaction point.

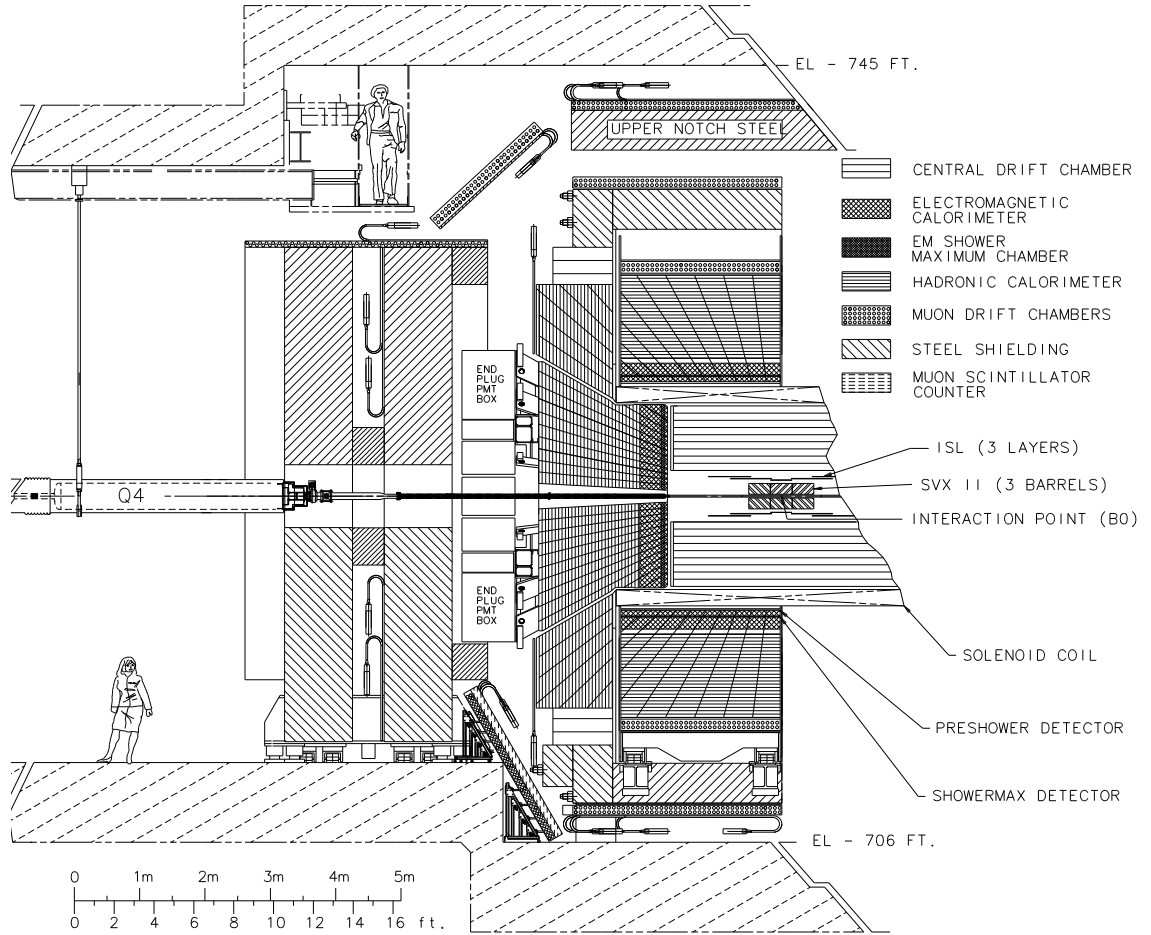


**Figure 2.2.** Elevation view of one half of the CDF II detector

The CDF reference system uses the right handed coordinate system where the  $\hat{z}$  axis is directed along the motion of proton beam, the  $\hat{x}$  axis is in the plane of the

accelerator, and the  $\hat{y}$  axis is pointing upward. To describe various detector system a polar coordinate system is often used with the polar angle  $\theta$  substituted by the pseudorapidity variable defined in Section 1.3.1.

The main bulk of the detecting volume is the tracking and calorimetry systems, which are build deliberately for the precise measurements of electroweak scale energies. The other detector parts are used for the particle identification. The rest of this chapter will contain a short review of each detector subsystem. The description starts with the inner parts and continues toward the outermost systems. We conclude this chapter with the brief examination of the on-line data acquisition system, which controls the detector operations.

## 2.3 Tracking System

Detection and tracking of charged particles is an essential part of many analyses at CDF. The operation of tracking detectors is based on the fact that charged particles ionize the matter through which they pass. The trail of ionized matter left behind by a charged particle coincides with its trajectory and is often referred to as a *track*. Throughout the history of experimental particle physics various implementations of particle tracking devices were used, varying from pioneering bubble and spark chambers to sophisticated drift chambers and semiconductor detectors.

Charged particles moving in a uniform magnetic field, as inside the CDF tracker, have a helical trajectory. By measuring the radius of curvature of the helix, particle's transverse momentum is obtained. The longitudinal component of particle's momentum is related to the helix pitch.

To have a precise measurement of charged particle's momentum, it is necessary to sample points of the trajectory on a long range. Therefore a good spectrometer requires a large tracking volume. On the other hand, by making a few, very accurate measurements of the track position near the interaction point, it is possible to delimit

a narrow region of space, where the particle might have been produced. In this case, the detection does not require a long trajectory range, instead, it has to be very close to the collision point and it must withstand high density of tracks.

The CDF II tracking system includes the *Silicon Vertex Detector* and *Central Outer Tracker* (COT) surrounded by the superconducting *Solenoid*. The schematic longitudinal view of CDF II tracking system is shown on Figure 2.3.

### CDF Tracking Volume

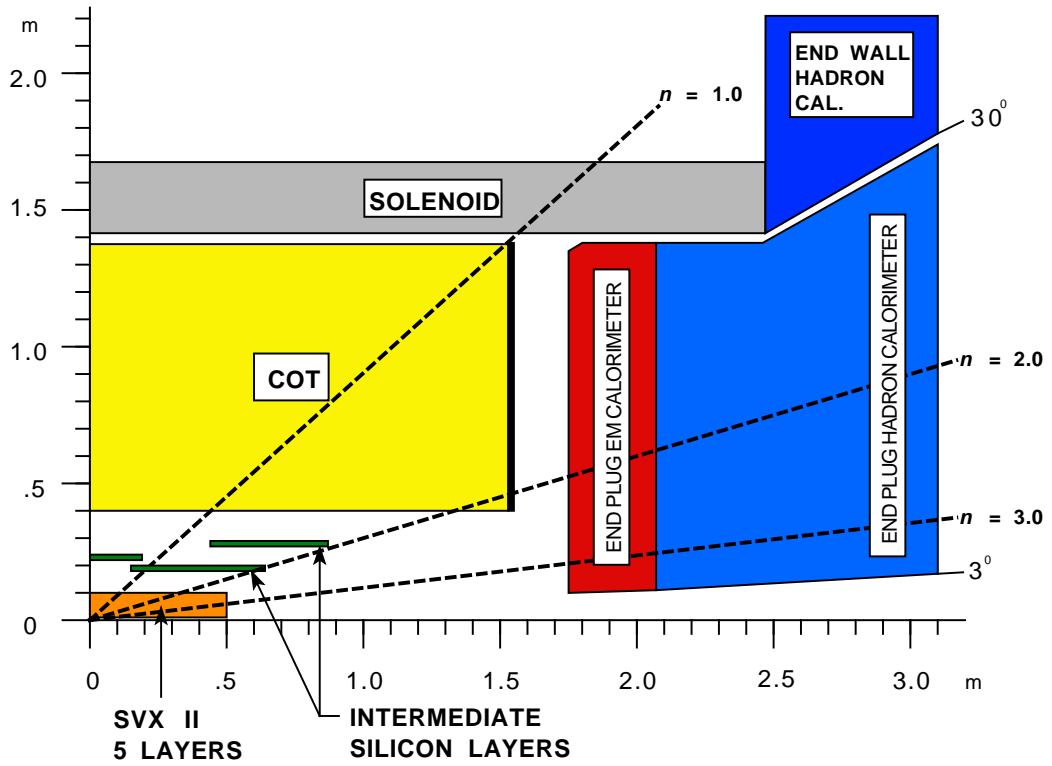


Figure 2.3. Tracking system of the CDF II detector

#### 2.3.1 Silicon Vertex Detector

Upgraded CDF silicon detectors include the following subsystems: “Layer 00” (L00), Silicon Vertex Detector (SVX II), and the Intermediate Silicon Layers (ISL). All of these systems rely on the functional unit which is a silicon microstrip detector.

Layer 00 is a single sided, radiation-hard silicon microstrip detector, placed im-



mediately outside the beam-pipe, at the radius of 1.5 cm, and surrounded by SVX as shown in Figure 2.4. Such a close proximity to the interaction point improves significantly the reconstruction of both tracks and vertexes.

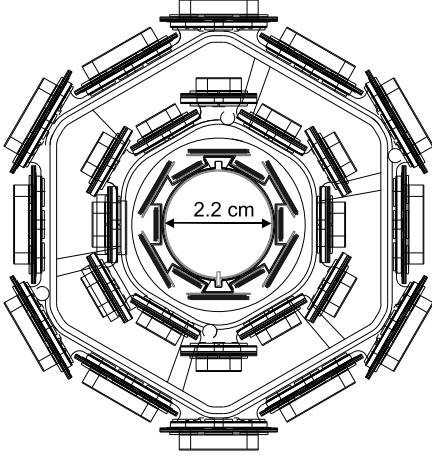


**Figure 2.4.** Transverse view of Layer 00.

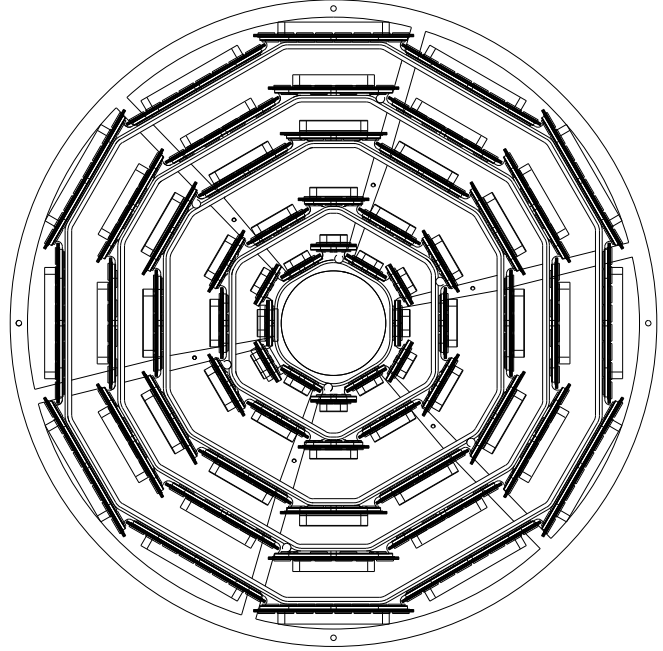


**Figure 2.5.** Transverse view of SVX II barrel.

SVX II is the Run II baseline detector. The detector spans radially from 2.5 cm to 10 cm and its transverse view is shown in Figure 2.5. It consists of five layers of double-sided silicon ladders. One side of each ladder provides measurement in the transverse plane while the other side provides additional information for complete 3-D reconstruction. SVX II extends longitudinally 45 cm on both sides of the collision point as indicated in Figure 2.3.

Similar to SVX, the ISL also consists of a double-sided silicon wafers. As shown in Figure 2.3, there is one layer placed at the radius 22 cm in the central region, and two forward layers placed at the radiuses 20 cm and 29 cm from the beam line. Combination of SVX and ISL detectors makes track reconstruction possible in the forward part of CDF, which is beyond the coverage of the COT.

### 2.3.2 Central Outer Tracker

The central outer tracker is an “open-cell drift chamber”, which lies outside the silicon detector and fills the space between radial coordinates of 40 and 138 cm, up to a  $z$  of 155 cm. Because of its large detecting volume the tracker provides an accurate measurement of track parameters.

The main constituents of any drift chamber are wires that collect ions produced by the charged particle in the gas inflating the volume. These wires are grouped together into identical *cells*, whose shape is shown on Figure 2.6. Within each cell twelve *sense* wires are placed in a proper electrostatic field, which is configured by high voltage on *field panels* and *shaper wires* with respect to *potential wires*. Cells are further joined into eight *super-layers*. Axial super-layers, in which the wires are parallel to the magnetic field, alternate with super-layers, in which the wires have a  $3^\circ$  stereo angle tilt. Stereo super-layers start with the innermost one, which contains 168 cells. Axial super-layers end at the outermost one, which contains 480 cells. The position of all eight super-layers is shown on Figure 2.7.

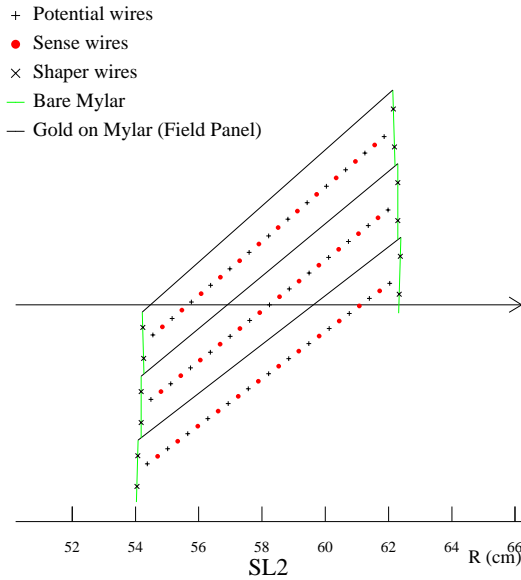


**Figure 2.6.** Cell layout for super-layer 2.

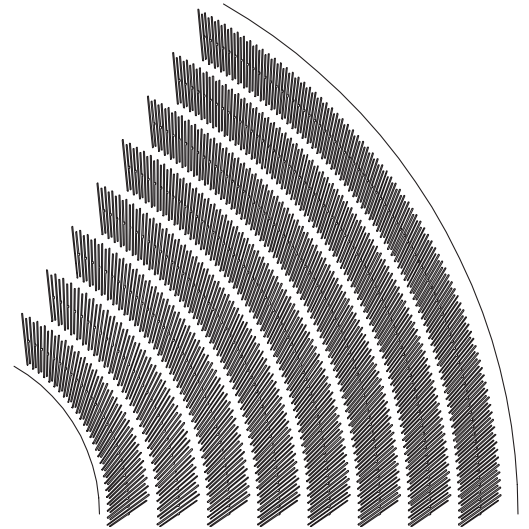


**Figure 2.7.** 1/6th view of COT east end-plate.

Once the drift time of ions from the charged particle to the sense wires is measured, it is possible to reconstruct the particle's trajectory, since the geometry of the COT and drift velocity are known. The wire readout is performed via custom-build amplifier-shaper-discriminator (ASD) 8-channel chip. The boards, containing three of these chips and reading out two adjacent cells are placed directly on the chamber end-plate. They continuously measure both the signal's leading edge and the total collected charge, which is used in many analysis for the charged particle identification. The signal is carried further to time-to-digit-converter (TDC) boards, which store the information in digital format.

The most important design requirement for COT is the ability to operate successfully at the high luminosity and collision rate of Run II. This requirement was met by choosing a small cell size and using the fast gas mixture. The COT uses the combination of Ar-Ethane-CF<sub>4</sub> gases mixed in proportion 50:35:15. This gas mixture provides a high drift speed of 88  $\mu\text{m}/\text{ns}$  at a drift field of 2.5 kV/cm.

The resolution of the measured transverse momentum has been studied using the simulation samples and has been found to be  $\delta P_T/P_T^2 = 0.30\%/ \text{GeV}/c$  for COT standalone track reconstruction and  $\delta P_T/P_T^2 = 0.12\%/ \text{GeV}/c$  for combined COT and SVX tracking.

### 2.3.3 Superconducting Solenoid

The CDF tracking system is enclosed in a superconducting solenoid, which provides a magnetic field of 1.4 T along the detector axis, over a cylindrical volume 4.8 m long and 3 m in diameter. The solenoid is made of an Al-stabilized NbTi superconductor, able to withstand currents up to 5000 A, and operating at the liquid helium temperature. The magnetic field generated by the solenoid is uniform throughout the entire tracking volume with 0.1 % accuracy.

## 2.4 Calorimeter

The calorimeter extends to  $|\eta| < 3.6$  and is used for measuring energies of jets, photons, electrons. The presence of an energetic neutrino in event is inferred through the transverse missing energy, calculated by taking a sum of energies over all calorimeter towers<sup>3</sup>. A minimum ionizing particle, such as muon, can also be identified by its small energy deposition in the calorimeter tower, through which it passes.

CDF uses scintillator sampling calorimeter, divided into separate *electromagnetic* and *hadronic* sections. The entire calorimeter is segmented into projective towers. Each tower consists of alternating layers of passive material and scintillator tiles. The signal is read via wavelength shifters (WLS) embedded in the scintillators. The light from WLS is transmitted further to photo multiplier tubes (PMT).

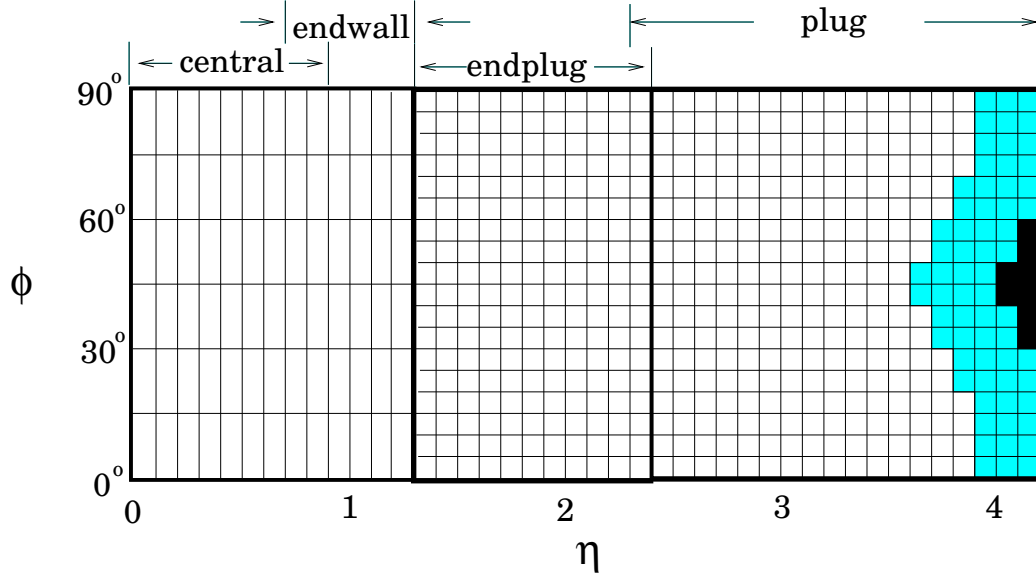


**Figure 2.8.** 1/8th of calorimeter segmentation map.

Depending on the detector pseudo-rapidity region, the calorimeter is further divided into central  $|\eta| < 1.1$  and plug  $1.1 < |\eta| < 3.6$

---

<sup>3</sup>for details refer to Chapter 5

### 2.4.1 Central Electromagnetic Calorimeter

The central electromagnetic calorimeter consists of projective towers of alternating lead and scintillator as shown in Figure 2.9. The signal is read via polymethylmethacrylate wavelength shifter, and carried via clear fiber to photomultiplier tubes.

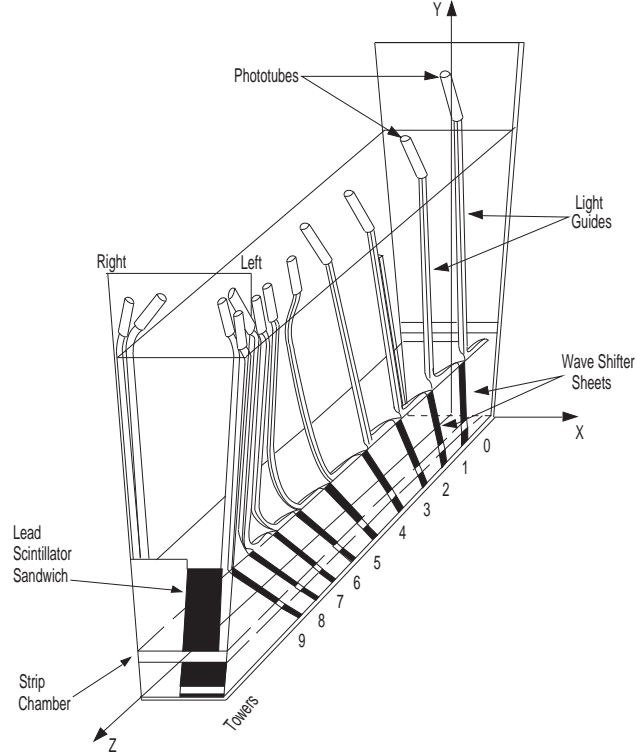


**Figure 2.9.** Central electromagnetic calorimeter wedge.

A two dimensional “strip chamber”—a *shower maximum* detector is embedded in the calorimeter. It measures the electromagnetic shower profile, developed by passing photon or electron. Another wire chamber—*central pre-radiator* (CPR) is placed in front of the calorimeter to act as a pre shower detector, which uses tracker and solenoid coil as radiators.

The nominal stochastic resolution of the central electromagnetic calorimeter is  $13.5\%/\sqrt{E_T/GeV}$ , which has been determined using the isolated electrons by matching track  $P_T$  to calorimeter  $E_T$ .

### 2.4.2 Central Hadron Calorimeter

The central and end-wall hadronic calorimeter is also sampled into projective towers and matches the geometry of central electromagnetic calorimeter described before. The passive material or radiator includes 23 iron layers.

The resolution of the central hadronic calorimeter is  $75 \% \sqrt{E_T/GeV} \oplus 3 \%$ .

### 2.4.3 Plug Calorimeter

The upgraded plug calorimeter, shown on Figure 2.10, covers the  $\eta$  region between 1.1 and 3.6. It replaces a Run I gas calorimeter, whose response was too slow for the current Run II operation conditions.

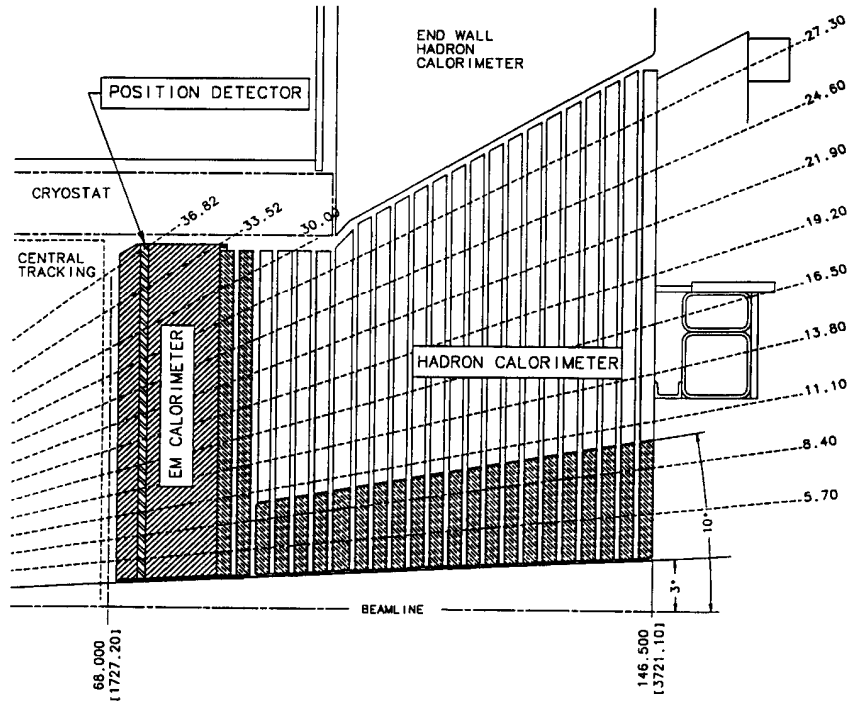


Figure 2.10. Cross section of upper part of end plug calorimeter.

The electromagnetic section of the plug calorimeter consists of 23 alternating layers of 4.5 mm lead and 4 mm scintillator.. As in the central calorimeter, a shower maximum detector (SMD) is embedded in the towers and the first layer of the calorimeter

is used as pre-shower detector. The SMD measures the position of electromagnetic shower within 1 mm accuracy. The resolution of electromagnetic part of the plug calorimeter is  $16 \% / \sqrt{E_T/GeV} \oplus 1 \%$ .

The hadronic section of the plug calorimeter is a 23 layer sampling device, with unit layers made of 2 inch iron and 6 mm scintillator. The energy resolution attainable in plug hadronic calorimeter is  $80 \% / \sqrt{E_T/GeV} \oplus 5 \%$ .

## 2.5 Muon Chambers

The outermost subsystem of the detector include still absorbers, scintillators, and stacks of drift tubes, used for the identification of muons.

Due to their minimum ionizing behavior, muons can easily pass through the large amount of material. At the same time, the majority of other particles produced in proton-antiproton collisions get absorbed by the calorimeter material. Additional layers of steel absorbers are placed immediately after the calorimeter to purify the muon detection. Outside of the steel, the penetrating muons are detected in a stack of muon drift tubes. The extended geometrical coverage of the central muon systems is shown as  $\eta - \phi$  map on Figure 2.11.

Muon tubes are filled with Ar-Ethane gas mixture. When a muon traverses the tube it ionizes the gas along its trajectory. Following the electrostatic field inside the tube ions drifts to the wire located at the center. Since the drift speed is known it is possible to reconstruct the distance between the passing muon and the wire, based on the measured timing. To facilitate full geometrical reconstruction of muon trajectory, the drift tubes are stacked together in several layers.

The scintillator counters outside the muon tube stacks provide additional confirmation of muon presence by generating a light impulse, collected by the photo-multiplier tubes. This signal is fast and therefore can be used to anchor the timing measurements obtained from the muon drift tubes.

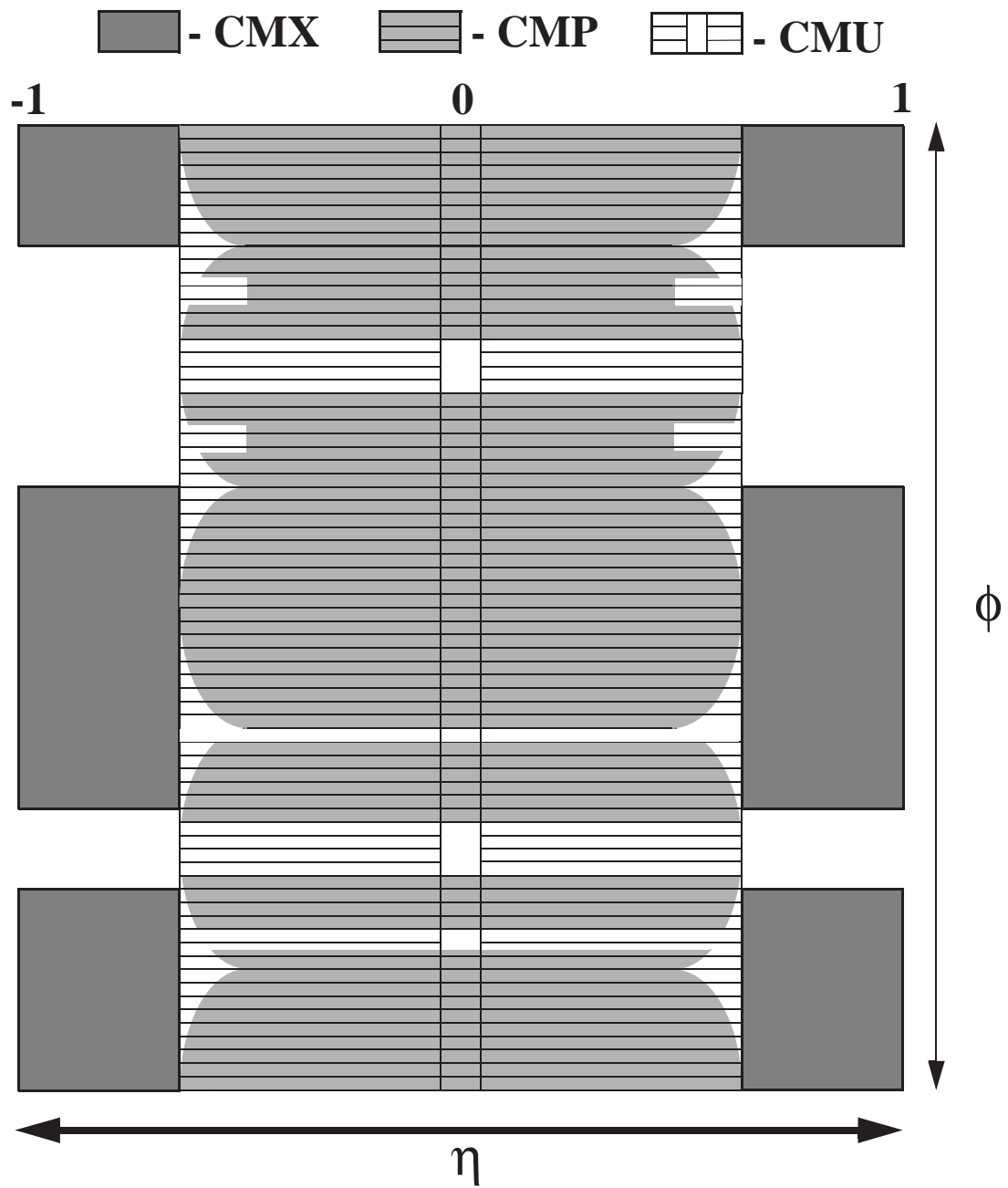


**Figure 2.11.**  $\eta$  and  $\phi$  coverage of the CDF II muon system.



### 2.5.1 Central Muon Chambers

The Central Muon Detector (CMU) is the original muon system built at CDF, which consists of 144 modules with 16 rectangular cells per module, as shown on Figure 2.12. The detector is placed just outside the central calorimeter, whose bulk absorbs more than 99 % of the outgoing particles. The cells are stacked in four layers in radial direction with a small azimuthal offset in order to facilitate the muon trajectory reconstruction. Each wire is connected to TDC board for timing information readout, which is used for measuring muon location in  $r - \phi$  plane. In addition, the amplitude-digit converter (ADC) is attached to each wire's end, to measure the collected charge, which is used to define the muon's location in  $\hat{z}$  via charge division.

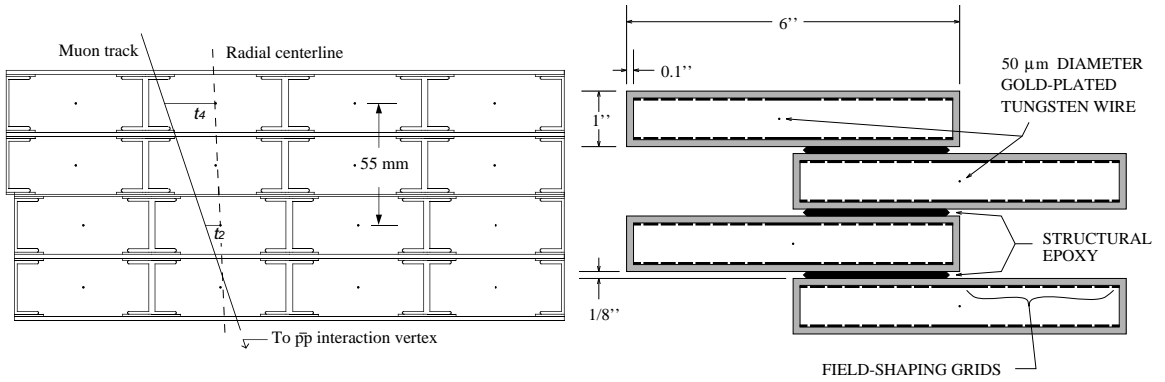


**Figure 2.12.** Transverse view of a CMU module. **Figure 2.13.** Transverse view of a CMP stack.

A second set of muon chambers—Central Muon Upgrade (CMP) is placed behind an additional 60 cm layer of steel, which is provided by the solenoid return yoke. This detector forms a square box around the CMU and the pseudo-rapidity coverage therefore varies with azimuth as shown in Figure 2.11. The CMP consists of four layers of rectangular single-wire drift tubes, staggered by half cell per layer as shown in Figure 2.13. The chambers are in proportional mode with a maximum drift time of  $1.4 \mu\text{s}$ . Preamplifiers are mounted on the end of the stacks and signals are read out by a single TDC per wire. The outer surface of the CMP is covered by the Central Scintillator Upgrade (CSP)—a layer of rectangular scintillator tiles.

The Central Muon Extension (CMX) is an addition to the central muon detectors that consists of conical sections of drift tubes which covers the pseudo-rapidity range from 0.65 to 1.0. Though no additional layer of steel is added, the large angle through the calorimeter and solenoid makes up enough absorbent material along the muon path. Each section of CMX has 15 degrees of azimuthal coverage and consists of 12 drift tubes stacked in four layers with half-cell offset. Both outer surfaces of CMX are covered by the Central Scintillator Extension (CSX)—a layer of trapezoidal scintillator tiles.

### 2.5.2 Intermediate Muon Detector

The muon identification beyond the central region is made possible by the Intermediate Muon Detector (IMU) which extends to the pseudo-rapidity coverage of  $|\eta|=2$ . This detector is based on its predecessor—Run I forward muon toroidal magnets that in Run II are moved closer to the interaction point. The still toroids are not energized and are used simply as shielding to purify the muon detection, since the magnetic field from solenoid and the new central tracker are able to provide the accurate muon trajectory measurements in the forward region. Similar to the central muon detectors, the IMU has four staggered layers of muon drift tubes and two layers of scintillators.

## 2.6 Data Acquisition System

Due to the increase in collision frequency, the DAQ and trigger systems of CDF had to be almost completely replaced. The new three-level pipelined architecture, illustrated in Figure 2.14, is fully capable of withstanding a 132 ns bunch separation, while keeping the deadtime as short as possible.

The hardware for each trigger level is configured through the *trigger database*, which is a set of interconnected tables implemented in the Oracle relational database. A complete configuration of the trigger system in terms of parameter and cut values

of various subsystems can be retrieved from the table if one provides a unique key called *physics table*.

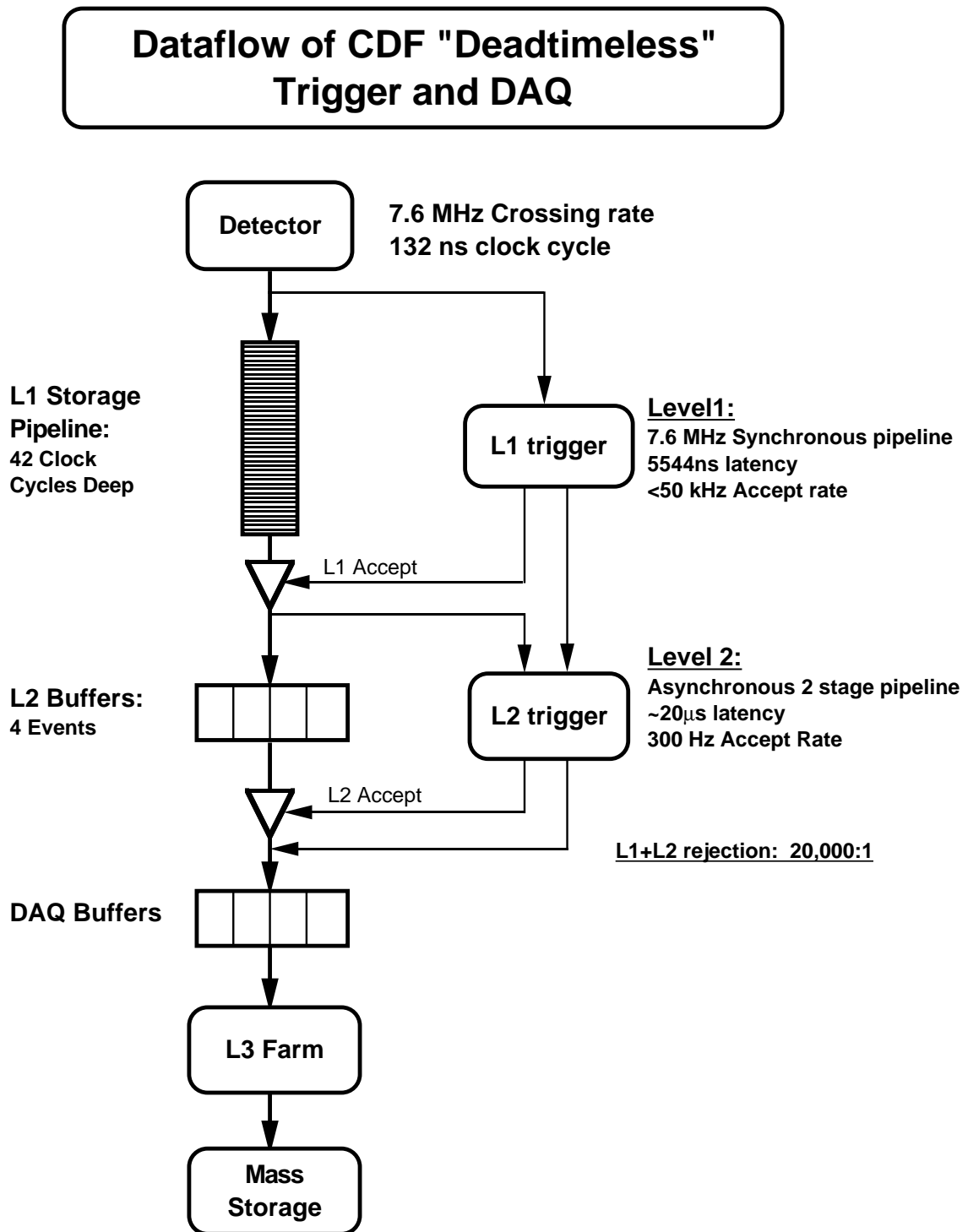


Figure 2.14. Schematic view of DAQ and trigger systems.

### 2.6.1 Level 1 Trigger

The front-end electronics of all detectors is fitted with a synchronous pipeline, 42 events deep, where the entire data regarding each event is stored for 5544 *ns*. Meanwhile, part of the data is examined in a first layer of dedicated, synchronous, highly parallel hardware processors:

- the eXtremely Fast Tracker (XFT) reconstructs tracks in the transverse plane of the COT and extrapolation unit (XTRP) matches these tracks to the level one calorimeter and muon trigger primitives;
- the Calorimeter trigger boards (DIRAC) reconstruct electromagnetic and hadron trigger towers and also calculates the total and missing transverse energy of the event;
- the Muon trigger cards match extrapolated tracks to the trigger primitives in muon chambers.

A total of 64 various outputs from level one subsystems get multiplexed by 8 logical units in the Global Level 1 Trigger board (FRED) according to the configuration content retrieved from the trigger database. Up to 64 various level one outputs can be produced and fed into level two Alpha processors.

The level one trigger produces a decision within 4000 *ns*, while the data is still in the pipeline, which makes it truly deadtimeless system.

### 2.6.2 Level 2 Trigger

Events passing level one trigger are downloaded into one of four asynchronous event buffers, and further analyzed by the level two set of hardware processors. Level 2 trigger is asynchronous: events remain in the buffer until they are accepted or rejected. In cases where all four buffers are full, the system encounters the dead time. There are two phases at level two: readout of level two systems and decision making. Each phase last about 10  $\mu s$ .

The following triggers systems are read out:

- The calorimeter boards (DCAS), which runs the clustering algorithm for electromagnetic and hadron online shower reconstruction;
- The calorimeter shower maximum (XCES) is used to identify electrons and photons in order to reduce the fake rate coming from the hadron jets;
- The Silicon Vertex Tracker (SVT), which reconstructs tracks in silicon detectors and measures their impact parameter;
- Level 1 muon and track data is also collected.

During the decision making stage the read out data are fed to a pair of Alpha processors, where each processor examines the event for a different set of level 2 trigger specifications, downloaded from the trigger data base described in the Section 2.6.

### **2.6.3 Level 3 Trigger**

Events accepted by Alpha processors from level two trigger read out entirely from the front-end electronics and are loaded into a Linux PC farm, where they are completely reconstructed by the CDF offline software. The software is almost fully written in C++ programming language, using object-oriented methods.

## CHAPTER 3

### Data Sets

This analysis is based on the data collected by CDF during a year and half data-taking period which was started at the beginning of Run II. In this chapter we describe the *inclusive high- $P_T$  muon data set* and various simulation samples that were used in this analysis.

#### 3.1 Inclusive Muon Samples

The high- $P_T$  muon data set used in these measurements was collected between March 23, 2002 and September 6, 2003 and has a corresponding run range of *141544* to *168889*. The Data Quality Monitoring working group established a common list of good runs [24] for leptons that is used to select events from this run range. The integrated luminosity for this run range is determined to be  $193.5 \pm 11.6 \text{ pb}^{-1}$ .

This data has been collected through the high- $P_T$  CMUP and CMX muon trigger paths, as described in Section 3.2, into the original data sample *bhmu08*, which is processed with the version 4.8.4 of the reconstruction code. To reduce the size of the data set it is stripped further into the intermediate multipurpose sample *bt0p1g*, which contains the sub-sample of events with a reconstructed muon that passes a loose set of muon identification cuts [25]. This data sample is refined further through a substantial amount of re-processing using version 4.11.2 of the offline reconstruction code [26]. The finalized sample is then registered under *rtop01* data set name and put on tape through the CDF data file catalog system [27].

## 3.2 High- $P_T$ Muon Trigger Paths

The muon data set described in the previous section is written through the **Stream B** data channel, which is fed by high- $P_T$  lepton trigger paths. Currently, there are two basic trigger paths for inclusive high- $P_T$  muons: MUON\_CMUP18 and MUON\_CMX18.

The MUON\_CMX18 data collected prior to run number *150145* is not used in physics analysis due to the large noise in the CMX chambers. The combination of both trigger paths in our measurement may produce additional sources of uncertainties. Also if we base our measurement solely on data gathered from MUON\_CMUP18 trigger path many parameters will cancel out completely, thus improving the overall result.

The MUON\_CMUP18 trigger path is divided into three levels:

- **L1\_CMUP6\_PT4**: The muon trigger cards attempt to match XFT track with both CMU and CMP hits. XFT provides tracks with  $P_T \geq 4$  GeV/c and at least 10 hits per axial super layer. Starting from run *152612* the minimum number of hits per super layer becomes 11.
- **L2\_TRK\_L1\_CMUP6\_PT4**: Prior to run *152612* all events fed by Level 1 trigger were auto-accepted and sent further to Level 3. Starting from run *152612* events coming from Level 1 were required to have a XFT track with  $P_T \geq 8$  GeV/c in order to pass Level 2 trigger requirements.
- **L3\_MUON\_CMUP18**: The trigger code attempts to reconstruct the muon COT track and links it to the CMU and CMP track segments or stubs. The required  $P_T$  of the COT track must be greater than 18 GeV/c. The code also checks matching between projected muon trajectory and stubs in the plane transverse to the beam-line. The track must match stub within 10 cm for CMU and 30 cm for CMP chambers.

Every event in our sample must have at least one muon that triggered the event according to these requirements. Additional offline selections are described in more details in the next Chapter 4.

### 3.3 Simulation Samples

We use the simulation samples in this analysis in order to determine both the acceptance discussed in Chapter 9 and the fraction of background events for  $W$  and  $Z$  processes described in more details in Chapters 6 and 8. These samples were generated using the standard Monte-Carlo technique [28].

The processes  $p\bar{p} \rightarrow W \rightarrow \mu\nu$  and  $p\bar{p} \rightarrow Z \rightarrow \mu\mu$  were simulated by PYTHIA [29] Monte Carlo generator with the CTEQ5L [30] parton distribution functions. The transverse motion of the vector boson and underlying event activity is tuned to match the data [20]. For each event the generator creates a list of final state particles that are fully specified kinematically.

The full CDF simulation is used to model the detector response. In case when final state particle is a muon, the CDF simulation propagates the particle through the Central Outer Tracker (COT) volume in the solenoidal magnetic field out to the calorimeters. The muon trajectory is simulated as a circular path in the transverse plane with the actual tracker resolution described previously in Section 2.3.2. Outside the magnetic field the muons follow a straight line trajectory through the calorimeter to the Central Muon chambers (CMU) and continue further through the additional layers of steel out to the Central Muon Upgrade chambers (CMP). The detector simulation takes into account multiple scattering and energy loss effects for muon momentum, while propagating the particle through the detector interior.

The generated data sets `wewk0m`, `wewk0t`, `zewk0m`, `zewk0t` correspond to the processes  $W \rightarrow \mu\nu$ ,  $W \rightarrow \tau\nu$ ,  $Z \rightarrow \mu\mu$ ,  $Z \rightarrow \tau\tau$  respectively.



## CHAPTER 4

### Muon Identification

When muons emerge from the interaction point they penetrate through various detector systems. The three major detectors that help to identify muon are: central tracker, calorimeter and muon chambers. The central tracker and muon chambers can detect muon since it is a charged particle and, therefore, it leaves the ionized trace behind when it passes through the gas volume. In COT the ionization is collected by the potential wires as described in Section 2.3.2. Then the signal from each channel is read out and since the position of each wire is known precisely, the collection of hits can be reconstructed for the associated charged particle. The reconstruction algorithm links hits together into the segments, which get linked further into a track coinciding with the trajectory of the actual particle. Magnetic field inside the COT bends muon trajectory into a *helix*, which can be fitted with 5 parameters as

$$\begin{aligned}x(s) &= \rho \sin(2cs + \phi_0) - (\rho + d_0)\sin(\phi_0) \\y(s) &= \rho \cos(2cs + \phi_0) - (\rho + d_0)\cos(\phi_0) \\z(s) &= z_0 + s\lambda ,\end{aligned}\tag{4.1}$$

where  $s$  is projected length along the track,  $\rho = \frac{1}{2c}$  is the helix radius. The signed semicurvature  $c$  is related to the transverse momentum  $P_T$  and charge  $q$  of a particle  $c = \frac{qeB}{2P_T}$ , where  $B$  is the magnetic field inside the COT volume. For high- $P_T$  particles the *impact* parameter  $d_0$  is defined as the distance from the COT origin to the track in  $\hat{x}$ - $\hat{y}$  plane and  $\phi_0$  is the azimuthal angle of the track. The parameter  $\lambda$  is related to the angle  $\theta$  between the track and  $\hat{z}$  axis as  $\lambda = \cot(\theta)$ .

Within the analysis framework a muon is defined as a reconstructed object that consists of a track linked to the respective muon chamber track segments or *stubs*. Very often muons also traverse the calorimeter detector towers depositing typical minimum ionizing energy, leaving neighboring calorimeter towers unaffected as shown in Figures 4.1–4.2.

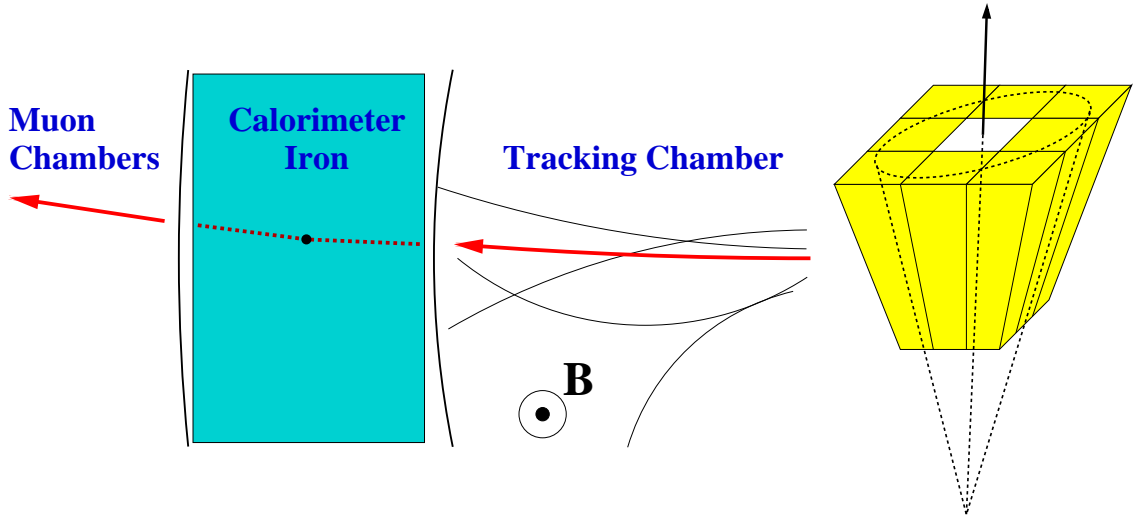


**Figure 4.1.** Schematic view of the detector systems involved in muon reconstruction.

**Figure 4.2.** Illustration of muon isolation variable definition.

Most of the particles emerging from the interaction point are not muons. In order to shield them from penetrating into the CMU detector, the muon chambers are placed outside the calorimeter iron. The additional layers of iron are placed outside the CMU chambers to enhance the shielding of CMP detector.

We establish the matching between the reconstructed muon stub and its track by measuring the distance in  $\hat{x}$ – $\hat{y}$  plane between the stub position and the location of the track extrapolated out to the muon chamber. When a muon passes through the bulk of iron it slightly changes its trajectory direction due to the *multiple scattering* phenomenon, which is Coulomb scattering between a muon and the nucleus of iron. As a result of this effect, the matching distance between the muon stub and its track increases. Since the amount of iron shielding is less for the CMU detector, the matching distance for the CMU chamber is shorter than that of the CMP chamber.

## 4.1 Inclusive Muon Selections

For our event selection it is extremely important to reject backgrounds and retain high- $P_T$  muons with very high efficiency. This can be achieved by cutting on numerous variables associated with the reconstructed particle. The collection of track, stub, and calorimeter tower parameters provides us with many variables that can be used for muon selection. We insure the quality of muon object by enforcing the following requirements:

- the muon is represented by the high quality track
- the matching between muon track and muon chamber segments is good
- the energy for calorimeter towers near muon track is consistent with minimum ionizing deposition

Several requirements are introduced to select a good muon track. We only consider the tracks that will pass through at least eight COT super-layers, which means that muon exits the tracker end-plate at the radius  $\rho$  greater than 140 *cm*. Then, we ensure that track originates within the luminous beam region, which can be represented in terms of track helix parameters as:

$$| z_0 | < 60 \text{ cm} \text{ — along the beam-line, and}$$

$$| d_0^{cor} = d_0 + x_{beam} \cdot \sin(\phi) - y_{beam} \cdot \cos(\phi) | < 0.2 \text{ cm} \text{ — in the transverse plane.}$$

The corrected value of the impact parameter reflects the shift of COT origin to the actual location of the beam, which is positioned at  $(x_{beam}, y_{beam})$  point away from the origin. If silicon hits are present on the reconstructed track we require  $| d_0^{cor} | < 0.02 \text{ cm}$ . We also demand that track contains at least 3 good axial and 3 good stereo segments, where each good segment in turn has at least seven COT associated hits. The quality of track helix fit is ensured by requiring  $| \chi_{COT}^2 / ndf | < 2$ . Here the value of  $\chi^2$  function defines the quality of the track helix fitting and the number of degree of freedom for this fit expresses the number of associated COT hits on track  $ndf = N_{COT}^{hits} - 5$ , where 5 reflects the number of helix parameters.

In this analysis the geometrical coverage of muon chambers is referred to as the muon *fiducial* regions. Part of our selection rules is a requirement that a muon track must always point to the muon fiducial region. The reconstructed stubs in the CMU and CMP chambers linked to the muon track are subject to the matching distance cuts  $|\Delta X|_{CMU} < 3 \text{ cm}$  for CMU chamber and  $|\Delta X|_{CMP} < 5 \text{ cm}$  for CMP chamber, which reflects the presence of multiple scattering in the iron shielding discussed in previous section.

The calorimeter response is divided into two parts: the energy from electromagnetic compartment and the energy from hadronic compartment. To take into account muon momentum dependence [31], the following criteria is used to insure minimum ionizing energy deposition in calorimeter towers:

$$E_{EM} < \max\{2, 2 + 0.0115(E_\mu - 100)\} \text{ and } E_{HAD} < \max\{6, 6 + 0.0280(E_\mu - 100)\},$$

where calorimeter  $E_{EM}$ ,  $E_{HAD}$  and muon  $E_\mu$  energies are measured in GeV. In this case muon energy  $E_\mu$  is equal to the absolute value of muon momentum  $|\vec{P}_\mu|$ .

The muon *isolation energy* variable is defined as ratio of the transverse energy  $E_T$  measured in the calorimeter towers inside a  $\Delta R = \sqrt{(\Delta\eta)^2 + (\Delta\phi)^2} = 0.4$  cone centered on the muon track excluding the muon tower as shown in Figure 4.2. In order to obtain isolation ratio we divide isolation energy by the muon  $P_T$ :

$$Iso = \left[ \left( \sum_{\Delta R < 0.4} E_T^i \right) - E_T^\mu \right] / P_T^\mu .$$

Leptons from vector boson prompt decays are isolated, so we require  $Iso < 0.1$  for muons in our sample to reduce the contamination from hadron semileptonic decays.

Events collected in our data sample must have at least one high- $P_T$  muon with  $P_T \geq 18 \text{ GeV}/c$  due to the trigger selections discussed in Chapter 3. For our analysis we slightly raise the value of the muon transverse momentum cut to make it  $P_T \geq 20 \text{ GeV}/c$  to get rid of the hardware and software trigger resolution effects.

The cosmic ray veto method is described in details the next Section 4.2.

The complete set of selections for inclusive high- $P_T$  muon is shown in Table 4.1.

Requirement	Purpose	Number of Passed Events
Good Run	Quality Data	1,128,370
Fiducial Muons	Muon Chamber Active Regions	727,865
Trigger Bits	Enforce Online Trigger	674,699
CMU and CMP Stubs	Use Central Muon Detectors	669,131
Cosmic Veto	Remove Cosmic Rays	491,023
$ z_0  < 60 \text{ cm}$	Nominal Collision Region	421,166
COT Radius $\rho \geq 140 \text{ cm}$	Fiducial Tracks	421,165
$P_T \geq 20 \text{ GeV}/c$	Low- $P_T$ Noise Reduction	246,681
$ \Delta X _{CMU} < 3 \text{ cm}$	Good Stub-Track Match	190,729
$ \Delta X _{CMP} < 5 \text{ cm}$	Good Stub-Track Match	153,598
$E_{EM} < 2 \text{ GeV}$	Minimum Ionizing Deposition	143,313
$E_{HAD} < 6 \text{ GeV}$	Minimum Ionizing Deposition	138,007
$N_{Seg}^{Ax} \geq 3, N_{Seg}^{St} \geq 3$	Good Track Quality	120,956
$ d_0^{cor}  < 0.2 \text{ cm}$	Good Track Quality	111,064
$\chi_{COT}^2/ndf < 2$	Good Track Quality	109,784
$Iso < 0.1$	Background Reduction	77,140

**Table 4.1.** Inclusive high- $P_T$  muon selection cuts.

## 4.2 Cosmic Ray Contamination

Energetic cosmic ray muons traverse the detector at a significant rate, leaving hits in both muon and COT chambers and passing the high- $P_T$  muon trigger requirements. Thus the original muon data set is heavily contaminated with the cosmic ray events.

A cosmic muon, passing through the detector, represents itself as a combination of incoming and outgoing legs relative to the beam line of the detector. To be recorded in the data, at least one such leg should form a good COT track with muon stubs linked to it. Often the other leg also gets reconstructed as a track or muon. The majority of events triggered by cosmic muons have much lower tracking multiplicity in comparison with the collision events. On the other hand, the fraction of events in which the cosmic muon hits the detector during the collision is quite significant.

Muons from cosmic rays are generally very isolated and easily pass the muon

identification cuts listed in Table 4.1. When only one cosmic leg is reconstructed, the event can imitate the  $W$  signature. Quite often both cosmic legs are present and in this case the event fakes  $Z$  decay. Therefore, an effective cosmic ray tagging technique is required to reduce cosmic background in both parts of our data sample.

The cosmic ray tagging algorithm [32] utilizes the timing information of the COT hits. The core of this method is a multi-parameter fit over the set of hits left by the incoming and outgoing cosmic legs. The leg belonging to the reconstructed muon serves as the seed track for the fit. The other leg is referred to as the opposite track. The algorithm performs in the following steps:

- hits belonging to the seed track are refitted with the 5 helix parameters and the global time shift
- based on the best value of the fit, incoming or outgoing hypothesis is assigned to the seed track
- the refitted seed track is used to find the other cosmic leg by defining a “road” in which hits are searched for.
- if enough hits are found, a similar fit is performed to produce the opposite track
- for the seed and the opposite tracks a simultaneous fit is performed to combine all hits into a single helix

The final decision of the cosmic tagger depends on the assigned direction of the legs. If one leg is recognized as incoming and the other as outgoing, then the event is tagged as cosmic ray. For a pair of tracks coming out of a real beam collision, both legs should be categorized as outgoing.

Further details on the cosmic ray backgrounds and tagger efficiency will be described in Chapters 6, 8, and 10 of this thesis.

## CHAPTER 5

### W Selection Criteria

When a  $W$  boson decays into a muon and a neutrino, the final state particles acquire high momentum due to a large  $W$  mass.

A kinematic cut  $P_T \geq 20$  GeV/ $c$  is applied to the muon from  $W$  decay along with the other cuts that coincide with the inclusive selections described previously in more details in Chapter 4. The comparison of the muon transverse momentum spectrum between data and simulation for events passing  $W$  selection requirements is shown on Figure 5.1.

All muon momentum components can be reconstructed by COT, but there is no direct way to measure neutrino momentum components. We can, however, infer the transverse momentum of neutrino by measuring the *missing transverse energy* of the event. The  $\hat{z}$ -component of the neutrino momentum cannot be reconstructed, since for proton-antiproton collision the longitudinal momentum of interacting parton pair is unknown. Therefore, event kinematics can only be reconstructed in the transverse plane with respect to the beam-line direction.

To reconstruct the missing transverse energy of the event we first define the event's "total energy vector"  $\vec{E}_T = (E_x, E_y)$  in the transverse plane

$$E_x = \sum_i (HAD_T^i + EM_T^i) \cos \phi_i \quad E_y = \sum_i (HAD_T^i + EM_T^i) \sin \phi_i, \quad (5.1)$$

where  $HAD_T^i$ —the amount of energy deposited in the hadronic calorimeter tower  $i$  projected on transverse plane,  $EM_T^i$ —the amount of energy deposited in the electromagnetic calorimeter tower projected on transverse plane,  $\phi_i$ —the polar angle of the

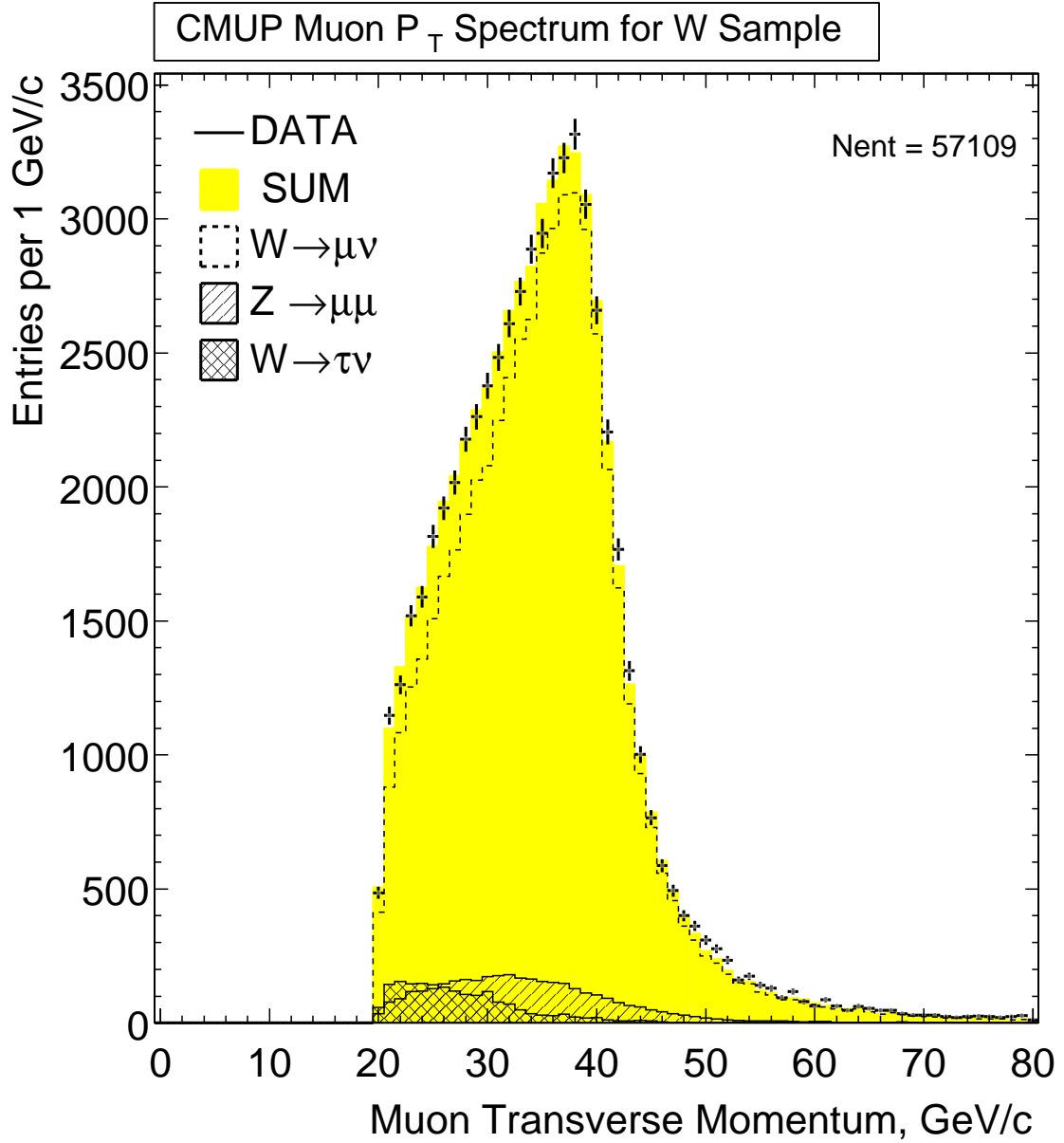


**Figure 5.1.** Muon transverse momentum spectrum in data and simulation for  $W \rightarrow \mu\nu$  candidate events. Only the leading contributing processes are shown.



calorimeter tower, and the sum is taken over all detector towers.

The colliding parton pair has zero initial momentum in the transverse plane, so using the conservation of momentum we define the missing transverse energy vector as

$$\vec{E}_T + \vec{\cancel{E}}_T = 0, \quad \vec{\cancel{E}}_T = -\vec{E}_T \quad (5.2)$$

and we ascribe the absolute value of  $\cancel{E}_T$  to the transverse momentum of the neutrino for events where one neutrino is expected.

When a muon is present in the event it deposits only minimum ionizing energy in the calorimeter. Therefore, for high- $P_T$  muons the actual momentum in the event is much greater than the energy they deposit in the calorimeter towers. To make a correction for this case we exclude muon energy deposition and add its momentum contribution in the Equations 5.1

$$E_x = \sum_i (HAD_T^i + EM_T^i) \cos \phi_i - (HAD_T^\mu + EM_T^\mu) \cos \phi_\mu + P_T^\mu \cos \phi_\mu \quad (5.3)$$

$$E_y = \sum_i (HAD_T^i + EM_T^i) \sin \phi_i - (HAD_T^\mu + EM_T^\mu) \sin \phi_\mu + P_T^\mu \sin \phi_\mu \quad (5.4)$$

where  $HAD_T^\mu$ —minimum ionizing energy deposited in the hadronic calorimeter tower traversed by muon projected on transverse plane,  $EM_T^\mu$ —minimum ionizing energy deposited in the electromagnetic calorimeter tower traversed by muon projected on transverse plane,  $\phi_\mu$ —the polar angle of the muon,  $P_T^\mu$ —muon transverse momentum.

Figure 6.5 shows the  $\cancel{E}_T$  spectrum of simulated electroweak processes along with our model of the QCD background. The electroweak processes and the QCD background are relatively well separated. Therefore, to reject most of the non-electroweak background and retain the signal efficiently we chose a kinematic cut  $\cancel{E}_T \geq 20$  GeV.

As will be shown in Chapter 6 the contamination from  $Z$  events is the leading source of background. To reduce  $Z \rightarrow \mu\mu$  presence in  $W$  candidate events a special  $Z$  rejection criteria is applied. The events are rejected only if the second muon passes a loose set of minimum ionizing energy deposition cuts  $EM < 3$  GeV and

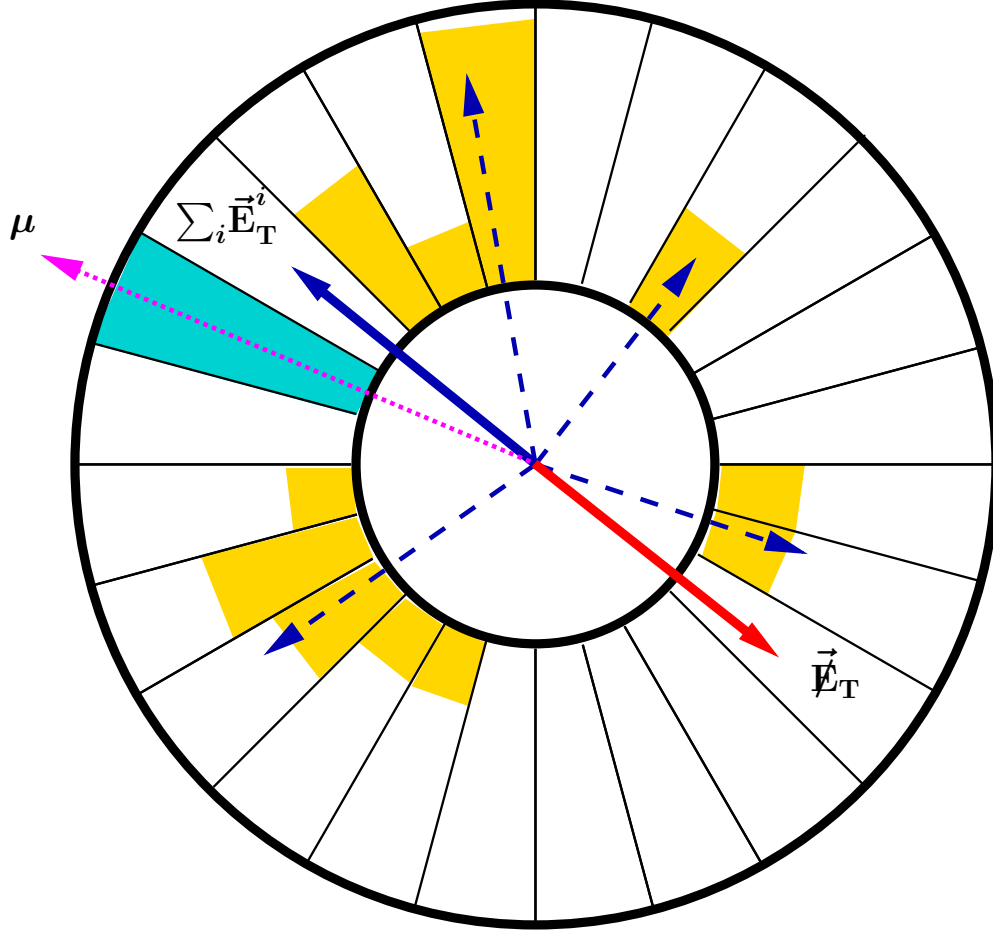


**Figure 5.2.** A schematic view illustrating the calculation of the transverse missing energy  $\cancel{E}_T$ . The energies of each tower are projected on  $\hat{x}$  and  $\hat{y}$  directions and summed across the entire calorimeter to form a “total energy vector”  $\sum_i \vec{E}_T^i = (\sum_i E_x^i, \sum_i E_y^i)$ . To correct for the muon presence in the event, the tower crossed by muon with minimum energy deposition is subtracted from  $\sum_i \vec{E}_T^i$  and replaced by the muon momentum. The inverted vector of the corrected total energy is defined as the transverse missing energy  $\cancel{E}_T$ .

$HAD < 9$  GeV. This criteria guarantees that there is no more than one high- $P_T$  muon-like object in the event, which also simplifies the  $\cancel{E}_T$  calculation.

Table 5.1 summarizes the  $W$  selection cuts and lists the number of passed events at every stage of the selection. The detailed description of the inclusive muon selection is listed previously in Section 4.

Requirement	Purpose	Number of Passed Events
Inclusive Muon	High- $P_T$ Quality Muon	77,140
$Z$ Veto	Remove $Z$ Events	70,512
$\cancel{E}_T > 20$ GeV	Background Reduction	57,109

**Table 5.1.**  $W \rightarrow \mu\nu$  selection cuts.

Since the neutrino momentum is not fully reconstructible we cannot measure the dilepton invariant mass to constrain further the kinematics of the  $W$  candidate events. However, we can build dilepton *transverse mass*—a two dimensional analog of the invariant mass, constrained to the transverse plane:

$$M_T = \sqrt{(P_T^\mu + \cancel{E}_T)^2 - (\vec{P}_T^\mu + \vec{\cancel{E}}_T)^2}, \quad (5.5)$$

where  $P_T^\mu = |\vec{P}_T^\mu|$ —absolute value of muon transverse momentum, and  $\cancel{E}_T = |\vec{\cancel{E}}_T|$ —absolute value of missing transverse energy in the event.

The reconstructed transverse mass spectrum for  $W$  candidates is shown on Figure 5.3 both for data and simulation events. The distribution have the characteristic shape of the *Jacobian peak*, which has its maximum near the actual mass of  $W$  boson and rapidly falls off for the values above the  $W$  mass. At the values below the  $W$  mass the spectrum falls slowly until it drops at  $40 \text{ GeV}/c^2$ —the kinematic limit imposed by our  $W$  selection cuts  $P_T \geq 20 \text{ GeV}/c$  and  $\cancel{E}_T \geq 20 \text{ GeV}$ .

The yield of  $W$  candidate events for the data-taking runs is shown on Figure 5.4. The run interval is sampled in the ranges with the corresponding integrated luminosity of at least  $8 \text{ pb}^{-1}$ . Figure 5.5 shows  $W$  event count per inverse picobarn of delivered

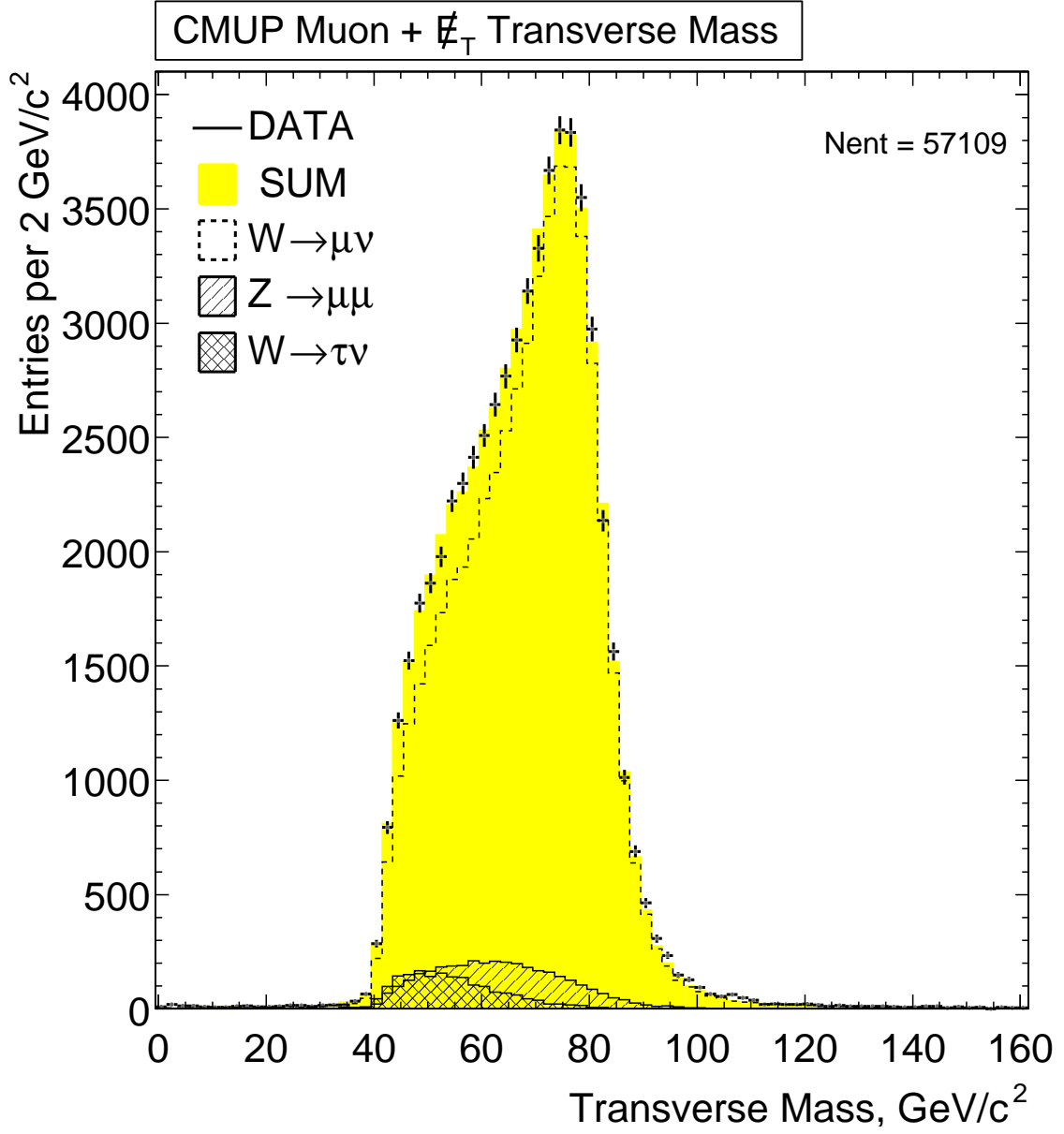


**Figure 5.3.** The transverse mass spectrum in data and simulation for  $W \rightarrow \mu\nu$  events.

luminosity for various run ranges, which is a relatively flat distribution. Higher event count for the first four run ranges reflects the changes in muon trigger as previously described in Section 3.2.

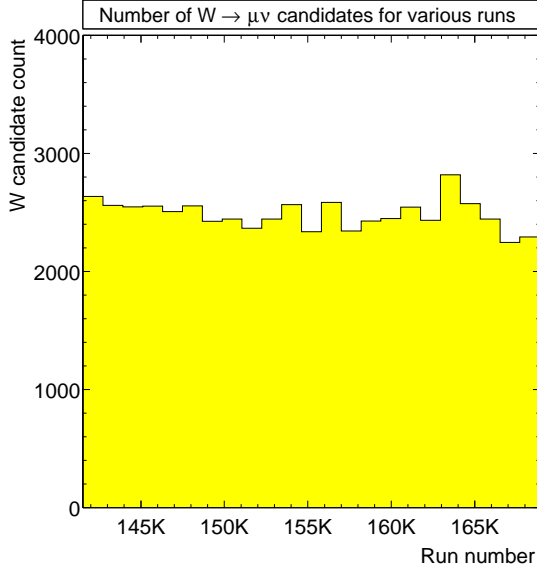


**Figure 5.4.** Number of  $W$  candidate events per a run range.

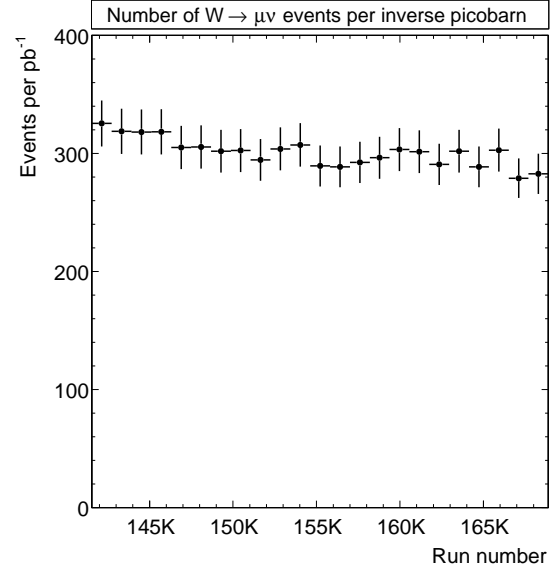


**Figure 5.5.**  $W$  candidate yield per inverse picobarn of delivered luminosity.

## CHAPTER 6

### *W* Backgrounds

In this chapter we estimate the contribution of four main backgrounds to our  $W \rightarrow \mu\nu$  candidate event sample. The backgrounds to be estimated are  $Z \rightarrow \mu^+\mu^-$ ,  $W \rightarrow \tau\nu$ , QCD processes and cosmic rays. The sum of all these contributing background processes, described in detail in the subsections below, yields a total fraction of background events in the  $W$  sample of

$$b_W = 9.49 \pm 0.45 \text{ \%}. \quad (6.1)$$

#### 6.1 Electroweak Processes

As it was already mentioned in Chapter 5 that  $Z \rightarrow \mu\mu$  process can contribute to the sample of  $W$  candidates. In cases when a hard photon is radiated along the second muon or when the second track is not found the  $Z$  veto fails to filter out  $Z \rightarrow \mu\mu$  decays.

$W \rightarrow \tau\nu$  can contribute to the sample of  $W$  candidates when, for example, decay  $\tau \rightarrow \mu\nu\bar{\nu}$  happens. In case when muon from tau decay has  $P_T \geq 20 \text{ GeV}/c$ , the event will appear in our  $W$  sample, given that  $\cancel{E}_T \geq 20 \text{ GeV}$ .

The size of these background processes is calculated using electroweak Monte Carlo samples. While it is possible to calculate them in a stand alone way, our standard background technique is best suited to a procedure where the electroweak processes treated simultaneously with the QCD background, which will be described in detail

in the next subsection. The fraction of these background events will be found to be:

$$b_{Z \rightarrow \mu\mu}^W = 5.85 \pm 0.11 \% \quad \text{and} \quad b_{W \rightarrow \tau\nu}^W = 3.10 \pm 0.12 \%. \quad (6.2)$$

## 6.2 QCD Backgrounds

We will show in the next subsection that contribution from the cosmic rays is negligible, therefore we attribute the remainder of the background to the QCD processes.

Contrary to electroweak processes, the majority of QCD background events have relatively small missing transverse energy and large isolation ratio. For that reason we choose to look at the  $\cancel{E}_T$  versus isolation ratio distributions to determine the number of the background events. Figures 6.1, 6.2 show these distributions for  $W$  candidates and  $W \rightarrow \mu\nu$  simulation respectively, where the analysis cuts define four regions:

$$\begin{aligned} \mathbf{B} : \cancel{E}_T < 20 \text{ GeV}, \text{ Iso} \geq 0.1 & \quad \mathbf{C} : \cancel{E}_T \geq 20 \text{ GeV}, \text{ Iso} \geq 0.1 \\ \mathbf{A} : \cancel{E}_T < 20 \text{ GeV}, \text{ Iso} < 0.1 & \quad \mathbf{D} : \cancel{E}_T \geq 20 \text{ GeV}, \text{ Iso} < 0.1 \end{aligned}$$

We will extract the QCD background in the signal region D by fitting data distribution on figure 6.1 with the simulation shapes for electroweak processes and with the QCD shape obtained from the data distribution itself. Table 6.1 summarizes the event distributions for regions A, B, C, and D for  $W$  candidates and simulated electroweak processes.

Process Type	Generated	Number of Events			
	G	A	B	C	D
$W \rightarrow \mu\nu$	2,026,500	12,310	426	6,686	182,831
$Z \rightarrow \mu\mu$	472,500	5,372	192	1,143	29,428
$W \rightarrow \tau\nu$	490,000	478	12	50	1,512
$W$ candidates	—	13,403	28,647	2,940	57,109
QCD	—	8,750	28,491	860	264

**Table 6.1.** Event distribution for regions A, B, C, and D for various processes.

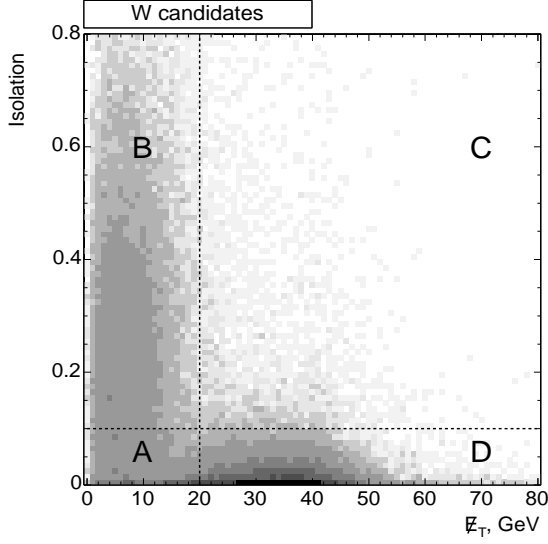


**Figure 6.1.** Isolation vs.  $E_T$  distribution for  $W$  candidate events.

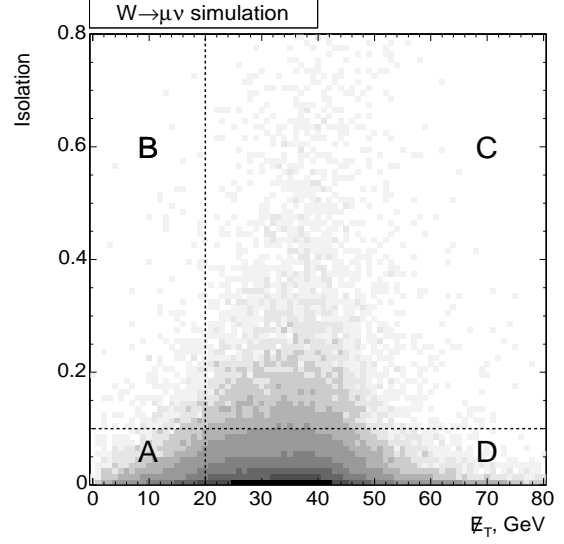


**Figure 6.2.** Isolation vs.  $E_T$  distribution for  $W \rightarrow \mu\nu$  simulation.

In order to obtain the number of QCD events, we assume that for QCD background, the  $E_T$  distribution does not depend on isolation ratio. In this case the number of QCD events  $A_{QCD}$ ,  $B_{QCD}$ ,  $C_{QCD}$ ,  $D_{QCD}$  in the regions A, B, C, D can be expressed as:

$$\frac{A_{QCD}}{B_{QCD}} = \frac{D_{QCD}}{C_{QCD}} \quad \text{or} \quad \frac{A - A_{EWK}}{B - B_{EWK}} = \frac{D - D_{EWK}}{C - C_{EWK}}, \quad (6.3)$$

where  $A$ ,  $B$ ,  $C$ ,  $D$ —the number of  $W$  candidate events in the regions A, B, C, D respectively. Similarly  $A_{EWK}$ ,  $B_{EWK}$ ,  $C_{EWK}$ ,  $D_{EWK}$  is the number of  $W \rightarrow \mu\nu$ ,  $Z \rightarrow \mu\mu$ ,  $W \rightarrow \tau\nu$  events in the regions A, B, C, D respectively.

We can perform the following substitution:

$$A_{EWK} = a \cdot W, \quad B_{EWK} = b \cdot W, \quad C_{EWK} = c \cdot W, \quad D_{EWK} = d \cdot W, \quad (6.4)$$

where  $W$ —the number of expected  $W \rightarrow \mu\nu$  events in the region D, and  $a$ ,  $b$ ,  $c$ ,  $d$ —the coefficients that can be determined using the simulation sample numbers A, B, C, D, and G from Table 6.1. In order to calculate these coefficients we use the lepton universality for  $W$  decay  $g \equiv \Gamma(W \rightarrow \tau\nu)/\Gamma(W \rightarrow \ell\nu) = 1.00$  [14] and the Standard



Model prediction for the  $W$  and  $Z$  cross section ratio  $R = 10.69$  from Equation 11.12:

$$a = \frac{A_{W \rightarrow \mu\nu}/G_{W \rightarrow \mu\nu} + A_{Z \rightarrow \mu\mu}/(R \cdot G_{Z \rightarrow \mu\mu}) + g \cdot A_{W \rightarrow \tau\nu}/G_{W \rightarrow \tau\nu}}{D_{W \rightarrow \mu\nu}/G_{W \rightarrow \mu\nu}} = 0.090 , \quad (6.5)$$

$$b = \frac{B_{W \rightarrow \mu\nu}/G_{W \rightarrow \mu\nu} + B_{Z \rightarrow \mu\mu}/(R \cdot G_{Z \rightarrow \mu\mu}) + g \cdot B_{W \rightarrow \tau\nu}/G_{W \rightarrow \tau\nu}}{D_{W \rightarrow \mu\nu}/G_{W \rightarrow \mu\nu}} = 0.003 , \quad (6.6)$$

$$c = \frac{C_{W \rightarrow \mu\nu}/G_{W \rightarrow \mu\nu} + C_{Z \rightarrow \mu\mu}/(R \cdot G_{Z \rightarrow \mu\mu}) + g \cdot C_{W \rightarrow \tau\nu}/G_{W \rightarrow \tau\nu}}{D_{W \rightarrow \mu\nu}/G_{W \rightarrow \mu\nu}} = 0.040 , \quad (6.7)$$

$$d = \frac{D_{W \rightarrow \mu\nu}/G_{W \rightarrow \mu\nu} + D_{Z \rightarrow \mu\mu}/(R \cdot G_{Z \rightarrow \mu\mu}) + g \cdot D_{W \rightarrow \tau\nu}/G_{W \rightarrow \tau\nu}}{D_{W \rightarrow \mu\nu}/G_{W \rightarrow \mu\nu}} = 1.099 . \quad (6.8)$$

We use substitution 6.4 in the expression 6.3 to obtain a quadratic equation

$$(A - a \cdot W)(C - c \cdot W) = (B - b \cdot W)(D - d \cdot W) \quad (6.9)$$

that has a valid root

$$W = \frac{-\beta + \sqrt{\beta^2 + 4\alpha\gamma}}{2\alpha}, \quad (6.10)$$

where  $\alpha = (ac - bd)$ ,  $\beta = (b \cdot D + d \cdot B - a \cdot C - c \cdot A)$ ,  $\gamma = (A \cdot C - B \cdot D)$ .

The calculated numbers for various processes contributing to the signal region D are:

$$N_W = 51,734 \pm 257 \quad (6.11)$$

$$B_{Z \rightarrow \mu\mu}^W = 3,341 \pm 61 \quad B_{W \rightarrow \tau\nu}^W = 1,769 \pm 67 \quad B_{QCD}^W = 264 \pm 83 \quad (6.12)$$

where the systematic error includes both the uncertainties on parameters  $g$ ,  $R$  and the uncertainty of our assumption that in QCD events  $\cancel{E}_T$  and isolation variables are independent. In order to test this assumption we study the variation in the number of background events when isolation or  $\cancel{E}_T$  cuts are changing. When we vary the  $\cancel{E}_T$  cut we fix the regions C and D but we let the regions A and B change. Likewise, when we change the isolation ratio cut we fix the regions A and D but we let the regions B and C vary. Figures 6.3 and 6.4 shows the dependence of the calculated backgrounds on  $\cancel{E}_T$  and isolation ratio values respectively.

As listed in Tables 6.2 and 6.3 the variation of cuts only affects the calculation of QCD background. The uncertainty on calculation of  $Z \rightarrow \mu\mu$  background shown

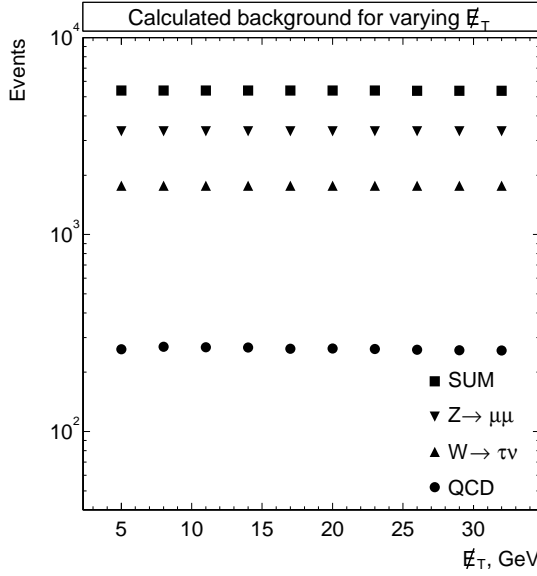


**Figure 6.3.** The background dependence on  $E_T$  cut for  $W$  candidates.

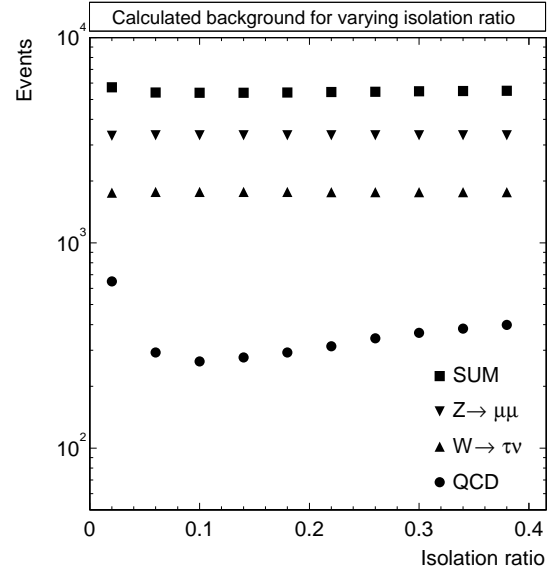


**Figure 6.4.** The background dependence on isolation ratio cut for  $W$  candidates.

$E_T$ cut	QCD	$W \rightarrow \tau \nu$	$Z \rightarrow \mu \mu$	background sum
5 GeV	261	1,769	3,347	5,378
8 GeV	270	1,769	3,346	5,385
11 GeV	268	1,769	3,347	5,384
14 GeV	267	1,769	3,347	5,383
17 GeV	263	1,769	3,347	5,379
20 GeV	264	1,769	3,347	5,380
23 GeV	262	1,769	3,347	5,378
26 GeV	260	1,769	3,347	5,376
29 GeV	258	1,769	3,347	5,375
32 GeV	258	1,769	3,347	5,375
$\bar{n} = \sum n_i / 10$	263	1,769	3,347	5,379
$\Delta n = \sqrt{\sum (n_i - \bar{n})^2 / 9}$	4	0	0	4

**Table 6.2.** The calculated number of the background events in the signal region D for varying  $E_T$  cut.

isolation ratio cut	QCD	$W \rightarrow \tau\nu$	$Z \rightarrow \mu\mu$	background sum
0.02	649	1,757	3,324	5,731
0.06	293	1,768	3,345	5,406
0.10	264	1,769	3,348	5,380
0.14	277	1,769	3,346	5,391
0.18	292	1,768	3,345	5,406
0.22	313	1,768	3,344	5,425
0.26	342	1,767	3,342	5,452
0.30	364	1,766	3,341	5,471
0.34	382	1,766	3,340	5,487
0.38	399	1,765	3,339	5,503
$\bar{n} = \sum n_i/10$	358	1,766	3,341	5,465
$\Delta n = \sqrt{\sum (n_i - \bar{n})^2/9}$	112	3	7	102

**Table 6.3.** The calculated number of the background events in the signal region D for varying isolation ratio cut.

in 6.12 comes from the 1.9 % uncertainty of the recent  $R$  measurement [33]. The uncertainty associated with  $W \rightarrow \tau\nu$  background quoted in 6.12 comes from the 2.9 % uncertainty on the lepton universality measurements [14]. The relative fraction of electroweak background events is given in Equation 6.2. The fraction of QCD background events is

$$b_{QCD}^W = 0.46 \pm 0.15 \text{ \%}. \quad (6.13)$$

Figure 6.5 plots the distributions of the  $\cancel{E}_T$  variable and shows the calculated relative contributions of signal and background events. The shapes of the  $W \rightarrow \mu\nu$  signal,  $W \rightarrow \tau\nu$  background, and  $Z \rightarrow \mu^+\mu^-$  background contributions are taken directly from simulation. The shape of the QCD background is obtained from the data using events that have an isolation ratio greater than 0.1 but pass all other analysis cuts. We note that our method relies on the assumption that  $\cancel{E}_T$  shape for the QCD background from high isolation region models that from low isolation region. The good fit in this plot verifies that this assumption is robust.

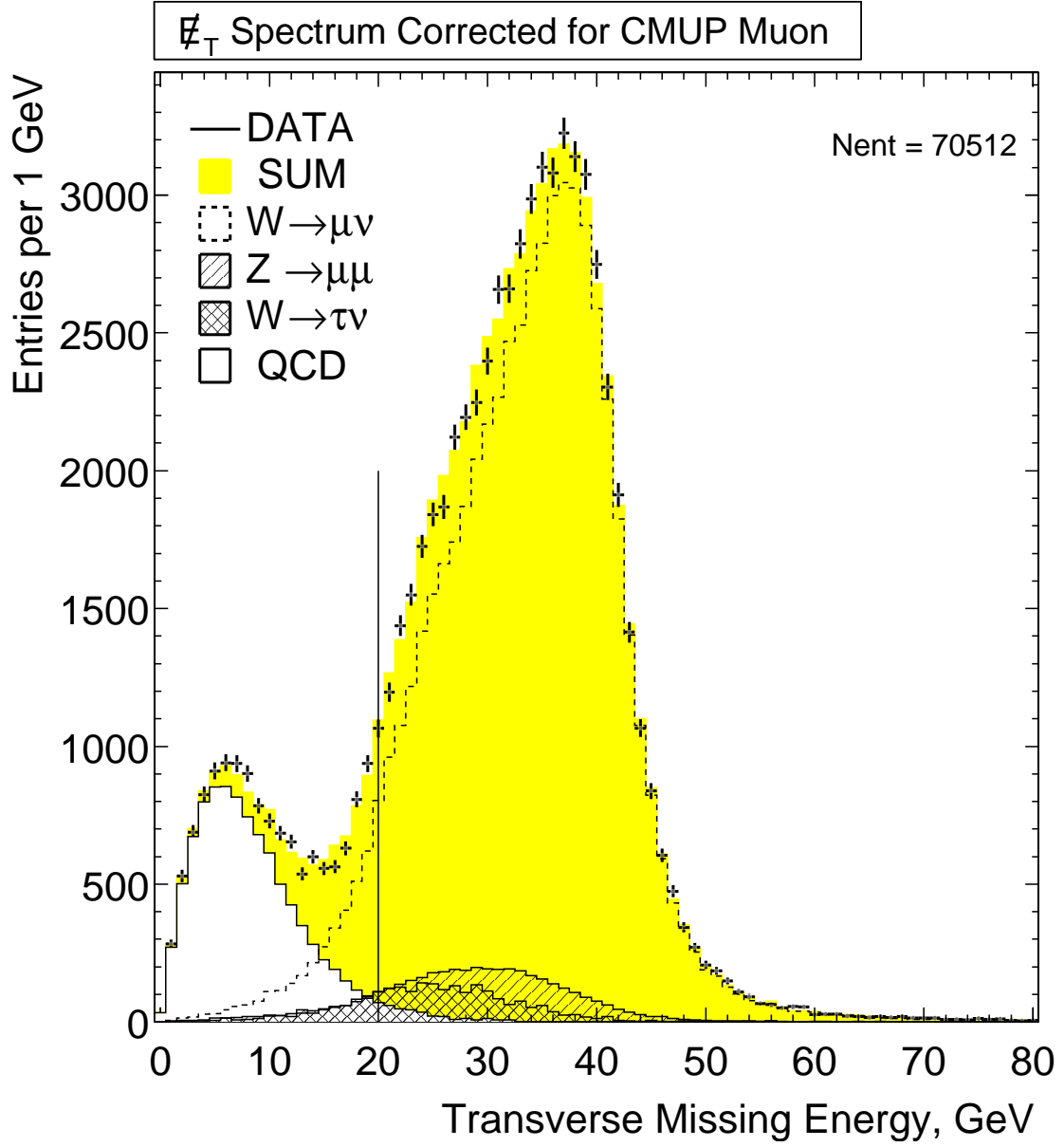


Figure 6.5.  $\cancel{E}_T$  in data and Monte Carlo for  $W \rightarrow \mu\nu$  candidate events.

### 6.3 Cosmic Background

As it was specified in Section 4.2 the signature of  $W$  event can be imitated by a cosmic ray when only one leg of the cosmic is reconstructed. Such an event may pass both  $Z$  veto and  $\cancel{E}_T$  cut due to the transverse momentum imbalance. In this section we attempt to determine the fraction of events due to cosmic rays that slipped through the cosmic tagger. To study such events, we prepare a “cosmic-rich” data sample: muons must pass the requirements of Table 4.1, except for the impact parameter cut, and in addition only events with the small number of tracks  $n_{trk} < 5$  are selected. Our “cosmic-rich” sample contains 178 events out of which 119 events have both CMP and CMU hits on the opposite side of the detector from the trigger muon. We conclude that about  $119/178 = 67 \pm 4$  % of cosmic events have opposite side muon hits.

For cosmic ray event the muon chamber hits are positioned near the straight line of a cosmic ray trajectory. We search for both CMP and CMU hits which are positioned on the opposite side of the detector from the trigger muon according to the following rules:

- Look for a CMP hit, which is the closest to the extrapolated cosmic ray track and calculate the azimuthal location in the CDF coordinate system. If the distance between found hit and expected cosmic ray is small:  $|\phi_{CMP} - \phi_{cosm}| \geq 0.5$  rad, consider the event.
- Look for CMU hits matching the found CMP hit and calculate the azimuthal location. If the distance between found CMU and CMP hits is small:  $|\phi_{CMP} - \phi_{CMU}| \geq 0.05$  rad, consider the event.

Using this algorithm we found 398 events out of the  $W$  candidate sample. Some of these are cosmic ray events that passed the cosmic tagger as discussed above. However there are additional  $Z$  events that escaped  $Z$ -veto perhaps because of hard photon radiation along the muon, and  $W$  events with jets and noise.

To understand the true cosmic fraction, we can examine the CMU hit position distribution relative to the projected cosmic ray hit both in transverse plane and along  $\hat{z}$  direction. In transverse plane collision events from  $W$  with jet or  $Z$  decay may have CMU hits on the opposite side of the detector from the trigger muon. However, we do not expect “back-to-back” signature for the collision events in  $\hat{z}$  direction. Figures 6.6 and 6.7 show  $z_{CMU} - z_{cosm}$  variable distribution both for “cosmic-rich” and  $W$  candidate samples.

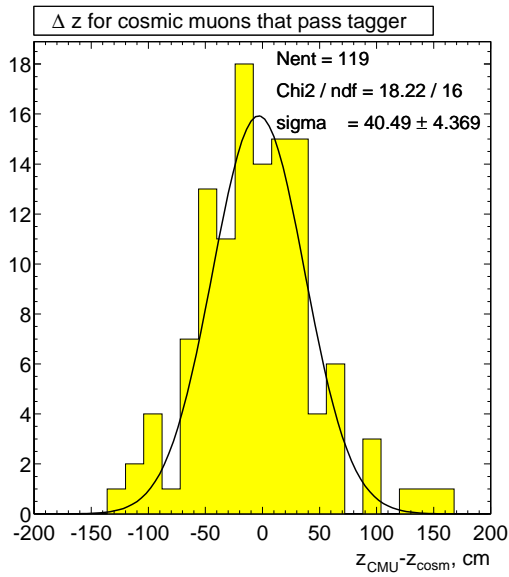


**Figure 6.6.** The difference between  $\hat{z}$  components of CMU hits and projected cosmic ray hit for cosmes data.

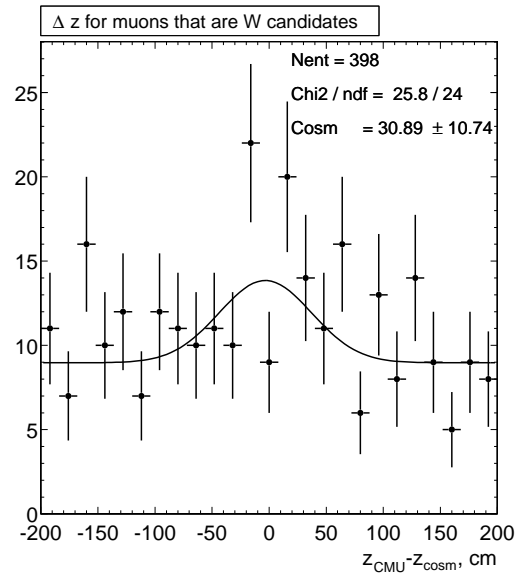


**Figure 6.7.** The difference between  $\hat{z}$  components of CMU hits and projected cosmic ray hit for  $W$  data.

The distribution for the cosmic sample peaks near 0 with the Gaussian width around 40 cm, whereas the distribution for the  $W$  sample looks rather flat. To determine the number of possible cosmic events in  $W$  data we fit the Figure 6.7 distribution with sum of Gaussian and constant. The mean and the width of the Gaussian are fixed at 0 and 40 respectively. The return value of the fit for Gaussian maximum suggests that the possible number of cosmic events with the found both CMU and CMP hits is  $30.9 \pm 10.7$ . To obtain the total number of cosmic events in  $W$  sample we have to divide the number obtained from the fit by the fraction of cosmes

events for which both CMU and CMP hits are found opposite to the muon:

$$B_{cosm}^W = \frac{30.9 \pm 10.7}{0.67 \pm 0.04} = 46.1 \pm 16.1 \quad \text{or} \quad b_{cosm}^W = 0.08 \pm 0.03 \%. \quad (6.14)$$

The remaining events in the flat background on figure 6.7 are accounted for the  $Z \rightarrow \mu\mu$  background, which is considered in more details in the previous subsection.

## CHAPTER 7

### Z Selection Criteria

The  $Z \rightarrow \mu^+\mu^-$  cross section measurement utilizes the same high- $P_T$  muon dataset and the same good run list that are used for the  $W$  measurement, which is described in detail in Chapters 3 and 4.

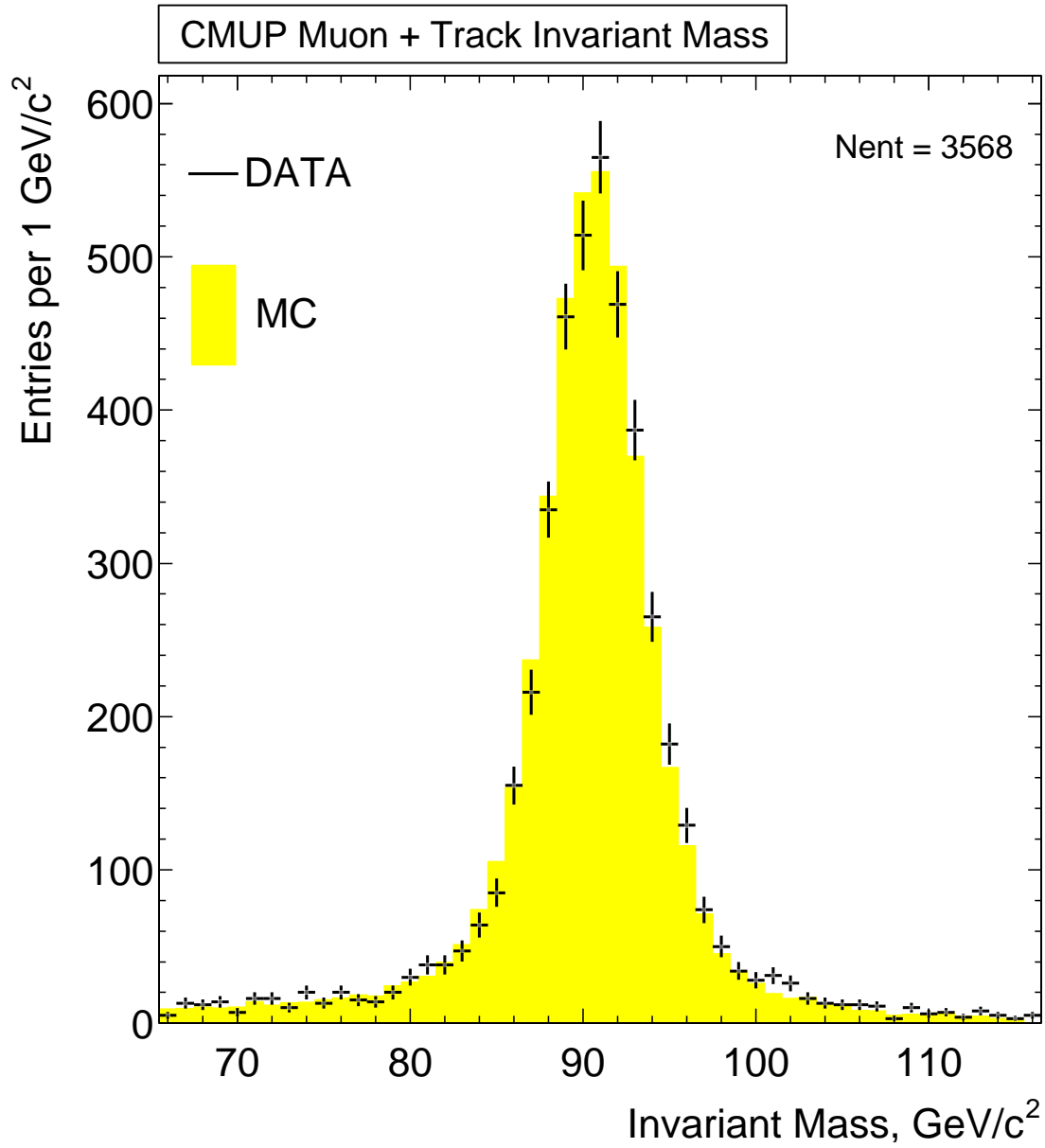
Every  $Z$  candidate event represents a muon-track pair, in which both legs must pass a **loose** set of cuts and at least one leg must pass a **tight** selection. This way we can greatly improve our acceptance and simplify our efficiency calculation without taking on additional background.

Figure 7.1 shows the invariant mass distribution for the selected  $Z \rightarrow \mu^+\mu^-$  candidate events. The measured muon  $P_T$  in simulation events has been tuned to give the best agreement with the data [20].

The **tight** muon is required to pass all of the kinematic and identification criteria used to select muon candidates in the  $W$  analysis. The full set of selection criteria for the **tight** muon was shown in Table 4.1. Note that the **tight** muon is also required to be the trigger muon in the event. This trigger requirement means that we reject events that make it into our sample exclusively via the CMX high- $P_T$  trigger path even if the events contain a second CMUP muon candidate that satisfies all of the other selection criteria for **loose** muons.

**Loose** muons are isolated COT tracks pointing at minimum ionizing energy deposits in the calorimeter. We also make sure that the **loose** muon leg traverse all eight COT super-layers before exiting the tracker. This requirement guarantees high





**Figure 7.1.** Dimuon invariant mass  $M_{\mu\mu}$  distribution in data and simulation for  $Z \rightarrow \mu^+\mu^-$  candidate events.

uniform efficiency for COT track reconstruction.

The full set of kinematic and identification cuts applied to the **loose** muon are listed in upper part of Table 7.1.

Requirement	Purpose	Number of Passed Events
Inclusive Muon	Quality Muon	77,140
Second High- $P_T$ Track	Second Leg of $Z$	9,565
$P_T > 20 \text{ GeV}/c$	Low- $P_T$ Noise Reduction	6,202
$ z_0^T - z_0^L  < 4 \text{ cm}$	Same Vertex Tracks	6,084
COT Radius $\rho \geq 140 \text{ cm}$	Fiducial Tracks	4,408
$E_{EM} < 2 \text{ GeV}$	Minimum Ionizing Deposition	4,223
$E_{HAD} < 6 \text{ GeV}$	Minimum Ionizing Deposition	4,186
$3 \leq N_{Seg}^{Ax}, 3 \leq N_{Seg}^{St}$	Good Track Quality	4,047
$ d_0^{cor}  < 0.2 \text{ cm}$	Good Track Quality	4,018
$\chi_{COT}^2/ndf < 2$	Good Track Quality	4,018
$Iso < 0.1$	Background Reduction	3,905
$66 < M < 166 \text{ GeV}/c^2$	Mass Range of Measurement	3,568
$Q^T = -Q^L$	Opposite Charge Tracks	3,568

**Table 7.1.** Loose muon cuts for  $Z \rightarrow \mu^+ \mu^-$  selection.

In order to ensure that both muons come from the same event vertex, we require that the distance between  $z_0$  of the two tracks is less than 4.0 cm. We also require that the two muon candidates have opposite charges. For the current data set, neither of these requirements removes any events from our candidate sample. As in other CDF electroweak analyses [34] we require that the invariant mass of the muon pair lies between  $66 \text{ GeV}/c^2$  and  $116 \text{ GeV}/c^2$ .

In some fraction of candidate events, we find two reconstructed muons that satisfy the **tight** muon selection criteria. Since the **loose** muon criteria are a subset of the **tight** muon criteria, all events of this type make it into our final candidate sample. However, in calculating the overall efficiency for selecting  $Z \rightarrow \mu^+ \mu^-$  events, we must consider events with two muons pointing at both the CMU and CMP chambers as a special case since both will have the opportunity to satisfy the **tight** muon requirements and the trigger. This calculation will be discussed in much greater detail in a Section 10.2

of this thesis.

The yield of  $Z$  candidate events per data-taking runs for the whole period is shown on Figure 7.2. The run interval is sampled in the ranges, with the corresponding integrated luminosity of at least  $8 \text{ pb}^{-1}$ . Figure 7.3 shows  $Z$  event count per inverse picobarn of delivered luminosity for various run ranges, which is a relatively flat distribution.

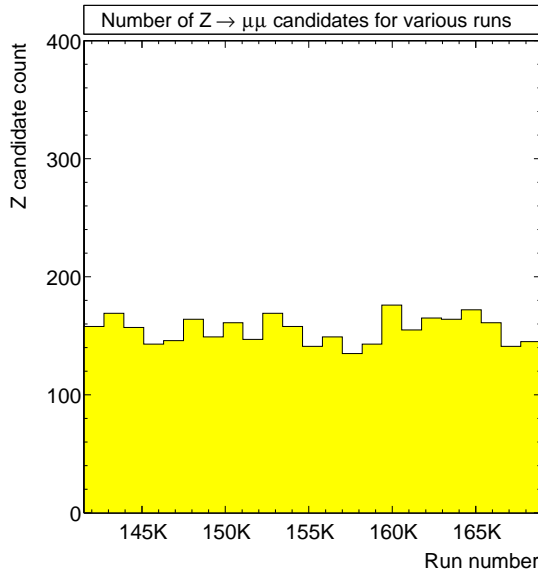


**Figure 7.2.** Number of  $Z$  candidate events per a run range.

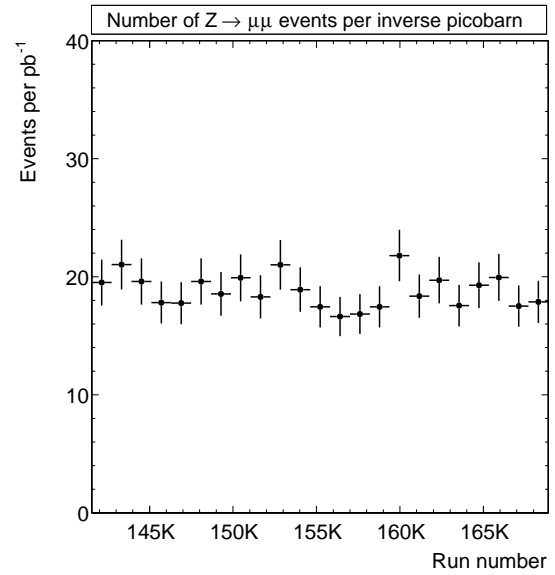


**Figure 7.3.**  $Z$  candidate yield per inverse picobarn of delivered luminosity.

## CHAPTER 8

### *Z* Backgrounds

Because of the requirement for a second muon we expect the fraction of background events for  $Z \rightarrow \mu^+\mu^-$  process to be much smaller than in case of  $W \rightarrow \mu\nu$  analysis. The leading backgrounds described in this section are cosmic rays,  $Z \rightarrow \tau^+\tau^-$  and QCD processes. The sum of all these contributing background processes, described in detail in the subsections below, yields a total fraction of background events in the  $Z$  sample of

$$b_Z = 0.36 \pm 0.19 \text{ \%}. \quad (8.1)$$

#### 8.1 Cosmic Background

The cosmic ray background is estimated by looking at the 3- $D$  opening angle between muon legs in  $Z$  decay. We expect muon legs from cosmic rays to be “back-to-back” with the opening angle distribution peaking at  $\pi$  as shown on Figure 8.1. This distribution falls sharply and ends at the angle value of about 2.8 radians. We compare opening angle distributions in  $Z$  data versus  $Z \rightarrow \mu\mu$  simulation as shown in Figure 8.2. We find 2207 data and 19572 simulation events in the angle interval from 0 to 2.8 radians. The total number of events is 3568 for data  $Z$  candidates and 31556 for simulation. We normalize the distributions such that the areas for both  $Z$  data and simulation histograms are equal in the interval from 0 to 2.8 radians. The normalization scale factor is:

$$19572/(31556 - 19572) = 0.612 \pm 0.003 \text{ .} \quad (8.2)$$

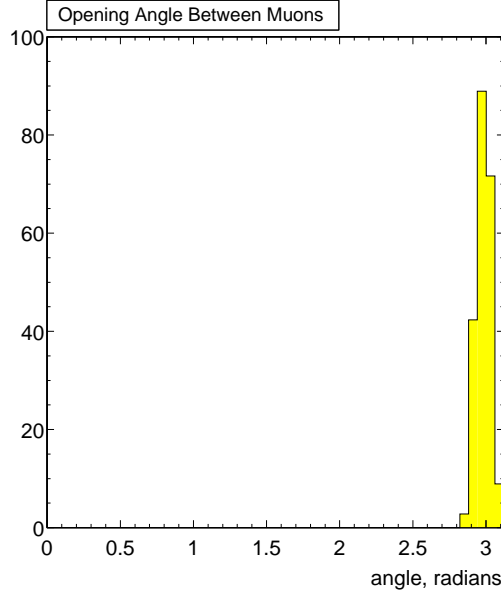


**Figure 8.1.** The distribution of 3-D opening angle between muon legs in cosmic ray events.

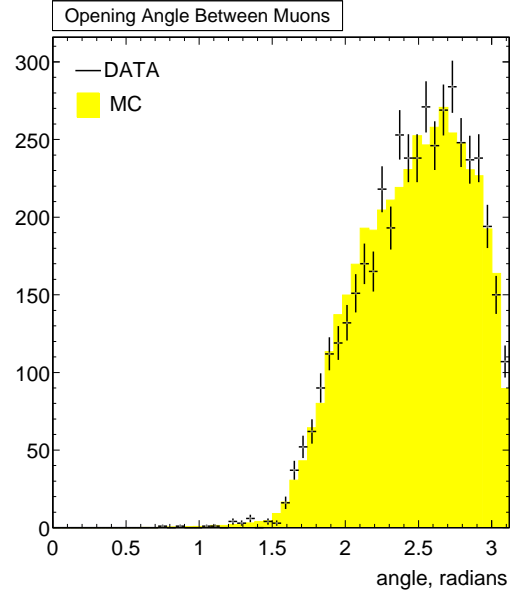


**Figure 8.2.** The distribution of 3-D opening angle between muon legs in collision data, compared to  $Z \rightarrow \mu\mu$  Monte Carlo.

We then look at the excess of the entries in the data over the simulation in the region from 2.8 to  $\pi$  radians. The estimated fraction of cosmic is

$$B_{cosm}^Z = (3568 - 2207) - 2207 \cdot 0.612 = 10 \pm 7 \quad \text{or} \quad b_{cosm}^Z = 0.27 \pm 0.19 \%. \quad (8.3)$$

## 8.2 Electroweak Processes

The background from  $Z \rightarrow \tau\tau$  process is significantly suppressed both by kinematics and by the square of branching ratio  $B(\tau \rightarrow \mu\nu\bar{\nu})$ . Kinematic suppression is due to the partial smearing of dimuon invariant mass distribution toward lower values outside the  $66 - 116 \text{ GeV}/c^2$  mass window. Using the 490,000 simulated  $Z \rightarrow \tau\tau$  events we counted 27 events. On the other hand, out of 472,500 simulated  $Z \rightarrow \mu\mu$  events, we select 31,556 events. The estimated fraction of background event due to  $Z \rightarrow \tau\tau$  process is, therefore

$$b_{\tau\tau}^Z = \frac{27/490,000}{31,556/472,500} = 0.089 \pm 0.017 \%, \quad (8.4)$$

where the uncertainty is due to the limited statistics.

### 8.3 QCD Backgrounds

We attribute the remainder of the contributing background to the QCD processes. Contrary to cosmic rays and electroweak processes, the dimuon fakes from these background events may have the same sign charges. In order to estimate the number of the QCD background events we assume that the number of fake events where both tracks have the same charges should be close to the number of fake events where both tracks have the opposite charges. For the current data set, we observe no same charge events and our estimate of the number of QCD events is

$$B_{QCD}^Z = 0_{-0}^{+1.1} \quad \text{or} \quad b_Z = 0.00_{-0.00}^{+0.03} \%, \quad (8.5)$$

where the error intervals come from one standard deviation confidence level for Poisson statistics with 0 counted events.

## CHAPTER 9

### Acceptances

The geometrical and kinematic requirements of  $W$  and  $Z$  selections result in limited acceptance for detecting these processes. To calculate the acceptance for  $W$  and  $Z$  cases we use the Monte Carlo simulation samples `wewk0m` and `zewk0m`. Tables 9.1–9.2 summarize the number of events that pass various geometrical and kinematic cuts.

Selection Stage	Number of Events
All Simulated Events	2,026,500
Luminous Beam Region $ z_0  < 60 \text{ cm}$	1,960,283
CMUP Fiducial Track	365,891
COT Radius $\rho \geq 140 \text{ cm}$	365,891
Track $P_T \geq 20 \text{ GeV}/c$	304,999
$\cancel{E}_T \geq 20 \text{ GeV}$	285,151
$Z$ -veto	284,428

**Table 9.1.**  $W$  acceptance calculation.

Selection Stage	Number of Events
All Simulated Events	472,500
Beam Region $ z_0  < 60 \text{ cm}$	456,912
$66 < M_{gen} < 116 \text{ GeV}/c^2$	341,119
First Leg CMUP Fiducial	113,582
First Leg $P_T \geq 20 \text{ GeV}/c$	103,212
Second Leg $\rho \geq 140 \text{ cm}$	39,541
Second Leg $P_T \geq 20 \text{ GeV}/c$	39,455
$66 < M_{rec} < 116 \text{ GeV}/c^2$	39,341

**Table 9.2.**  $Z$  acceptance calculation.

The values above the double line in these tables are the number of events that represent the denominator in the ratio for the acceptance calculation. The number of events in the numerator are taken from the last entry of the Tables 9.1–9.2. Thus:

$$A_W = 284,428/1,960,283 = 0.1451^{+0.0020}_{-0.0024} \quad (9.1)$$

$$A_Z = 39,341/341,119 = 0.1153^{+0.0021}_{-0.0026} \quad (9.2)$$

where  $A_W$ —the acceptance for selecting  $W \rightarrow \mu\nu$  process, and  $A_Z$ —the acceptance for selecting  $Z \rightarrow \mu\mu$  process. The expected ratio of acceptances is

$$A_Z/A_W = 0.1153/0.1451 = 0.7949^{+0.0068}_{-0.0076} \quad (9.3)$$

The errors quoted in Equations 9.1, 9.2 and 9.3 are the combined systematic uncertainties that have been studied previously in greater detail in [20]. The results of these studies are summarized in the Table 9.3.

Uncertainty Source	$\delta A_W$ , %	$\delta A_Z$ , %	$\delta(A_Z/A_W)$ , %
Simulation Statistics	0.18	0.46	0.49
Momentum Scale	0.21	0.05	0.16
Recoil Model	0.36	—	0.36
W Z Transverse Motion	0.04	0.08	0.12
Parton Distributions	+1.30 -1.61	+1.74 -2.23	+0.56 -0.71
All Combined	+1.38 -1.67	+1.80 -2.28	+0.85 -0.96

**Table 9.3.** Summary of uncertainties for calculating the acceptance ratio

The most relevant quantity for both  $W$  and  $Z$  acceptance calculations is the boson rapidity  $y$  defined by Equation 1.18. For vector boson production at Tevatron the range of rapidity values is  $|y| < 3$ . However the limited rapidity coverage of muon and tracking chambers makes our acceptance calculations sensitive to the boson rapidity. The boson rapidity distribution depends on the parton distribution functions according to Equation 1.22. We use CTEQ5L [30] parton distribution function similar to those shown in Figure 1.5 to evaluate the central value of acceptance, and we compute the uncertainties from 20 pairs of eigenvectors basis sets available from CTEQ6M. Using this method we obtain the asymmetric values quoted in Table 9.3. It turns out that systematic errors due to the parton distribution functions is the largest source of uncertainties in this analysis. The relative error value for this uncertainty is about 2 % for  $W$  and  $Z$  acceptances. However, for the ratio of acceptances this uncertainty is significantly reduced to the relative error value of about 0.7 %.

The vector boson transverse motion is not not accounted by the leading order calculations used for our simulation. Therefore in order to include the transverse motion of  $W$  and  $Z$  bosons in our Monte Carlo samples we have to include the vector boson transverse momentum spectrum as an input to our generator. We assume that  $W$  and  $Z$  transverse momentum distributions represent the same spectrum, therefore



we use the experimental measurement of  $P_T^Z$  spectrum based on our  $Z \rightarrow \mu\mu$  candidates. Several `PYTHIA` parameters are used to tune vector boson  $P_T^V$  spectrum in our generator to match the measured  $P_T^Z$  distribution [20].

In order to account for potential differences in COT momentum measurements between the data and simulation samples we introduce a “momentum scale” uncertainty. The origin of this uncertainty is the potential difference between the magnetic field description in the detector simulation software and the actual value of magnetic field inside the COT. In order to study this difference we multiply the reconstructed value of muon  $P_T$  by a correction factor for every entry in our Monte Carlo simulation. Then we compare a benchmark distribution such as dimuon invariant mass  $Z$  spectrum shown on Figure 7.1 both for the data and simulation samples. We adjust the correction factor to get the best fit between the data and Monte Carlo distributions.

The recoil energy is related to the leftover calorimeter energy measurement when muon deposition is excluded. This parameter is essential only to the  $W$  acceptance measurement, since it smears the overall missing transverse energy. In order to study how significant is the uncertainty due to the recoil energy modeling, we compared the calorimeter energy distributions between our  $W \rightarrow \mu\nu$  data and Monte Carlo samples using the same method as described in the previous paragraph. The obtained values for acceptance uncertainties due to recoil energy modeling are quoted in Table 9.3.

Finally a parameter which we will need for evaluating the efficiency of  $Z$  selection cuts in Chapter 10 is the fraction of events where both muon legs from  $Z$  decay fall into the fiducial region of both CMU and CMP chambers. Out of 39,341 selected events passing basic kinematic and geometrical requirements from Table 9.2 we find 10,307 events with both legs of  $Z$  pointing to CMU and CMP fiducial regions:

$$f = 10,307/39,341 = 0.262 \pm 0.002 \quad (9.4)$$

where the error is based on statistical uncertainty only.

## CHAPTER 10

### Efficiencies

Three major types of the muon efficiencies correspond to muon reconstruction, triggering, and identification. In order to account for potential variation of these efficiencies during the data-taking period we determine them directly from our  $Z$  candidate event sample. The muons from  $Z$  decay will have a similar kinematics to those from  $W$  decay and will be embedded in a similar event environment.

The method for measuring the efficiencies of various requirements that we apply for the muon is based on utilizing the unbiased leg of  $Z$  boson. The event sample in this case is merely two high- $P_T$  tracks that have opposite sign charges and form an invariant mass within the window  $80 < M < 100 \text{ GeV}/c^2$ . Regardless of what efficiency we measure, the biased leg must always be a reconstructed muon that triggered the event and passes all muon identification cuts. The unbiased or *probe* leg must at least point to fiducial regions of both CMU and CMP muon chambers.

To measure the reconstruction efficiency we apply muon identification cuts to the probe leg except for the stub matching requirements. We then divide the number of probe legs that have both CMU and CMP stubs reconstructed by the number of all found probe legs:

$$\epsilon_{rec} = 2,499/2,735 = 0.9137 \pm 0.0054 \quad (10.1)$$

To measure the trigger efficiency we require the probe leg to have both CMU and CMP stubs reconstructed. We also apply all muon identification cuts to the unbiased leg including the stub matching requirements. We then take a ratio of the number of

probe legs that have associated local trigger to the number of all found probe legs:

$$\epsilon_{trg} = 2,116/2,355 = 0.8985 \pm 0.0062 . \quad (10.2)$$

In addition to the local trigger, there are inefficiencies associated to the global trigger path. We found that out of 722  $Z$  events for which at least one leg has associated local trigger, 720 events have passed the global trigger requirement:

$$\epsilon_{L3} = 720/722 = 0.9972 \pm 0.0020 . \quad (10.3)$$

To measure the efficiency of muon identification cuts we require the probe leg to have both CMU and CMP stubs reconstructed. We also apply remaining muon identification cuts that we are not measuring to the unbiased leg. The efficiencies for muon identification when various cuts are applied simultaneously are:

$\epsilon'_{id}$ —the efficiency to identify the **loose** leg,

$\epsilon_{dx}$ —the efficiency of matching a muon track to its CMU and CMP stubs,

$\epsilon_{id}$ —the efficiency to identify the **tight** leg.

The measured values for these parameters are listed as the last three entries in the Table 10.1 along with the other efficiencies.

Applied Cut	Label	Ratio	Efficiency
$E_{EM} < 2 \text{ GeV}$	$\epsilon_{em}$	2,355 / 2,428	0.9699±0.0035
$E_{HAD} < 6 \text{ GeV}$	$\epsilon_{had}$	2,355 / 2,394	0.9837±0.0026
$N_{Seg}^{Ax} \geq 3, N_{Seg}^{St} \geq 3$	$\epsilon_{seg}$	2,355 / 2,419	0.9735±0.0033
$ d_0^{cor}  < 0.2 \text{ cm}$	$\epsilon_{d_0}$	2,355 / 2,361	0.9975±0.0010
$\chi_{COT}^2/ndf < 2$	$\epsilon_{\chi}$	2,355 / 2,355	1.000
$Iso < 0.1$	$\epsilon_{iso}$	2,355 / 2,395	0.9833±0.0026
All Combined Without Muon Stub Matching	$\epsilon'_{id}$	2,355 / 2,595	0.9075±0.0057
$ \Delta X _{CMU} < 3 \text{ cm}$	$\epsilon_{dx}$	2,355 / 2,499	0.9424±0.0047
$ \Delta X _{CMP} < 5 \text{ cm}$			
All Combined	$\epsilon_{id}$	2,355 / 2,748	0.8570±0.0067

**Table 10.1.** Muon identification efficiencies

## 10.1 Efficiency for Selecting $W$

We define the efficiency of detecting the muon from  $W$  decay according to the expression

$$\epsilon_W = \epsilon_{z_0} \epsilon_W^{cr} \epsilon_{trk} \epsilon_{L3} \epsilon_{trg} \epsilon_{rec} \epsilon_{id}. \quad (10.4)$$

The last four variables were described in the previous subsection. The additional efficiencies related to the  $W$  selection are:

$\epsilon_{z_0}$ —the efficiency of  $z_0$  track cut,

$\epsilon_W^{cr}$ —the overefficiency of cosmic ray tagger,

$\epsilon_{trk}$ —COT track reconstruction efficiency.

The efficiency of the  $z_0$  track cut is measured independently by using minimum bias events. The method is based on the measurement of longitudinal profile of the  $p\bar{p}$  luminous region and calculating the fraction of events that falls inside the region  $|z_0| < 60$  cm. A separate note [20] describes the measurement in more detail and quotes the efficiency value:

$$\epsilon_{z_0} = 0.948 \pm 0.003, \quad (10.5)$$

where statistical and systematic uncertainties have been included in the error.

A small fraction of muon tracks originating from  $W$  decay can be misidentified as a cosmic ray by the cosmic tagger. The overefficiency of cosmic ray tagger  $\epsilon_{cr}$  is measured using the electron  $W$  and  $Z$  samples [26]. Since the electron samples are free of cosmic ray background, the fake number of tags observed in these samples is a reliable measure of the overefficiency of our algorithm for tagging real  $W \rightarrow \mu\nu$  and  $Z \rightarrow \mu\mu$  processes. The method is outlined in more detail in a separate note [20]. The measured values are:

$$\epsilon_W^{cr} = 0.9999 \pm 0.0001 \quad \text{and} \quad \epsilon_Z^{cr} = 0.9994 \pm 0.0006, \quad (10.6)$$

where the quoted error includes both statistical and systematic uncertainties.

The COT tracking efficiency is estimated using a sample of  $W \rightarrow e\nu$  candidates collected by `W_NOTRACK` trigger path. To reconstruct an electron object in this sample one requires an energetic electromagnetic cluster in the calorimeter, which is matched with the track from silicon detector. The presence of a COT link between the silicon track and the calorimeter cluster is a good measure of COT track reconstruction efficiency. To account for inefficiency due to Bremsstrahlung radiation in electrons a comparison to  $W \rightarrow e\nu$  Monte Carlo sample is made. A separate note [36] describes the measurement in more detail and quotes the efficiency value:

$$\epsilon_{trk} = 0.996 \pm 0.003 . \quad (10.7)$$

We use the efficiency numbers from Table 10.1 and Equations 10.1–10.7 to calculate the efficiency for  $W \rightarrow \mu\nu$  process:

$$\epsilon_W = 0.661 \pm 0.009 . \quad (10.8)$$

## 10.2 Efficiency for Selecting $Z$

The efficiency expression for selecting  $Z \rightarrow \mu^+\mu^-$  candidates differs significantly from efficiency of  $W \rightarrow \mu\nu$ , since our selection requires both **tight** and **loose** muons are present in our final sample.

We define the efficiency of detecting the **loose** muon according to the expression

$$\epsilon_L = \epsilon_{trk}\epsilon'_{id} , \quad (10.9)$$

where  $\epsilon_{trk}$ —track reconstruction efficiency;  $\epsilon'_{id}$ —the combined efficiency of muon identification cuts without applying stub matching requirements.

Detecting a **tight** muon requires CMU and CMP stub reconstruction and matching, and the efficiency can be expressed as

$$\epsilon_T = \epsilon_L\epsilon_{rec}\epsilon_{dx} , \quad (10.10)$$

where  $\epsilon_{rec}$ —efficiency for a track to be linked to both CMU and CMP reconstructed stubs; and  $\epsilon_{dx}$ —efficiency for a track to match both CMU and CMP stubs within  $\Delta X$  cuts.

To combine  $\epsilon_L$  and  $\epsilon_T$  into  $\epsilon_Z$ , we must consider several distinct categories of muon pairs:

- *Both muons are in CMUP fiducial region with CMU and CMP stubs.*

When both CMU and CMP stubs are present for loose muon the efficiency  $\epsilon_L$  is multiplied by the factor  $\epsilon_{rec}$ . Also, depending on track-stub matching, the loose muon efficiency becomes

$$\epsilon_L \epsilon_{rec} (1 - \epsilon_{dx}) \quad (10.11)$$

when muon fails  $\Delta X$  cuts, and

$$\epsilon_L \epsilon_{rec} \epsilon_{dx} = \epsilon_T \quad (10.12)$$

when muon passes  $\Delta X$  cuts. The efficiency combinations for various cases are:

$$\begin{aligned} \epsilon_T^2 & \quad \text{— both muons pass tight selection} \\ \epsilon_T \epsilon_L \epsilon_{rec} (1 - \epsilon_{dx}) & \quad \text{— only first muon passes tight selection} \\ \epsilon_L \epsilon_{rec} (1 - \epsilon_{dx}) \epsilon_T & \quad \text{— only second muon passes tight selection} \\ (\epsilon_L \epsilon_{rec} (1 - \epsilon_{dx}))^2 & \quad \text{— no tight muon—event is rejected} \end{aligned}$$

We also have to take care of trigger efficiencies for each case considered above:

$$\begin{aligned} \epsilon_{trg} (2 - \epsilon_{trg}) & \quad \text{— both muons pass tight selection} \\ & \quad \text{and at least one muon triggers the event} \\ \epsilon_{trg} & \quad \text{— first muon is tight and triggers the event} \\ \epsilon_{trg} & \quad \text{— second muon is tight and triggers the event} \end{aligned}$$

By combining the efficiencies for each cases we obtain the following result for this category of  $Z \rightarrow \mu^+ \mu^-$  events:

$$\epsilon_{trg} (2 - \epsilon_{trg}) \epsilon_T^2 + 2 \epsilon_{trg} \epsilon_T \epsilon_L \epsilon_{rec} (1 - \epsilon_{dx}) = \epsilon_{trg} \epsilon_T \epsilon_L \epsilon_{rec} (2 - \epsilon_{trg} \epsilon_{dx}). \quad (10.13)$$

- *Both legs in CMUP region but only the tight leg has both CMU and CMP stubs.*

In this case, for some reason the muon reconstruction fails to provide both CMU and CMP stubs for loose leg of  $Z$ . Under this condition the efficiency for the loose leg becomes

$$\epsilon_L(1 - \epsilon_{rec}). \quad (10.14)$$

The only observed outcomes in this case is when first leg is **tight** and second is **loose** or first leg is **loose** and second is **tight**, the sum over which is

$$2\epsilon_T\epsilon_L(1 - \epsilon_{rec}). \quad (10.15)$$

The trigger efficiency enters the  $\epsilon_Z$  expression for this case simply as a factor  $\epsilon_{trg}$ , since only the **tight** muon can trigger the event.

The combined  $\epsilon_Z$  result for this category of  $Z \rightarrow \mu^+\mu^-$  events is

$$2\epsilon_{trg}\epsilon_T\epsilon_L(1 - \epsilon_{rec}). \quad (10.16)$$

- *Only tight muon is CMUP-fiducial, but loose leg is outside of CMUP region.*

For this case, the **loose** leg of  $Z$  is directed in such a way that it does not hit both CMU and CMP chambers at the same time. Under this condition, the efficiency to detect the **loose** leg is simply  $\epsilon_L$ . The only one observed outcome in this case is when CMUP leg is **tight** and the other leg is **loose**, which corresponds to the selection efficiency

$$\epsilon_T\epsilon_L. \quad (10.17)$$

The trigger efficiency enters the  $\epsilon_Z$  expression for this case simply as a factor  $\epsilon_{trg}$ , since only the **tight** muon can trigger the event.

The combined  $\epsilon_Z$  result for this category of  $Z \rightarrow \mu^+\mu^-$  events becomes

$$\epsilon_{trg}\epsilon_T\epsilon_L. \quad (10.18)$$

Now that we have considered all the cases, we can combine them together weighing by the fractions<sup>1</sup>  $f$  and  $(1 - f)$  for Equations 10.13–10.16 and 10.18 respectively:

$$\begin{aligned} f\epsilon_{trg}\epsilon_T\epsilon_L\epsilon_{rec}(2 - \epsilon_{trg}\epsilon_{dx}) + 2f\epsilon_{trg}\epsilon_T\epsilon_L(1 - \epsilon_{rec}) + (1 - f)\epsilon_{trg}\epsilon_T\epsilon_L = \\ = \epsilon_{trg}\epsilon_T\epsilon_L[1 + f(1 - \epsilon_{trg}\epsilon_{rec}\epsilon_{dx})] \end{aligned} \quad (10.19)$$

To finalize our result we multiply the combined result 10.19 by the efficiencies of track  $z_0$ , cosmic tagging and global trigger:

$$\epsilon_Z = \epsilon_{z0}\epsilon_Z^{cr}\epsilon_{L3}\epsilon_{trg}\epsilon_T\epsilon_L[1 + f(1 - \epsilon_{trg}\epsilon_{rec}\epsilon_{dx})]. \quad (10.20)$$

While expression for  $\epsilon_Z$  looks a bit complicated we note that when  $\epsilon_{trg} \approx 1$ ,  $\epsilon_{rec} \approx 1$ , and  $\epsilon_{dx} \approx 1$  the expression  $[1 + f(1 - \epsilon_{trg}\epsilon_{rec}\epsilon_{dx})]$  in brackets reduces to  $\approx 1$  for arbitrary values of  $f$ . Thus, Equation 10.20 turns into more simplified form  $\epsilon_{z0}\epsilon_Z^{cr}\epsilon_{L3}\epsilon_{trg}\epsilon_T\epsilon_L$ , which is a good estimate for  $\epsilon_Z$ .

We use the efficiency numbers from Equations 10.1, 10.2, 10.3 and Table 10.1 to calculate the efficiency for  $Z \rightarrow \mu^+\mu^-$  process:

$$\epsilon_Z = 0.633 \pm 0.011 \quad (10.21)$$

### 10.3 Ratio of Efficiencies

To calculate the ratio of efficiencies  $\epsilon_Z/\epsilon_W$  we use the Equations 10.4 and 10.20. When we evaluate this ratio we notice that the product of efficiencies  $\epsilon_{z0}\epsilon_{cr}\epsilon_{L3}\epsilon_{trg}\epsilon_T$  in expression for  $\epsilon_Z$  is equivalent to the definition of  $\epsilon_W$  according to the Equations 10.4 and 10.10. Canceling these parameters in the ratio we obtain

$$\epsilon_Z/\epsilon_W = \epsilon_Z^{cr}\epsilon_L[1 + f(1 - \epsilon_{trg}\epsilon_{rec}\epsilon_{dx})]/\epsilon_W^{cr}. \quad (10.22)$$

We use the efficiency numbers from Table 10.1 and Equations 10.1–10.7 to calculate the numeric value for the efficiency ratio

$$\epsilon_Z/\epsilon_W = 0.957 \pm 0.007. \quad (10.23)$$

---

<sup>1</sup>refer to Chapter 9 for definition of  $f$



## CHAPTER 11

### Result

We wish to measure the product of the production cross section and the branching ratio for a vector boson decay

$$\sigma(p\bar{p} \rightarrow V) \cdot BR(V \rightarrow \mu X) = \frac{N(1-b)}{A\epsilon \int L dt}, \quad (11.1)$$

where:  $N$  is the number of candidate events passing the selection,  $b$  is the estimated fraction of background events,  $A$  is the detector acceptance,  $\epsilon$  is the efficiency of the selection cuts,  $\int L dt$  is the luminosity integral.

Alternatively, we can combine our sensitivity to both  $W$  and  $Z$  decays to measure a luminosity independent cross section ratio

$$R = \frac{\sigma(p\bar{p} \rightarrow W) \cdot BR(W \rightarrow \mu\nu)}{\sigma(p\bar{p} \rightarrow Z) \cdot BR(Z \rightarrow \mu\mu)} = \frac{N_W(1-b_W)}{N_Z(1-b_Z)} \frac{A_Z}{A_W} \frac{\epsilon_Z}{\epsilon_W}. \quad (11.2)$$

The measured input parameters for these calculations [11.1](#)–[11.2](#) summarizing all the

Parameter	W	Z	Ratio R
Integrated Luminosity	$\int L dt$ 193.5±11.6 pb <sup>-1</sup>	$\int L dt$ 193.5±11.6 pb <sup>-1</sup>	
Number Of Candidates	$N_W$ 57,109	$N_Z$ 3,568	$\frac{N_W}{N_Z}$ 16.006
Background Fraction	$b_W$ 0.0949±0.0045	$b_Z$ 0.0036±0.0019	$\frac{1-b_W}{1-b_Z}$ 0.908±0.005
Acceptance	$A_W$ 0.1451 <sup>+0.0020</sup> <sub>-0.0024</sub>	$A_Z$ 0.1153 <sup>+0.0021</sup> <sub>-0.0026</sub>	$\frac{A_Z}{A_W}$ 0.7949 <sup>+0.0068</sup> <sub>-0.0076</sub>
Efficiency	$\epsilon_W$ 0.661±0.009	$\epsilon_Z$ 0.633±0.011	$\frac{\epsilon_Z}{\epsilon_W}$ 0.957±0.007

**Table 11.1.** Measured input parameters for the cross section and ratio calculations.

analysis presented here are shown in table 11.1. For many parameters systematic uncertainties are quoted next to the central values.

## 11.1 W Cross Section

Using the values from Table 11.1 for  $p\bar{p} \rightarrow W \rightarrow \mu\nu$  process in Equation 11.1 we obtain the following result:

$$\sigma(p\bar{p} \rightarrow W)BR(W \rightarrow \mu\nu) = 2.786^{+0.060}_{-0.054}(\text{syst}) \pm 0.012(\text{stat}) \pm 0.166(\text{lum}) \text{ nb} , \quad (11.3)$$

which agrees well with the previous result based on 72 pb<sup>-1</sup> of CDF Run II data [20]

$$\sigma(p\bar{p} \rightarrow W)BR(W \rightarrow \mu\nu) = 2.791^{+0.077}_{-0.072}(\text{syst}) \pm 0.019(\text{stat}) \pm 0.167(\text{lum}) \text{ nb} . \quad (11.4)$$

To make a comparison with the theoretical prediction we use the calculated  $W$  production cross section for  $p\bar{p}$  collisions at  $\sqrt{s}=1.96$  TeV [37]. The theoretical prediction of the cross section and the branching ratio product is:

$$\sigma(p\bar{p} \rightarrow W) \cdot BR(W \rightarrow \mu\nu) = 2.687 \pm 0.054 \text{ nb}, \quad (11.5)$$

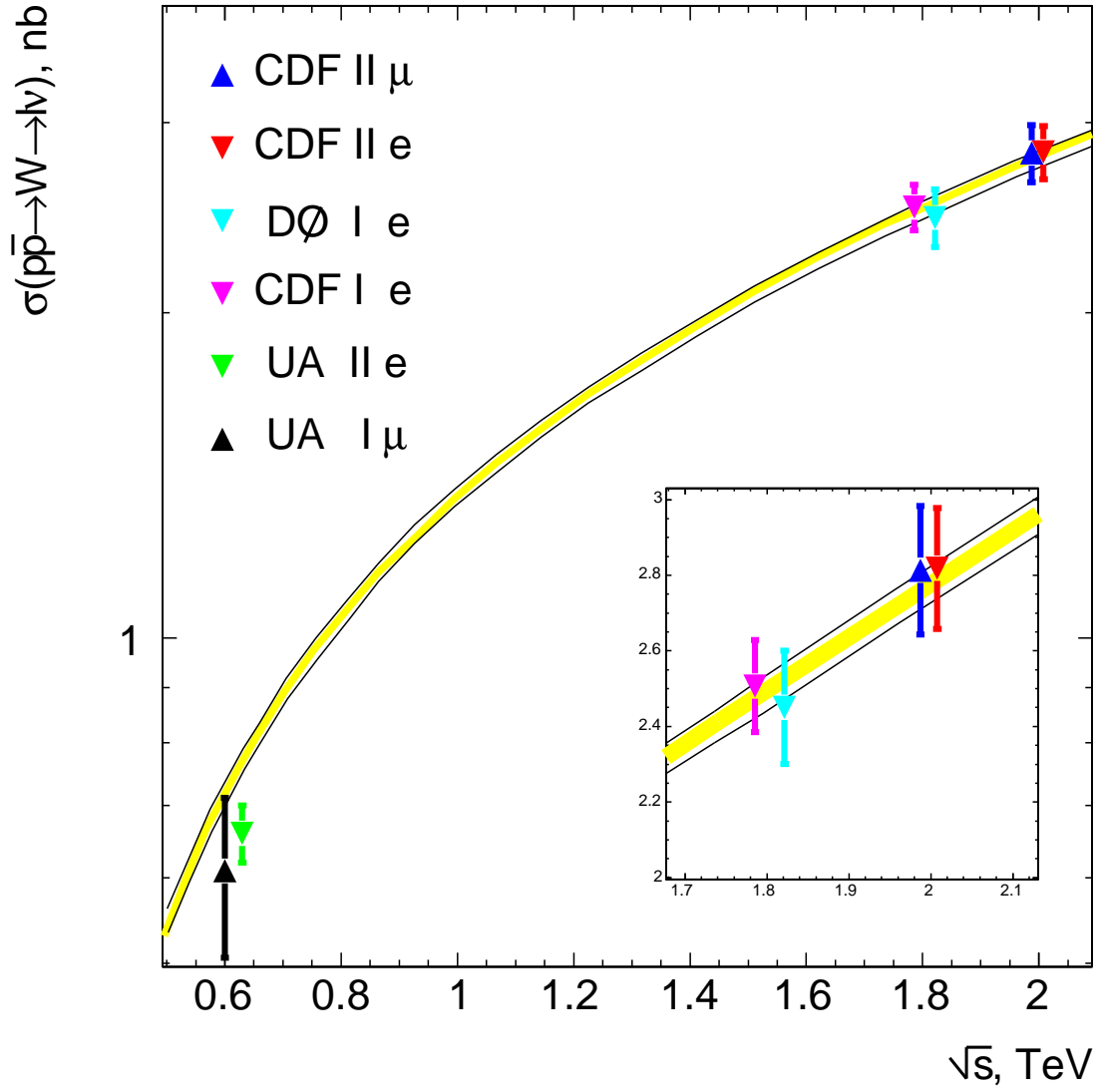
where the uncertainties come from the next-to-next-to leading order splitting functions, parton distribution functions and from the electroweak parameters [38].

Figure 11.1 shows the results of  $W$  production cross section measurement in the leptonic channel from various experiments in comparison with the theoretical prediction.

## 11.2 Z Cross Section

In case of  $p\bar{p} \rightarrow Z \rightarrow \mu^+\mu^-$  process we account for  $\gamma^* \rightarrow \mu^+\mu^-$  admixture to the  $Z \rightarrow \mu^+\mu^-$  decay by multiplying the number of  $Z$  signal events by a correction factor:

$$F_{Z\gamma^*} = \int_0^\infty \sigma_Z dM_{\mu\mu} \bigg/ \int_{66}^{116} (\sigma_Z + \sigma_{Z\gamma^*} + \sigma_{\gamma^*}) dM_{\mu\mu} = 1.004 \pm 0.001 . \quad (11.6)$$



**Figure 11.1.** The measurements of  $W$  production cross section in leptonic channel.

By using this factor we convert the measured  $Z/\gamma^* \rightarrow \mu^+\mu^-$  cross section over the 66–116 GeV/ $c^2$  dimuon invariant mass range to an exclusive  $Z \rightarrow \mu^+\mu^-$  cross section over the entire dimuon invariant mass range as discussed in Appendix A.

Using the values from table for  $p\bar{p} \rightarrow Z \rightarrow \mu^+\mu^-$  process in Equation 11.1 we obtain the following result

$$\sigma(p\bar{p} \rightarrow Z)BR(Z \rightarrow \mu^+\mu^-) = 253.1_{-6.2}^{+7.1}(\text{syst}) \pm 4.2(\text{stat}) \pm 15.2(\text{lum}) \text{ pb} , \quad (11.7)$$

which agrees well with the previous result based on 72 pb<sup>-1</sup> of CDF Run II data [20]

$$\sigma(p\bar{p} \rightarrow Z)BR(Z \rightarrow \mu^+\mu^-) = 253.1_{-8.1}^{+8.9}(\text{syst}) \pm 6.8(\text{stat}) \pm 15.1(\text{lum}) \text{ pb} . \quad (11.8)$$

To make a comparison with the theoretical prediction we use the calculated  $Z$  production cross section for  $p\bar{p}$  collisions at  $\sqrt{s} = 1.96$  TeV [37]. The theoretical prediction of the cross section and the branching ratio product is:

$$\sigma(p\bar{p} \rightarrow Z) \cdot BR(Z \rightarrow \mu^+\mu^-) = 251.3 \pm 5.0 \text{ pb}, \quad (11.9)$$

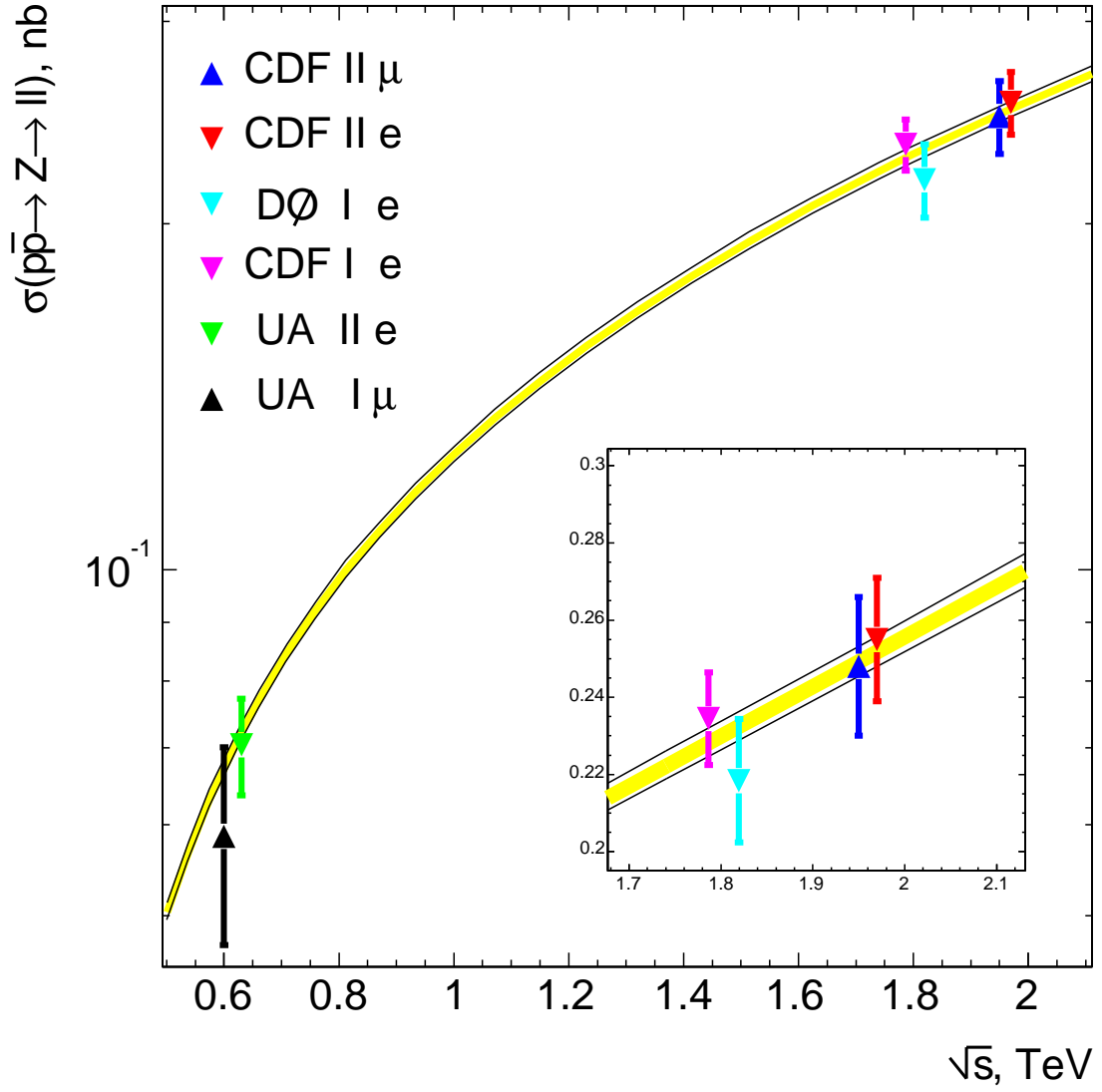
where the uncertainties come from the next-to-next-to leading order splitting functions, parton distribution functions and from the electroweak parameters [38].

Figure 11.2 shows the results of  $Z$  production cross section measurement in leptonic channel from various experiments in comparison with the theoretical prediction 11.2.

### 11.3 $W/Z$ Cross Section Ratio

To calculate the cross section ratio we use the Equation 11.2 with the parameter values from Table 11.1. We multiply the number of  $Z$  candidates by the correction factor  $F_{Z\gamma^*}$  as described in the previous subsection and obtain the following result:

$$R = 11.02 \pm 0.14(\text{syst}) \pm 0.18(\text{stat}) , \quad (11.10)$$



**Figure 11.2.** The measurements of  $Z$  production cross section in leptonic channel.

which agrees well with the previous result based on  $72 \text{ pb}^{-1}$  of CDF Run II data [20]

$$R = 11.03 \pm 0.18(\text{syst}) \pm 0.31(\text{stat}) . \quad (11.11)$$

The cross section ratio result 11.10 has significant improvement in precision over the cross section measurements of  $W$  11.3 and  $Z$  11.7 for which luminosity is a considerable source of uncertainty. In addition, the acceptance and efficiency calculation errors contribute less when used in the ratio due to the full or partial cancellations of uncertainty sources as can be seen in Table 11.1.

To make a comparison with the Standard Model prediction we use the calculated ratio of  $W$  and  $Z$  production cross section for  $p\bar{p}$  collisions at  $\sqrt{s}=1.96 \text{ TeV}$  [37]. The theoretical prediction of the ratio 11.2 is:

$$R = 10.69 \pm 0.013 , \quad (11.12)$$

where the uncertainties come from the next-to-next-to leading order splitting functions, parton distribution functions and from the electroweak parameters [38].

## 11.4 Extracting Physics Quantities

Equation for the cross section ratio 1.40 can be rewritten to express the  $W$  leptonic branching ratio:

$$BR(W \rightarrow \mu\nu) = \frac{\sigma(p\bar{p} \rightarrow Z)}{\sigma(p\bar{p} \rightarrow W)} \cdot BR(Z \rightarrow \mu\mu) \cdot R , \quad (11.13)$$

where the measured value of  $R$  is our result 11.10.

The Standard Model prediction for the  $W$  and  $Z$  production cross section ratio is:

$$\frac{\sigma(p\bar{p} \rightarrow W)}{\sigma(p\bar{p} \rightarrow Z)} = 3.3677 \pm 0.0155 , \quad (11.14)$$

according to the theoretical calculations [37] and [38].

For  $Z$  leptonic branching ratio we take the world average value [14]

$$BR(Z \rightarrow \ell^+ \ell^-) = 3.3658 \pm 0.0023 \% . \quad (11.15)$$

To obtain the value for our indirect measurement of  $W$  leptonic branching ratio we put parameters 11.10, 11.14 and 11.15 in the Equation 11.13:

$$BR(W \rightarrow \mu\nu) = 11.01 \pm 0.14(\text{syst}) \pm 0.18(\text{stat}) \pm 0.05(\text{ext}) \%, \quad (11.16)$$

where the external error comes from the input uncertainties of Equations 11.14–11.15. Figure 11.3 shows the comparison of our result for  $W$  leptonic branching ratio with those from the other measurements and the Standard Model prediction. The Standard Model value [33] is  $10.82 \pm 0.02 \%$ . The world average value is  $10.68 \pm 0.12 \%$ , which is based on 2002 edition of the Review of Particle Physics [14] and includes Run I results.

We can extract the value for the full width of  $W$  if we take the Standard Model value [14] for  $W$  lepton partial width

$$\Gamma(W \rightarrow \ell\nu) = 226.4 \pm 0.3 \text{ MeV}, \quad (11.17)$$

and divide it by our value for  $W$  leptonic branching ratio 11.16. The extracted value of  $W$  width is

$$\Gamma(W) = 2056 \pm 26(\text{syst}) \pm 34(\text{stat}) \pm 10(\text{ext}) \text{ MeV}, \quad (11.18)$$

where the external error comes from the input uncertainties of Equations 11.14–11.15 and 11.17. Figure 11.4 shows the comparison of our result for the full width of  $W$  with those from the other measurements and the Standard Model prediction. The Standard Model value [33] for  $W$  width can be evaluated using the Equation 1.27. However the precise calculation in the next-to-next-to-leading order [33] yields:

$$\Gamma_{\text{SM}}(W) = 2092.1 \pm 2.5 \text{ MeV}. \quad (11.19)$$

The world average value is  $2118 \pm 42 \text{ MeV}$ , which is based on 2002 edition of the Review of Particle Physics [14] and includes Run I results.

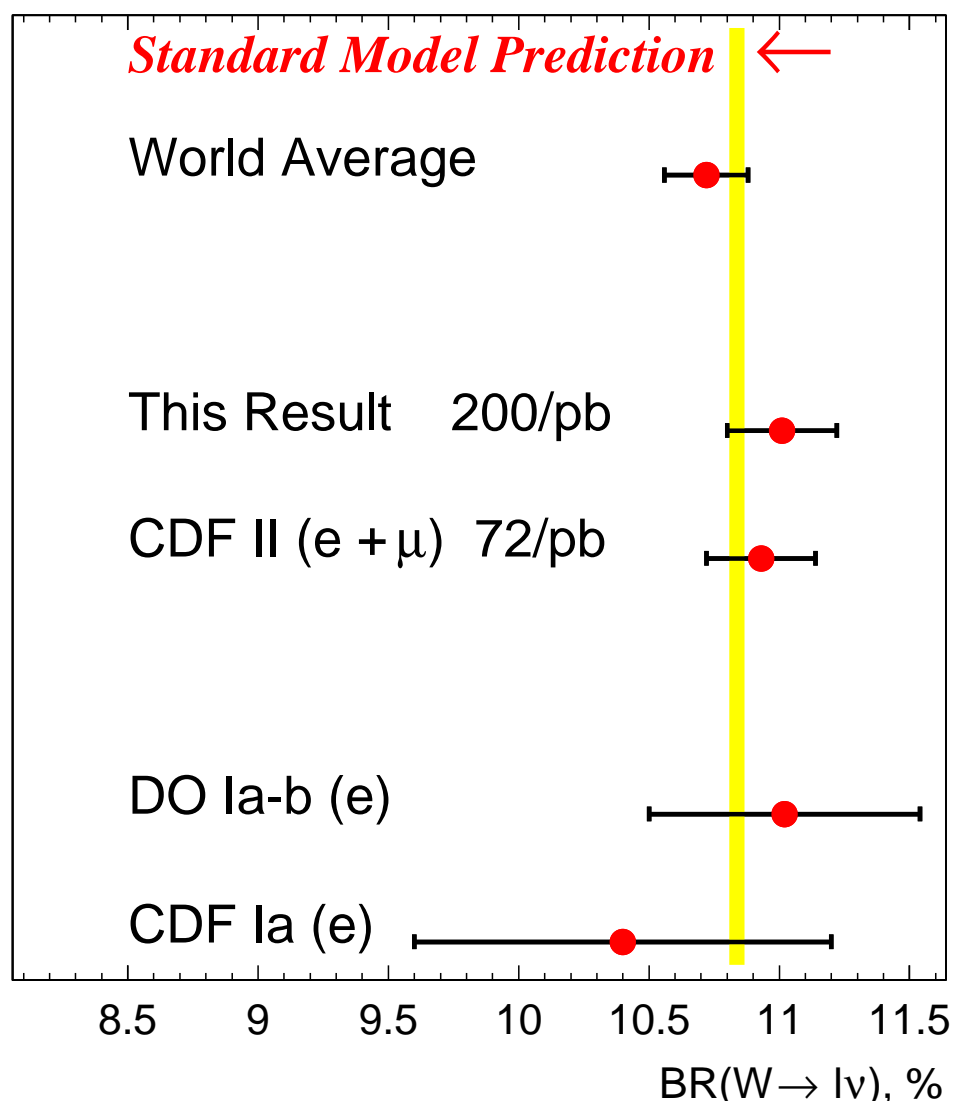


**Figure 11.3.** Comparison of our result for  $BR(W \rightarrow \ell \nu)$  with those from the other measurements and the Standard Model expectation.



## 11.5 Limit on Unknown Modes of $W$ Decay

Using our new measurement of the  $W$  width we can establish an upper limit for the width of the  $W$  decays into unknown final states. We assume the standard distribution of our result with the measurement error corresponding to the Gaussian standard deviation  $\Delta = 44$  MeV. The asymmetric 95 % confidence level interval has an upper boundary at  $1.644\Delta$  relative to the mean value. The maximum value of  $W$  width for the upper limit of this interval is

$$\Gamma_{max}(W) = \Gamma(W) + 1.644\Delta = 2128 \text{ MeV}. \quad (11.20)$$

On the other hand,  $\Gamma_{max}(W)$  can be expressed as:

$$\Gamma_{max}(W) = \Gamma_{SM}(W) + \Gamma(W \rightarrow \text{unknown}) , \quad (11.21)$$

where  $\Gamma_{SM}(W)$  is the Standard Model expectation for  $W$  width given by Equation 11.19, and  $\Gamma(W \rightarrow \text{unknown})$  is the width of the  $W$  decay into unknown final states. Therefore, our expectation for the maximum of  $\Gamma(W \rightarrow \text{unknown})$  at 95 % confidence level corresponds to

$$\Gamma(W \rightarrow \text{unknown}) < 36 \text{ MeV}. \quad (11.22)$$

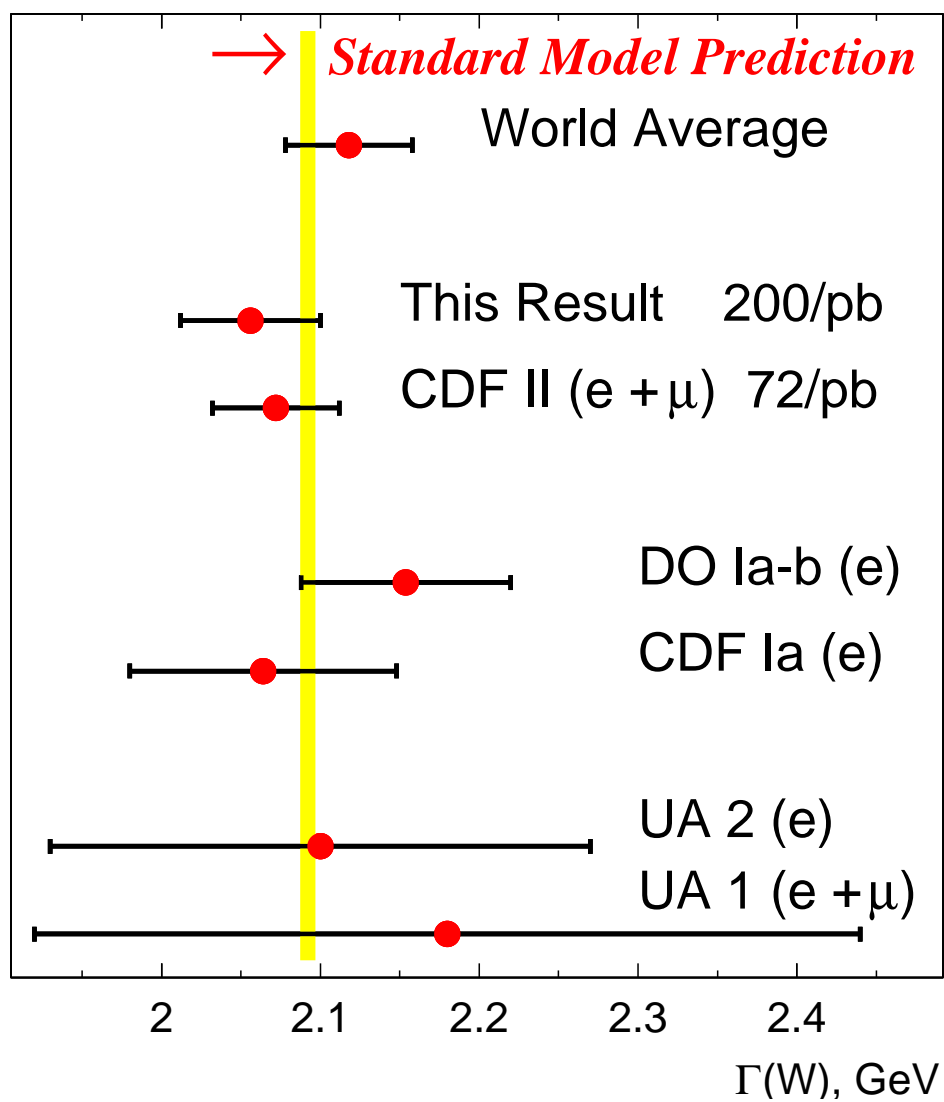


**Figure 11.4.** Comparison of our result for  $\Gamma(W)$  with those from the other measurements and the Standard Model prediction.

## APPENDICES

## APPENDIX A

### Interference Correction in $Z$ Cross Section

We wish to measure the  $Z$  production cross section as illustrated in Figure 1.2, where the  $Z$  boson is the only mediator. However, the intermediate state can also be a photon  $\gamma^*$  produced by annihilating quark antiquark pair. The total cross section for the observed dimuon final state is then given by the combination of the  $Z$  and  $\gamma^*$  intermediate states, plus the interference term between the two:

$$\sigma(q\bar{q} \rightarrow \mu^+\mu^-) = \sigma_Z + \sigma_{Z\gamma^*} + \sigma_{\gamma^*} .$$

The individual cross sections are given by the following expressions:

$$\begin{aligned} \sigma_Z &= 12\pi \frac{\hat{s}}{M_Z^2} \frac{\Gamma(Z \rightarrow \bar{q}q)\Gamma(Z \rightarrow \mu^+\mu^-)}{(\hat{s} - M_Z^2)^2 + M_Z^2\Gamma^2(Z)} \\ \sigma_{Z\gamma^*} &\sim \frac{\alpha(\hat{s})}{M_Z} \frac{(\hat{s} - M_Z^2)\sqrt{\Gamma(Z \rightarrow \bar{q}q)\Gamma(Z \rightarrow \mu^+\mu^-)}}{(\hat{s} - M_Z^2)^2 + M_Z^2\Gamma^2(Z)} \\ \sigma_{\gamma^*} &= \{4, 1\} \frac{4\pi\alpha^2(\hat{s})}{\hat{s}} \end{aligned}$$

where in the last expression factors 4 and 1 correspond to up- and down- flavored quarks respectively.

To correct our measurement for intermediate photon presence in our signal region, we define the correction factor as in Equation 11.6:

$$F_{Z\gamma^*} = \int_0^\infty \sigma_Z d\sqrt{\hat{s}} \bigg/ \int_{66}^{116} (\sigma_Z + \sigma_{Z\gamma^*} + \sigma_{\gamma^*}) d\sqrt{\hat{s}} = 1.004 \pm 0.001 .$$

## APPENDIX B

### The CDF Collaboration

D. Acosta,<sup>14</sup> T. Affolder,<sup>7</sup> M.G. Albrow,<sup>13</sup> D. Ambrose,<sup>36</sup> D. Amidei,<sup>27</sup> K. Anikeev,<sup>26</sup> J. Antos,<sup>1</sup> G. Apollinari,<sup>13</sup> T. Arisawa,<sup>50</sup> A. Artikov,<sup>11</sup> W. Ashmanskas,<sup>2</sup> F. Azfar,<sup>34</sup> P. Azzi-Bacchetta,<sup>35</sup> N. Bacchetta,<sup>35</sup> H. Bachacou,<sup>24</sup> W. Badgett,<sup>13</sup> A. Barbaro-Galtieri,<sup>24</sup> V.E. Barnes,<sup>39</sup> B.A. Barnett,<sup>21</sup> S. Baroiant,<sup>5</sup> M. Barone,<sup>15</sup> G. Bauer,<sup>26</sup> F. Bedeschi,<sup>37</sup> S. Behari,<sup>21</sup> S. Belforte,<sup>47</sup> W.H. Bell,<sup>17</sup> G. Bellettini,<sup>37</sup> J. Bellinger,<sup>51</sup> D. Benjamin,<sup>12</sup> A. Beretvas,<sup>13</sup> A. Bhatti,<sup>41</sup> M. Binkley,<sup>13</sup> D. Bisello,<sup>35</sup> M. Bishai,<sup>13</sup> R.E. Blair,<sup>2</sup> C. Blocker,<sup>4</sup> K. Bloom,<sup>27</sup> B. Blumenfeld,<sup>21</sup> A. Bocci,<sup>41</sup> A. Bodek,<sup>40</sup> G. Bolla,<sup>39</sup> A. Bolshov,<sup>26</sup> D. Bortoletto,<sup>39</sup> J. Boudreau,<sup>38</sup> C. Bromberg,<sup>28</sup> E. Brubaker,<sup>24</sup> J. Budagov,<sup>11</sup> H.S. Budd,<sup>40</sup> K. Burkett,<sup>13</sup> G. Busetto,<sup>35</sup> K.L. Byrum,<sup>2</sup> S. Cabrera,<sup>12</sup> M. Campbell,<sup>27</sup> W. Carithers,<sup>24</sup> D. Carlsmith,<sup>51</sup> A. Castro,<sup>3</sup> D. Cauz,<sup>47</sup> A. Cerri,<sup>24</sup> L. Cerrito,<sup>20</sup> J. Chapman,<sup>27</sup> C. Chen,<sup>36</sup> Y.C. Chen,<sup>1</sup> M. Chertok,<sup>5</sup> G. Chiarelli,<sup>37</sup> G. Chlachidze,<sup>13</sup> F. Chlebana,<sup>13</sup> M.L. Chu,<sup>1</sup> J.Y. Chung,<sup>32</sup> W.-H. Chung,<sup>51</sup> Y.S. Chung,<sup>40</sup> C.I. Ciobanu,<sup>20</sup> A.G. Clark,<sup>16</sup> M. Coca,<sup>40</sup> A. Connolly,<sup>24</sup> M. Convery,<sup>41</sup> J. Conway,<sup>43</sup> M. Cordelli,<sup>15</sup> J. Cranshaw,<sup>45</sup> R. Culbertson,<sup>13</sup> D. Dagenhart,<sup>4</sup> S. D'Auria,<sup>17</sup> P. de Barbaro,<sup>40</sup> S. De Cecco,<sup>42</sup> S. Dell'Agnello,<sup>15</sup> M. Dell'Orso,<sup>37</sup> S. Demers,<sup>40</sup> L. Demortier,<sup>41</sup> M. Deninno,<sup>3</sup> D. De Pedis,<sup>42</sup> P.F. Derwent,<sup>13</sup> C. Dionisi,<sup>42</sup> J.R. Dittmann,<sup>13</sup> A. Dominguez,<sup>24</sup> S. Donati,<sup>37</sup> M. D'Onofrio,<sup>16</sup> T. Dorigo,<sup>35</sup> N. Eddy,<sup>20</sup> R. Erbacher,<sup>13</sup> D. Errede,<sup>20</sup> S. Errede,<sup>20</sup> R. Eusebi,<sup>40</sup> S. Farrington,<sup>17</sup> R.G. Feild,<sup>52</sup> J.P. Fernandez,<sup>39</sup> C. Ferretti,<sup>27</sup> R.D. Field,<sup>14</sup> I. Fiori,<sup>37</sup> B. Flaughner,<sup>13</sup> L.R. Flores-Castillo,<sup>38</sup> G.W. Foster,<sup>13</sup> M. Franklin,<sup>18</sup> J. Friedman,<sup>26</sup> I. Furic,<sup>26</sup>

M. Gallinaro,<sup>41</sup> M. Garcia-Sciveres,<sup>24</sup> A.F. Garfinkel,<sup>39</sup> C. Gay,<sup>52</sup> D.W. Gerdes,<sup>27</sup>  
 E. Gerstein,<sup>9</sup> S. Giagu,<sup>42</sup> P. Giannetti,<sup>37</sup> K. Giolo,<sup>39</sup> M. Giordani,<sup>47</sup> P. Giromini,<sup>15</sup>  
 V. Glagolev,<sup>11</sup> D. Glenzinski,<sup>13</sup> M. Gold,<sup>30</sup> N. Goldschmidt,<sup>27</sup> J. Goldstein,<sup>34</sup>  
 G. Gomez,<sup>8</sup> M. Goncharov,<sup>44</sup> I. Gorelov,<sup>30</sup> A.T. Goshaw,<sup>12</sup> Y. Gotra,<sup>38</sup> K. Goulianos,<sup>41</sup>  
 A. Gresele,<sup>3</sup> C. Grosso-Pilcher,<sup>10</sup> M. Guenther,<sup>39</sup> J. Guimaraes da Costa,<sup>18</sup> C. Haber,<sup>24</sup>  
 S.R. Hahn,<sup>13</sup> E. Halkiadakis,<sup>40</sup> R. Handler,<sup>51</sup> F. Happacher,<sup>15</sup> K. Hara,<sup>48</sup> R.M. Harris,<sup>13</sup>  
 F. Hartmann,<sup>22</sup> K. Hatakeyama,<sup>41</sup> J. Hauser,<sup>6</sup> S.J. Haywood,<sup>53</sup> J. Heinrich,<sup>36</sup>  
 M. Hennecke,<sup>22</sup> M. Herndon,<sup>21</sup> C. Hill,<sup>7</sup> A. Hocker,<sup>40</sup> K.D. Hoffman,<sup>10</sup> S. Hou,<sup>1</sup>  
 B.T. Huffman,<sup>34</sup> R. Hughes,<sup>32</sup> J. Huston,<sup>28</sup> C. Issever,<sup>7</sup> J. Incandela,<sup>7</sup> G. Introzzi,<sup>37</sup>  
 M. Iori,<sup>42</sup> A. Ivanov,<sup>40</sup> Y. Iwata,<sup>19</sup> B. Iyutin,<sup>26</sup> E. James,<sup>13</sup> M. Jones,<sup>39</sup> T. Kamon,<sup>44</sup>  
 J. Kang,<sup>27</sup> M. Karagoz Unel,<sup>31</sup> S. Kartal,<sup>13</sup> H. Kasha,<sup>52</sup> Y. Kato,<sup>33</sup> R.D. Kennedy,<sup>13</sup>  
 R. Kephart,<sup>13</sup> B. Kilminster,<sup>40</sup> D.H. Kim,<sup>23</sup> H.S. Kim,<sup>20</sup> M.J. Kim,<sup>9</sup> S.B. Kim,<sup>23</sup>  
 S.H. Kim,<sup>48</sup> T.H. Kim,<sup>26</sup> Y.K. Kim,<sup>10</sup> M. Kirby,<sup>12</sup> L. Kirsch,<sup>4</sup> S. Klimenko,<sup>14</sup>  
 P. Koehn,<sup>32</sup> K. Kondo,<sup>50</sup> J. Konigsberg,<sup>14</sup> A. Korn,<sup>26</sup> A. Korytov,<sup>14</sup> J. Kroll,<sup>36</sup>  
 M. Kruse,<sup>12</sup> V. Krutelyov,<sup>44</sup> S.E. Kuhlmann,<sup>2</sup> N. Kuznetsova,<sup>13</sup> A.T. Laasanen,<sup>39</sup>  
 S. Lami,<sup>41</sup> S. Lammel,<sup>13</sup> J. Lancaster,<sup>12</sup> K. Lannon,<sup>32</sup> M. Lancaster,<sup>25</sup> R. Lander,<sup>5</sup>  
 A. Lath,<sup>43</sup> G. Latino,<sup>30</sup> T. LeCompte,<sup>2</sup> Y. Le,<sup>21</sup> J. Lee,<sup>40</sup> S.W. Lee,<sup>44</sup> N. Leonardo,<sup>26</sup>  
 S. Leone,<sup>37</sup> J.D. Lewis,<sup>13</sup> K. Li,<sup>52</sup> C.S. Lin,<sup>13</sup> M. Lindgren,<sup>6</sup> T.M. Liss,<sup>20</sup> T. Liu,<sup>13</sup>  
 D.O. Litvintsev,<sup>13</sup> N.S. Lockyer,<sup>36</sup> A. Loginov,<sup>29</sup> M. Loreti,<sup>35</sup> D. Lucchesi,<sup>35</sup> P. Lukens,<sup>13</sup>  
 L. Lyons,<sup>34</sup> J. Lys,<sup>24</sup> R. Madrak,<sup>18</sup> K. Maeshima,<sup>13</sup> P. Maksimovic,<sup>21</sup> L. Malferrari,<sup>3</sup>  
 M. Mangano,<sup>37</sup> G. Manca,<sup>34</sup> M. Mariotti,<sup>35</sup> M. Martin,<sup>21</sup> A. Martin,<sup>52</sup> V. Martin,<sup>31</sup>  
 M. Martínez,<sup>13</sup> P. Mazzanti,<sup>3</sup> K.S. McFarland,<sup>40</sup> P. McIntyre,<sup>44</sup> M. Menguzzato,<sup>35</sup>  
 A. Menzione,<sup>37</sup> P. Merkel,<sup>13</sup> C. Mesropian,<sup>41</sup> A. Meyer,<sup>13</sup> T. Miao,<sup>13</sup> R. Miller,<sup>28</sup>  
 J.S. Miller,<sup>27</sup> S. Miscetti,<sup>15</sup> G. Mitselmakher,<sup>14</sup> N. Moggi,<sup>3</sup> R. Moore,<sup>13</sup> T. Moulik,<sup>39</sup>  
 M. Mulhearn,<sup>26</sup> A. Mukherjee,<sup>13</sup> T. Muller,<sup>22</sup> A. Munar,<sup>36</sup> P. Murat,<sup>13</sup> J. Nachtman,<sup>13</sup>  
 S. Nahn,<sup>52</sup> I. Nakano,<sup>19</sup> R. Napora,<sup>21</sup> F. Niell,<sup>27</sup> C. Nelson,<sup>13</sup> T. Nelson,<sup>13</sup> C. Neu,<sup>32</sup>  
 M.S. Neubauer,<sup>26</sup> C. Newman-Holmes,<sup>13</sup> T. Nigmanov,<sup>38</sup> L. Nodulman,<sup>2</sup> S.H. Oh,<sup>12</sup>

Y.D. Oh,<sup>23</sup> T. Ohsugi,<sup>19</sup> T. Okusawa,<sup>33</sup> W. Orejudos,<sup>24</sup> C. Pagliarone,<sup>37</sup> F. Palmonari,<sup>37</sup>  
 R. Paoletti,<sup>37</sup> V. Papadimitriou,<sup>45</sup> J. Patrick,<sup>13</sup> G. Pauletta,<sup>47</sup> M. Paulini,<sup>9</sup> T. Pauly,<sup>34</sup>  
 C. Paus,<sup>26</sup> D. Pellett,<sup>5</sup> A. Penzo,<sup>47</sup> T.J. Phillips,<sup>12</sup> G. Piacentino,<sup>37</sup> J. Piedra,<sup>8</sup>  
 K.T. Pitts,<sup>20</sup> A. Pompoš,<sup>39</sup> L. Pondrom,<sup>51</sup> G. Pope,<sup>38</sup> T. Pratt,<sup>34</sup> F. Prokoshin,<sup>11</sup>  
 J. Proudfoot,<sup>2</sup> F. Ptohos,<sup>15</sup> O. Poukhov,<sup>11</sup> G. Punzi,<sup>37</sup> J. Rademacker,<sup>34</sup> A. Rakitine,<sup>26</sup>  
 F. Ratnikov,<sup>43</sup> H. Ray,<sup>27</sup> A. Reichold,<sup>34</sup> P. Renton,<sup>34</sup> M. Rescigno,<sup>42</sup> F. Rimondi,<sup>3</sup>  
 L. Ristori,<sup>37</sup> W.J. Robertson,<sup>12</sup> T. Rodrigo,<sup>8</sup> S. Rolli,<sup>49</sup> L. Rosenson,<sup>26</sup> R. Roser,<sup>13</sup>  
 R. Rossin,<sup>35</sup> C. Rott,<sup>39</sup> A. Roy,<sup>39</sup> A. Ruiz,<sup>8</sup> D. Ryan,<sup>49</sup> A. Safonov,<sup>5</sup> R. St. Denis,<sup>17</sup>  
 W.K. Sakumoto,<sup>40</sup> D. Saltzberg,<sup>6</sup> C. Sanchez,<sup>32</sup> A. Sansoni,<sup>15</sup> L. Santi,<sup>47</sup> S. Sarkar,<sup>42</sup>  
 P. Savard,<sup>46</sup> A. Savoy-Navarro,<sup>13</sup> P. Schlabach,<sup>13</sup> E.E. Schmidt,<sup>13</sup> M.P. Schmidt,<sup>52</sup>  
 M. Schmitt,<sup>31</sup> L. Scodellaro,<sup>35</sup> A. Scribano,<sup>37</sup> A. Sedov,<sup>39</sup> S. Seidel,<sup>30</sup> Y. Seiya,<sup>48</sup>  
 A. Semenov,<sup>11</sup> F. Semeria,<sup>3</sup> M.D. Shapiro,<sup>24</sup> P.F. Shepard,<sup>38</sup> T. Shibayama,<sup>48</sup>  
 M. Shimojima,<sup>48</sup> M. Shochet,<sup>10</sup> A. Sidoti,<sup>35</sup> A. Sill,<sup>45</sup> P. Sinervo,<sup>46</sup> A.J. Slaughter,<sup>52</sup>  
 K. Sliwa,<sup>49</sup> F.D. Snider,<sup>13</sup> R. Snihur,<sup>25</sup> M. Spezziga,<sup>45</sup> F. Spinella,<sup>37</sup> M. Spiropulu,<sup>7</sup>  
 L. Spiegel,<sup>13</sup> A. Stefanini,<sup>37</sup> J. Strologas,<sup>30</sup> D. Stuart,<sup>7</sup> A. Sukhanov,<sup>14</sup> K. Sumorok,<sup>26</sup>  
 T. Suzuki,<sup>48</sup> R. Takashima,<sup>19</sup> K. Takikawa,<sup>48</sup> M. Tanaka,<sup>2</sup> M. Tecchio,<sup>27</sup> R.J. Tesarek,<sup>13</sup>  
 P.K. Teng,<sup>1</sup> K. Terashi,<sup>41</sup> S. Tether,<sup>26</sup> J. Thom,<sup>13</sup> A.S. Thompson,<sup>17</sup> E. Thomson,<sup>32</sup>  
 P. Tipton,<sup>40</sup> S. Tkaczyk,<sup>13</sup> D. Toback,<sup>44</sup> K. Tollefson,<sup>28</sup> D. Tonelli,<sup>37</sup> M. Tönnemann,<sup>28</sup>  
 H. Toyoda,<sup>33</sup> W. Trischuk,<sup>46</sup> J. Tseng,<sup>26</sup> D. Tsybychev,<sup>14</sup> N. Turini,<sup>37</sup> F. Ukegawa,<sup>48</sup>  
 T. Unverhau,<sup>17</sup> T. Vaiciulis,<sup>40</sup> A. Varganov,<sup>27</sup> E. Vataha,<sup>37</sup> S. Vejcek III,<sup>13</sup> G. Velez,<sup>13</sup>  
 G. Veramendi,<sup>24</sup> R. Vidal,<sup>13</sup> I. Vila,<sup>8</sup> R. Vilar,<sup>8</sup> I. Volobouev,<sup>24</sup> M. von der Mey,<sup>6</sup>  
 R.G. Wagner,<sup>2</sup> R.L. Wagner,<sup>13</sup> W. Wagner,<sup>22</sup> Z. Wan,<sup>43</sup> C. Wang,<sup>12</sup> M.J. Wang,<sup>1</sup>  
 S.M. Wang,<sup>14</sup> B. Ward,<sup>17</sup> S. Waschke,<sup>17</sup> D. Waters,<sup>25</sup> T. Watts,<sup>43</sup> M. Weber,<sup>24</sup>  
 W.C. Wester III,<sup>13</sup> B. Whitehouse,<sup>49</sup> A.B. Wicklund,<sup>2</sup> E. Wicklund,<sup>13</sup> H.H. Williams,<sup>36</sup>  
 P. Wilson,<sup>13</sup> B.L. Winer,<sup>32</sup> S. Wolbers,<sup>13</sup> M. Wolter,<sup>49</sup> S. Worm,<sup>43</sup> X. Wu,<sup>16</sup>  
 F. Würthwein,<sup>26</sup> U.K. Yang,<sup>10</sup> W. Yao,<sup>24</sup> G.P. Yeh,<sup>13</sup> K. Yi,<sup>21</sup> J. Yoh,<sup>13</sup> T. Yoshida,<sup>33</sup>  
 I. Yu,<sup>23</sup> S. Yu,<sup>36</sup> J.C. Yun,<sup>13</sup> L. Zanello,<sup>42</sup> A. Zanetti,<sup>47</sup> F. Zetti,<sup>24</sup> and S. Zucchelli<sup>3</sup>

- <sup>1</sup> *Institute of Physics, Academia Sinica, Taipei, Taiwan 11529, Republic of China*
- <sup>2</sup> *Argonne National Laboratory, Argonne, Illinois 60439*
- <sup>3</sup> *Istituto Nazionale di Fisica Nucleare, University of Bologna, I-40127 Bologna, Italy*
- <sup>4</sup> *Brandeis University, Waltham, Massachusetts 02254*
- <sup>5</sup> *University of California at Davis, Davis, California 95616*
- <sup>6</sup> *University of California at Los Angeles, Los Angeles, California 90024*
- <sup>7</sup> *University of California at Santa Barbara, Santa Barbara, California 93106*
- <sup>8</sup> *Instituto de Fisica de Cantabria, CSIC-University of Cantabria, 39005 Santander, Spain*
- <sup>9</sup> *Carnegie Mellon University, Pittsburgh, Pennsylvania 15213*
- <sup>10</sup> *Enrico Fermi Institute, University of Chicago, Chicago, Illinois 60637*
- <sup>11</sup> *Joint Institute for Nuclear Research, RU-141980 Dubna, Russia*
- <sup>12</sup> *Duke University, Durham, North Carolina 27708*
- <sup>13</sup> *Fermi National Accelerator Laboratory, Batavia, Illinois 60510*
- <sup>14</sup> *University of Florida, Gainesville, Florida 32611*
- <sup>15</sup> *Laboratori Nazionali di Frascati, Istituto Nazionale di Fisica Nucleare, I-00044 Frascati, Italy*
- <sup>16</sup> *University of Geneva, CH-1211 Geneva 4, Switzerland*
- <sup>17</sup> *Glasgow University, Glasgow G12 8QQ, United Kingdom*
- <sup>18</sup> *Harvard University, Cambridge, Massachusetts 02138*
- <sup>19</sup> *Hiroshima University, Higashi-Hiroshima 724, Japan*
- <sup>20</sup> *University of Illinois, Urbana, Illinois 61801*
- <sup>21</sup> *The Johns Hopkins University, Baltimore, Maryland 21218*
- <sup>22</sup> *Institut für Experimentelle Kernphysik, Universität Karlsruhe, 76128 Karlsruhe, Germany*
- <sup>23</sup> *Center for High Energy Physics: Kyungpook National University, Taegu 702-701; Seoul National University, Seoul 151-742; and SungKyunKwan University, Suwon 440-746; Korea*
- <sup>24</sup> *Ernest Orlando Lawrence Berkeley National Laboratory, Berkeley, California 94720*
- <sup>25</sup> *University College London, London WC1E 6BT, United Kingdom*
- <sup>26</sup> *Massachusetts Institute of Technology, Cambridge, Massachusetts 02139*



- <sup>27</sup> *University of Michigan, Ann Arbor, Michigan 48109*
- <sup>28</sup> *Michigan State University, East Lansing, Michigan 48824*
- <sup>29</sup> *Institution for Theoretical and Experimental Physics, ITEP, Moscow 117259, Russia*
- <sup>30</sup> *University of New Mexico, Albuquerque, New Mexico 87131*
- <sup>31</sup> *Northwestern University, Evanston, Illinois 60208*
- <sup>32</sup> *The Ohio State University, Columbus, Ohio 43210*
- <sup>33</sup> *Osaka City University, Osaka 588, Japan*
- <sup>34</sup> *University of Oxford, Oxford OX1 3RH, United Kingdom*
- <sup>35</sup> *Universita di Padova, Istituto Nazionale di Fisica Nucleare, Sezione di Padova, I-35131 Padova, Italy*
- <sup>36</sup> *University of Pennsylvania, Philadelphia, Pennsylvania 19104*
- <sup>37</sup> *Istituto Nazionale di Fisica Nucleare, University and Scuola Normale Superiore of Pisa, I-56100 Pisa, Italy*
- <sup>38</sup> *University of Pittsburgh, Pittsburgh, Pennsylvania 15260*
- <sup>39</sup> *Purdue University, West Lafayette, Indiana 47907*
- <sup>40</sup> *University of Rochester, Rochester, New York 14627*
- <sup>41</sup> *Rockefeller University, New York, New York 10021*
- <sup>42</sup> *Istituto Nazionale de Fisica Nucleare, Sezione di Roma, University di Roma I, I-00185 Roma, Italy*
- <sup>43</sup> *Rutgers University, Piscataway, New Jersey 08855*
- <sup>44</sup> *Texas A&M University, College Station, Texas 77843*
- <sup>45</sup> *Texas Tech University, Lubbock, Texas 79409*
- <sup>46</sup> *Institute of Particle Physics, University of Toronto, Toronto M5S 1A7, Canada*
- <sup>47</sup> *Istituto Nazionale di Fisica Nucleare, University of Trieste/ Udine, Italy*
- <sup>48</sup> *University of Tsukuba, Tsukuba, Ibaraki 305, Japan*
- <sup>49</sup> *Tufts University, Medford, Massachusetts 02155*
- <sup>50</sup> *Waseda University, Tokyo 169, Japan*
- <sup>51</sup> *University of Wisconsin, Madison, Wisconsin 53706*
- <sup>52</sup> *Yale University, New Haven, Connecticut 06520*
- <sup>53</sup> *CCLRC Rutherford Appleton Laboratory, Didcot OX11 0QX, UK*

## BIBLIOGRAPHY

# BIBLIOGRAPHY

- [1] S. Glashow, *Partial Symmetries Of Weak Interactions*,  
*Nucl. Phys.* **22** (1961) 579
- [2] S. Weinberg, *A Model Of Leptons*, *Phys. Rev. Lett.* **19** (1967) 1264
- [3] A. Salam, *Elementary Particle Theory*,  
edited by N. Svartholm (Almquist and Wiksells, Stockholm, 1969), 367.
- [4] W. Bardeen, H. Fritzsch, M. Gell-Mann, *Scale and Conformal Symmetry in Hadron Physics*, edited by R. Gatto (Wiley, New York, 1973), 139.
- [5] D. Gross and F. Wilczek, *Asymptotically Free Gauge Theories. I*,  
*Phys. Rev. D* **8** (1973) 3633
- [6] S. Weinberg, *Nonabelian Gauge Theories Of The Strong Interactions*,  
*Phys. Rev. Lett.* **31** (1973) 494
- [7] The UA1 Collaboration (G. Arnison et al.), *Experimental observation of isolated large transverse energy electrons with associated missing energy at  $\sqrt{s}=540$  GeV*, *Phys. Lett. B* **122** (1983) 103
- [8] UA2 Collaboration (P. Bagnaia et al.), *Observation Of Single Isolated Electrons Of High Transverse Momentum In Events With Missing Transverse Energy At The Cern  $p\bar{p}$  Collider*, *Phys. Lett. B* **122** (1983) 476
- [9] The UA1 Collaboration (G. Arnison et al.), *Experimental Observation Of Lepton Pairs Of Invariant Mass Around  $95\text{GeV}/c^2$  At The CERN SPS Collider*, *Phys. Lett. B* **126** (1983) 398
- [10] UA2 Collaboration (P. Bagnaia et al.), *Evidence For  $Z^0 \rightarrow e^+e^-$  At The Cern  $p\bar{p}$  Collider*, *Phys. Lett. B* **129** (1983) 130

- [11] P.W. Higgs, *Broken Symmetries and the Masses of Gauge Bosons*,  
*Phys. Rev. Lett.* **13** (1964) 508
- [12] K. Kane, *Modern Elementary Particle Physics*,  
updated edition (Addison Wesley, 1993), 92
- [13] W. Badgett and P. Derwent, *Event z Vertex Cut Efficiency as a Luminosity Correction for Run Ia*, *CDF Note* **2527**, Jul. 12, 1994
- [14] K. Hagiwara et al. *Particle Data Group*, *Phys. Rev. D* **66** (2002) 010001
- [15] V. Barger and R. Phillips, *Collider Physics*, updated edition  
(Perseus Books, 1996)
- [16] J. Pumplin, D. Stump, J. Huston, H. L. Lai, P. Nadosky, W. K. Tung, *New Generation of Parton Distributions with Uncertainties from Global QCD Analysis*,  
[hep-ph/0201195](#)
- [17] Ken Bloom, Eric James, Jian Kang, Victoria Martin, Tracey Pratt, Michael Schmitt, Anyes Taffard, and Alexei Varganov, *Measurement of  $\sigma(p\bar{p} \rightarrow W \rightarrow \mu\nu)$  with Data from CDF II*, *CDF Note* **6017**, Jul. 16, 2002.
- [18] Ken Bloom, Eric James, Jian Kang, Victoria Martin, Tracey Pratt, Michael Schmitt, Anyes Taffard, and Alexei Varganov, *Measurement of  $\frac{\sigma(p\bar{p} \rightarrow W \rightarrow \mu\nu)}{\sigma(p\bar{p} \rightarrow Z \rightarrow \mu^+\mu^-)}$  with Data from CDF II*, *CDF Note* **6025**, Jul. 10, 2002.
- [19] Ken Bloom, Eric James, Jian Kang, Victoria Martin, Michael Schmitt, Anyes Taffard, and Alexei Varganov *Updated Measurements of  $\sigma(p\bar{p} \rightarrow W \rightarrow \mu\nu)$ ,  $\sigma(p\bar{p} \rightarrow Z \rightarrow \mu\mu)$ , and  $R$  Using CDF Run II Data*,  
*CDF Note* **6302**, Mar. 21, 2003.
- [20] Dan Amidei, Ken Bloom, Mircea Coca, Eva Halkiadakis, Eric James, Jian Kang, Young-Kee Kim, Giulia Manca, Victoria Martin, Pasha Murat, Aidan Robson, Willis Sakumoto, Michael Schmitt, Greg Veramendi, and Alexei Varganov *Measurements of  $p\bar{p} \rightarrow W \rightarrow \mu\nu$  and  $p\bar{p} \rightarrow Z \rightarrow \mu\mu$  Production Cross Sections and  $R$  Using CDF Run II Data*, *CDF Note* **6711**, Feb. 27, 2004.

- [21] Alexei Varganov and Dan Amidei, *Measurement of W and Z Production Cross Sections and Ratio in Muon Channel with 200 pb-1*, CDF Note **6884**, Feb. 16, 2004.
- [22] Fermilab Beam Division *Run II Handbook*  
[http://www-bd.fnal.gov/lug/runII\\_handbook/RunII\\_index.html](http://www-bd.fnal.gov/lug/runII_handbook/RunII_index.html)
- [23] D. Amidei, *The CDF II Detector*, Technical Design Report, 1996
- [24] Data Quality Monitoring Group *Version IV of the Good Run List*  
<http://www-cdf.fnal.gov/internal/dqm/goodrun/v4/goodv4.html>
- [25] Ricardo Eusebi *Secondary Data Sets for the Top Group*  
<http://b0urpc.fnal.gov/~eusebi/Stripping/TopDataSets.html>
- [26] Evelyn J. Thomson *Description of data samples for Top Group for Summer 2003*, CDF Note **6548**, Jul. 1, 2003.
- [27] Dmitry O. Litvintsev *The CDF Run II Data File Catalog*,  
CDF Note **5983**, May. 29, 2002.
- [28] B. Roe, *Probability and Statistics in Experimental Physics*, Second edition (Springer, 2001)
- [29] Torbjörn Sjöstrand, Leif Lönnblad, Stephen Mrenna, Peter Skands *PYTHIA 6.3 Physics and Manual*, [hep-ph/0308153](http://hep-ph/0308153)
- [30] Daniel Stump, Joey Huston, Jon Pumplin, Wu-Ki Tung, H. L. Lai, Steve Kuhlmann, J. F. Owens *Inclusive Jet Production, Parton Distributions, and the Search for New Physics*, [hep-ph/0303013](http://hep-ph/0303013)
- [31] Mircea Coca, Henry Frisch, David Goldstein, Jaco Konigsberg, Mark Kruse, Nancy Lai, Carla Pilcher, David Saltzberg, Paul Tipton, Un-ki Yang *Draft Proposal for the Summer-2002 Top Dilepton Analysis and Top Dilepton Dataset*, CDF Note **5676**, Jul. 13, 2001.
- [32] Heather K. Gerberich, Ashutosh V. Kotwal and Chris Hays *Cosmic Ray Tagging using COT Hit Timing*, CDF Note **6089**, Aug. 19, 2002.

- [33] Eva Halkiadakis, Eric James, Jian Kang, Guilia Manca, Victoria Martin, Pasha Murat, Peter Renton, Willis Sakumoto, Michael Schmitt, *Updated Combination of  $e$  and  $\mu$  Measurements of the  $W$  and  $Z$  Cross Sections and Their Ratio*, CDF Note **6894**, Mar. 6, 2004.
- [34] The CDF Collaboration (F. Abe et al.), *A Measurement of the ratio  $\sigma(p\bar{p} \rightarrow W)B(W \rightarrow e\nu)/\sigma(p\bar{p} \rightarrow Z^0)B(Z^0 \rightarrow e^+e^-)$  in  $p\bar{p}$  collisions at  $\sqrt{s} = 1800$  GeV*, *Phys. Rev. D* **52** (1995) 2624.
- [35] Eva Halkiadakis, Eric James, Jian Kang, Guilia Manca, Victoria Martin, Pasha Murat, Aidan Robson, Michael Schmitt *PDF Uncertainties for  $W$  and  $Z$  Cross Section Measurements*, CDF Note **6890**, Feb. 22, 2004.
- [36] D. Glenzinski, M. Herndon, C.-J. Lin, J. Thom, A. Yagil, *Determination of the Run IIa COT Tracking Efficiency Using the  $W$ -No-Track Sample*, CDF Note **6866**, Jun. 14, 2002.
- [37] Willis Sakumoto,  *$W/Z$  Cross Section Predictions for  $\sqrt{s} = 1.96$  TeV*, CDF Note **6341**, Feb. 23, 2003.
- [38] Willis Sakumoto,  *$W/Z$  Cross Section Predictions Errors for  $\sqrt{s} = 1.96$  TeV*, CDF Note **6899**, Feb. 25, 2004.